学位論文

Systematic Study on Microscopic Ferromagnetism and High T_C in Anatase Co-doped TiO_2 Epitaxial Thin Films

(アナターゼ型 Co ドープ TiO_2 エピタキシャル薄膜の微視的強磁性と高 T_C に関する系統的研究)

平成 27 年 12 月博士（理学）申請

東京大学大学院理学系研究科

化学専攻

クラシエンアピバーン　タンティップ　シリナピグ

KRASIENAPIBAL THANTIP SIRINABHIGUPTA

Systematic Study on Microscopic Ferromagnetism and High T_C in Anatase Co-doped TiO_2 Epitaxial Thin Films

by

Thantip S. Krasienapibal

Department of Chemistry
Graduate School of Science
The University of Tokyo

December 2015

Abstract

Ferromagnetic oxide semiconductor Co-doped TiO_2 ($Ti_{1-x}Co_xO_2$; (Ti,Co)O_2) is a promising candidate of semiconductor spintronic materials. This compound has high ferromagnetic Curie temperature, T_C (> 600 K). Its ferromagnetism at room temperature can be controlled via electrostatic and chemical carrier doping. Although there are many reports on (Ti,Co)O_2 especially for high quality film fabrication, bulk magnetization and controlling of magnetic property, there are still several issues on this compound related to microscopic ferromagnetism, magnetically dead layer in the surface and mechanism of the high T_C.

I conducted microscopic investigation of ferromagnetism in anatase (Ti,Co)O_2 thin film by means of the observation of magnetic domain structure. The observation of microscopic magnetic domain structure is an evidence of microscopic ferromagnetism and also a key to realize spintronic applications such as current-induced magnetic domain wall motion. In this dissertation, I clearly observed magnetic domain structure in (Ti,Co)O_2 at room temperature for the first time. Magnetic force microscope operated under vacuum condition enabled to resolve the individual magnetic domains, from which the micromagnetic parameters were also evaluated. In addition, I was able to relate the evolution of magnetic domain structure with the carrier density as well as the magnetization from bulk measurement. This result is consistent with the carrier mediated ferromagnetism reported previously.

To protect the film from magnetically dead layer at the surface, non-magnetic capping layer was developed in this experiment. With only a 2 nm-thick capping layer, the improved magnetization as well as magnetic anisotropy of anatase (Ti,Co)O_2 was observed at 300 K. By using the capping layer, the film thickness was able to be decreased

to very thin thickness with maintaining the magnetization. As a result, the magnetic domain structure in ultrathin film was successfully observed at room temperature because of improved surface magnetization. In addition, the stability of film was substantially improved by the capping layer.

In order to investigate the origin of high T_C , the T_C vs. carrier density relationship was systematically studied. The T_C of anatase (Ti,Co)O_2 thin films as function of carrier density was investigated by using electrical transport and magnetization measurements at lower temperature than T_C in order to avoid unintentional change of carrier density at high temperature. A non-monotonic relationship of T_C vs. carrier density was obtained implying a formation of bound magnetic polarons in addition to carrier-mediated interaction. Some possible substructures which could response for the nucleation of magnetic polarons, were proposed by using density functional theory (DFT) calculation.

In conclusion, I succeeded in observing magnetic domain structure in (Ti,Co)O_2 at room temperature and microscopic ferromagnetism was confirmed by homogeneous emergence of magnetic domains. I also developed non-magnetic capping layer to protect surface oxidation resulting in the fabrication of ultrathin magnetically active film. The first report of systematic study of T_C vs. carrier density relationship in (Ti,Co)O_2 was presented suggesting a non-monotonic relationship. This suggests a possibility of bound magnetic polarons in concert with carrier-mediated interaction which electrons play an important role. It is expected that these results will contribute to magnetic domain manipulation and future development of spintronics devices using this compound. Furthermore, the presently proposed ferromagnetic mechanism could also provide a guideline to explore new high T_C ferromagnetic semiconductors.

Acknowledgements

First of all, this Ph.D. thesis was successfully finished with the tremendous support from my supervisor, Prof. Tetsuya Hasegawa, who always gives me his advice and encouragement for my academic study. Moreover, whenever I faced any difficulties, Prof. Hasegawa always inspires me and supports me to pass through those circumstances. Besides, he motivated me to have a great chance to be a part of Advanced Leading Graduate Course for Photon Science (ALPS) program during my Ph.D. program.

I would like to give my great thanks to Prof. Tomoteru Fukumura who has been promoted to Tohoku University. He always gives me very useful advice and also understands and supports me with patience and kindness through my research. He is my inspiration to work hard and learn more all what I still do not understand. Not only, the knowledge I have learned from him, but also life experience in Japan.

I am also grateful to Dr. Hideyuki Kamisaka. His advice on computational simulation supported me for doing research with a benefit of programming. Assoc. Prof. Yasushi Hirose and Assist. Prof. Akira Chikamatsu, have given me their thoughtful discussions about my experiment. And I am also appreciated Mr. Shoichiro Nakao (KAST, Hasegawa Group) for the helps in instrument and equipment support.

Thanks to Dr. Daisuke Ogawa, Dr. Jie Wei, Mr. Shungo Kojima, Mr. Ryosuke Sei, Mr. Kenichi Kaminaga, Mr. Kyouhei Yamatake, Mr. Yutaka Uchida and Mr. Dai Kutsuzawa and Mr. Shunsuke Shibata as the members of the same project's group who always discuss and support my experiments.

Thanks for experimental supports to other members who are or have ever been in Solid State Chemistry Lab. of Univ. of Tokyo; Mrs. Anri Watanabe, Mr. Tsukasa

Katayama, Mr. Jeon Il, Mr. Shun Inoue, Ms. Xi Shen, Ms. Mayuko Oka, Ms. Kaori Kurita, Mr. Ryosuke Takagi, Mr. Tomoya Onozuka, Mr. Keisuke Kawahara, Mr. Yuji Kurauchi, Mr. Ryota Kantake, Mr. Fahd S. Kahn, Mr. Naoaki Hashimoto and Keisuke Yamada, and also members in Hasegawa Group at KAST; Dr. Sohei Okazaki, Dr. Chang Yang, Dr. Youngok Park, Mr.Atsushi Suzuki, Mr. Kazuki Aizawa, Mr. Kenta Shimamoto, Mr. Masahito Sano, Mr.Jumpei Takahashi, Mr. Vitchaphol Motaneeyachart, Mr. Takanori Yamazaki and Naoki Kashiwa. I always enjoy talking and sharing my life in Japan with them. And I must thanks to the secretaries of Hasegawa group, Mrs. Mie Umino and Mrs. Miki Komazawa.

I would like to give special thanks to Japanese government for MEXT scholarships as my financial supports along my master course in the University of Tokyo. And, I am also appreciated the academic funding for my research from Marubun foundation during the final year of this Ph.D. course.

Finally, my deepest gratitude to my family and my friends who always make me feel comfortable and relax from my research works and also support me with daily life in Japan.

Contents

Chapter 1

General introduction

1.1 Diluted magnetic semiconductors

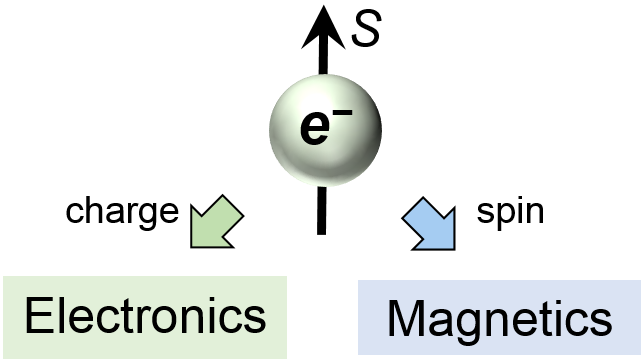

Figure 1.1 Schematic concept of spintronics combining information of electrical charge and magnetic spin representing both electric and magnetic property.

Spintronics has attracted much attention as a next generation of technology to realize high performance electronic devices because it combines both features of electrical charges and magnetic spins of electron carriers. With both degrees of freedom, spintronics clearly differs from conventional semiconductor based electronic and magnetics that utilize only either charges or spins. Examples of applications in this field are read head in hard disk drive, magnetoresistive random access memory (MRAM), spin effect transistor and etc.

Functional ferromagnetic semiconductor or diluted magnetic semiconductor is a key material for spintronics [1]. As its name, it combines both semiconducting and magnetic properties. It consists of semiconducting host doped with magnetic element as shown in Figure 1.2. Ferromagnetic semiconductor is a compound in between magnetic material containing periodically arranged magnetic atoms and non-magnetic semiconductor. The magnetic moment of the dopants in ferromagnetic semiconductor can interact with each

other via carriers which can be either electrons or holes, through $sp-d$ exchange interaction. In this system, magnetic property can be chemically or electrically controlled by charge carriers.

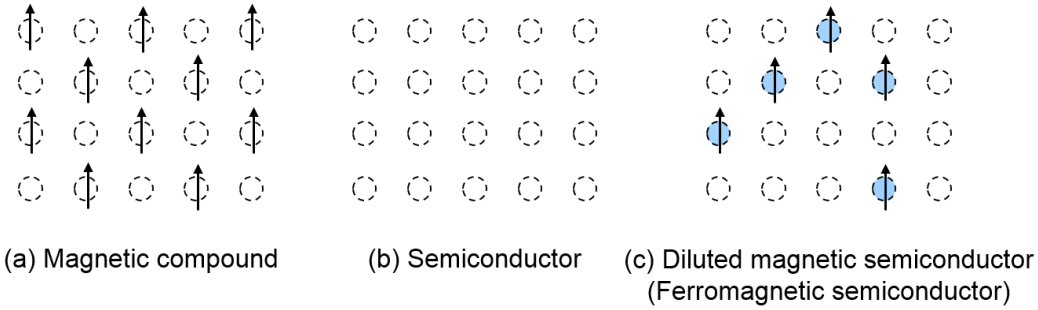

Figure 1.2 Illustration of (a) magnetic compound (b) semiconductor and (c) a diluted magnetic semiconductor. Blue circles represent magnetic dopants and arrows represent magnetic spin.

Various Mn-doped II-VI compounds, for example, ZnS, ZnTe, CdS, CdTe, etc., were investigated in an early stage. The dopant Mn^{2+} ions can substitute divalent cation in the host without introducing carriers. Continuously, Mn-doped III-V compounds (InAs, GaAs, etc.) were intensively studied by utilizing thin film technique with epitaxial stabilization of host compound which leads to high solubility of Mn content. In III-V host, Mn^{2+} ions substitute trivalent cations generating hole carriers. A sufficient amount of carriers can mediate ferromagnetic exchange coupling between localized magnetic spins of Mn. Among the Mn-doped III-V semiconductors, (Ga,Mn)As was considered as archetypal ferromagnetic semiconductor since it has been investigated from both fundamental and practical viewpoints despite the low Curie temperature (T_C) around 190 K [2]. Low ferromagnetic Curie temperature in most ferromagnetic semiconductors limits their practical interests. However, a discovery of room temperature ferromagnetic oxide semiconductors with high T_C lead us to expectation for their practical uses though more investigation and development are sill necessary.

1.2 Ferromagnetic oxide semiconductor

Wide-gap oxide semiconductors with good electrical conductivity have been widely used in various applications such as solar cells, transistor and photocatalysis. The advantages of wide-gap oxides materials are high transparency, high chemical stability, environmental friendliness and availability of many material forms, such as bulk, thin film and nanoparticles. In addition, high carrier density (n-type) can be easily controlled via the amount of oxygen vacancies acting as electron donors. Several techniques for fabrication of thin films such as molecular beam epitaxy (MBE), sputtering, and pulsed laser deposition (PLD), where epitaxial stabilization can be applied, have been well-established. In the oxide compounds, it is expected that heavy electron mass will benefit the strong ferromagnetic exchange interaction via carrier induced ferromagnetism such as Ruderman-Kittel-Kasuya-Yosida (RKKY) and may result in high T_C which will lead to fascinate applications at room temperature.

Most of studies have paid attention to ferromagnetic oxide semiconductors based on ZnO and TiO_2, while few studies to magnetically doped In_2O_3 and SnO_2.

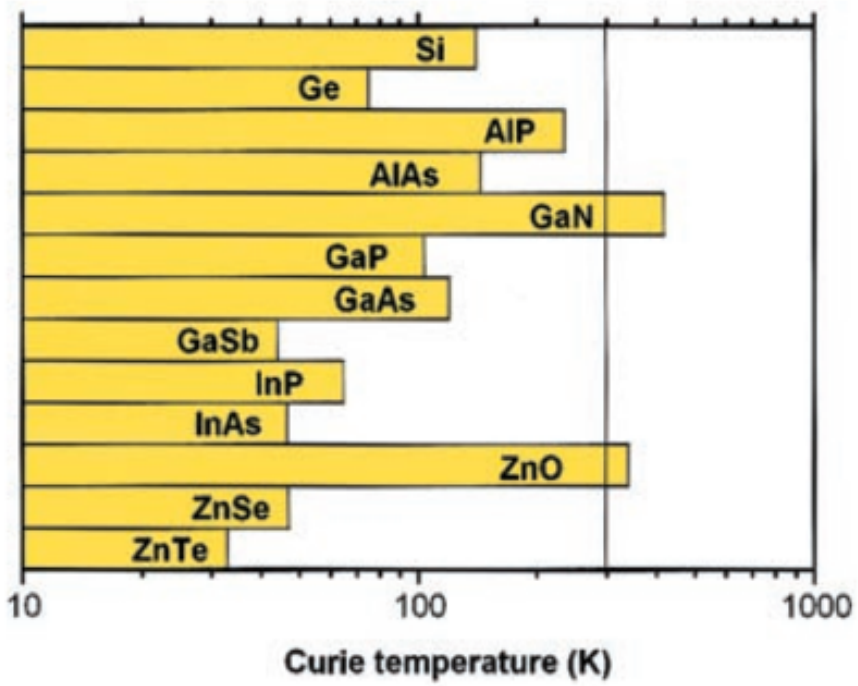

Figure 1.3 Theoretical prediction of T_C in various p-type semicondutors from T. Dietl, H. Ohno, F. Matsukura, J. Cibert, and D. Ferrand, *Science* **287**, 1019 (2000). Reprinted with permission from AAAS.

From the band calculation studies, room temperature ferromagnetism was predicted in p-type ferromagnetic semiconductors including ZnO (Figure 1.3) [3]. Various transition metals doped ZnO materials were firstly developed with T_C scattering in a range of 30-550 K [4–7]. (Zn,Mn)O is reported to show the properties similar to those of typical Mn-doped II-VI compounds (CdTe, CdSe), and hence has been argued as a member of II-VI group with oxygen anion [8].

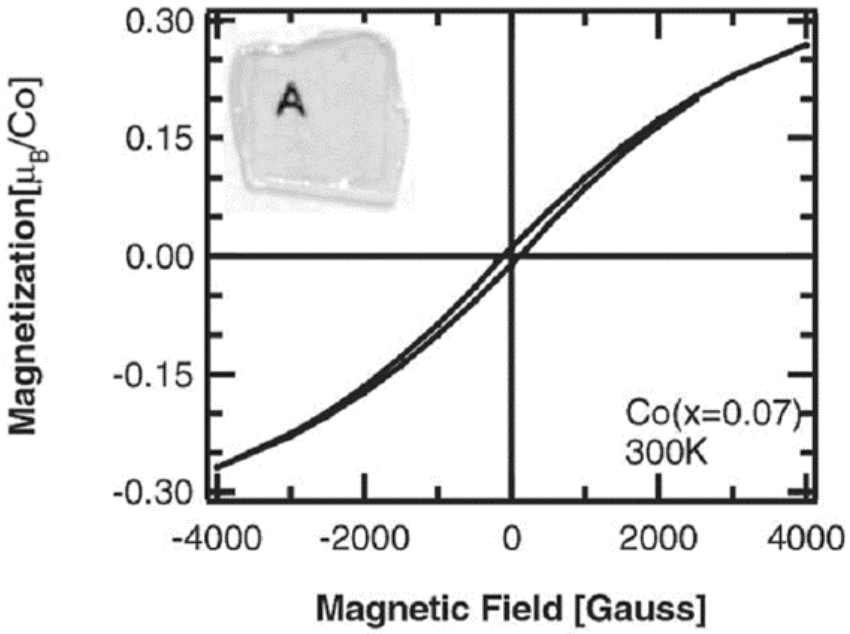

Figure 1.4 Magnetization curve at 300 K of anatase $Ti_{0.93}Co_{0.07}O_{2-\delta}$. Inset shows image of the sample indicating its high transparency from Y. Matsumoto, M. Murakami, T. Shono, T. Hasegawa, T. Fukumura, M. Kawasaki, P. Ahmet, T. Chikyow, S. Koshihara, and H. Koinuma, *Science* **291**, 854 (2001). Reprinted with permission from AAAS.

Another most employed host semiconductor is TiO_2 ($Ti_{1-x}Co_xO_2$; (Ti,Co)O_2). Both Co-doped rutile and anatase TiO_2 as transparent ferromagnetic oxide semiconductor were intensively studied since the discovery of room temperature ferromagnetism (Figure 1.4) [9]. A few studies investigated the doping of other transition metals such as Cr, V, Fe and Ni into TiO_2 and reported ferromagnetism with T_C above room temperature [10]. However, due to lack of development for high quality films, investigation on these transition metals doped TiO_2 is less compared to that of (Ti,Co)O_2. Therefore, among several ferromagnetic semiconductors, Co-doped TiO_2 become a promising candidate for room temperature spintronic application and hence is widely studied for both fundamental understanding and controlling of physical properties.

1.3 Room temperature ferromagnetic oxide semiconductor, Co-doped TiO_2

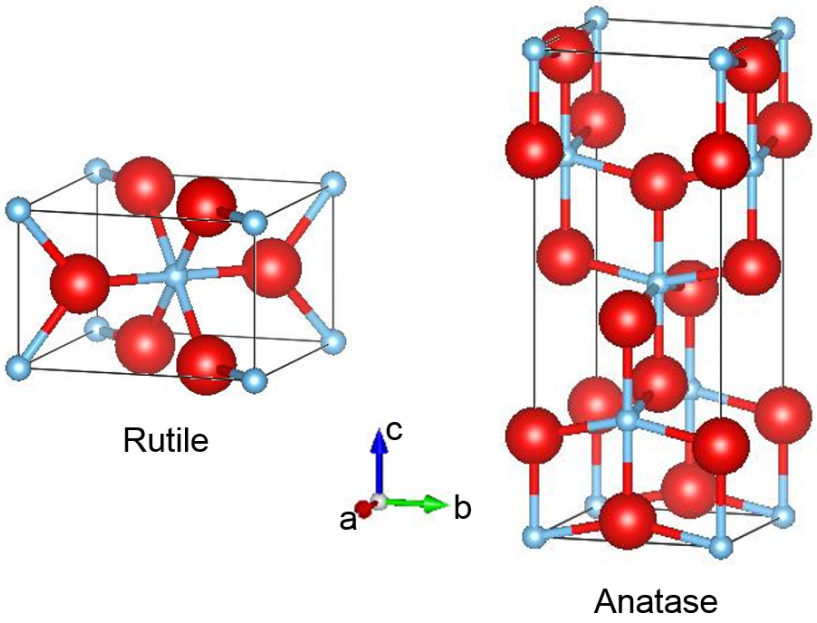

Figure 1.5 Crystal structures of rutile and anatase TiO_2.

The crystal structures of rutile and anatase TiO_2 are shown in Figure 1.5. Compared to the rutile structure which is the most thermodynamically stable polymorph, the metastable anatase turned out to have high efficiency for catalytic applications and solar cells. In addition, the higher electron mobility in anatase phase attracted researchers to study on anatase Co-doped TiO_2.

Curie temperature of Co-doped TiO_2 ($(Ti,Co)O_2$) was reported to be very high ~ 600 K [11]. Several reports on magnetization suggested ferromagnetic hyteresis with saturation magnetization $\lesssim 2\ \mu_B$/Co and coercivity less than 500 Oe by SQUID magnetometer. However, some researchers doubted whether these are intrinsic properties of

---

The structures shown here were produced by VESTA software; K. Momma and F. Izumi,"VESTA 3 for three-dimensional visualization of crystal, volumetric and morphology data," *J. Appl. Crystallogr.*, **44**, 1272-1276 (2011).

(Ti,Co)O_2 or originate from any magnetic Co clusters with direct interaction of local moments. This issue was later clarified, that is, intrinsic ferromagnetism was proven based on the measurement of ferromagnetic magneto-optical effect, anomalous Hall effect and x-ray photoemission spectroscopy (XPS).

Finding of ferromagnetic magneto-optical effect by magnetic circular dichroism (MCD) measurement indicated the interaction between carriers and ferromagnetic dopants which was observed as the ferromagnetic response at the band edge of TiO_2 host [12]. Another important evidence is the clearly observed anomalous Hall effect in (Ti,Co)O_2 indicating that the ferromagnetism responses with charge carriers (electrons) [13]. This kind of long-range interaction between carriers supports the intrinsic ferromagnetism since ferromagnetic Co clusters shall not respond to the change of carriers in the host. In addition, XPS measurements revealed that Co exists in TiO_2 as Co^{2+} ions with high spin configuration and strong hybridization between carriers in Ti 3*d* band and localized t_{2g} of Co^{2+} was suggested from the shift of binding energy [14]. Therefore, the intrinsic ferromagetism in (Ti,Co)O_2 was confirmed.

Although a presence of high spin Co^{2+} ions was proven, some research groups reported a possibility that Co nanoclusters were formed at the substrate/film interface [15]. Thus, fabrication of high quality thin films without any cluster is strongly desired. Thin film growth of (Ti,Co)O_2 with segregation-free was well-established by utilizing pulsed laser deposition under ultrahigh vacuum where higher Co content than the thermodynamic solubility limit can be obtained. The keys to obtain (Ti,Co)O_2 can be summarized as follows:

- *Substrate materials*: In order to obtain rutile (Ti,Co)O_2, sapphire substrate is usually used while anatase (Ti,Co)O_2 can be grown on perovskite oxide substrates such as $LaAlO_3$ and $SrTiO_3$. The lattice matching between thin film and substrate

is important because epitaxial stabilization from the substrate assists 2D-growth resulting in high solubility of Co content.

- *Growth atmosphere*: Ultrahigh vacuum background atmosphere is preferable to finely control the oxygen partial pressure during the deposition because the oxygen partial pressure significantly affects the amounts of oxygen vacancies and electron carriers in the film.

- *Growth temperature*: By using low growth temperature, high quality surface of the film can be obtained. In addition, a possibility of segregation is reduced. In order to obtain a crystallized film at low temperature, buffering technique is known to be effective.

By utilizing TiO_2 buffer layer, homoepitaxial growth of both high quality rutile and anatase $(Ti,Co)O_2$ films were successfully achieved indicating the effectiveness of buffering technique. Figure 1.6 shows XRD pattern and AFM image of high quality anatase epitaxial $(Ti,Co)O_2$ thin film grown on anatase TiO_2 buffer layer at low temperature [16]. In addition, microanalysis of the sample with bright-field scanning transmission electron microscopy (STEM) and the energy-dispersive x-ray spectroscopy (EDS) mapping suggested that Co atoms homogeneously dispersed throughout the film without any clustering or segregation inside the film or at film/substrate interface (Figure 1.7).

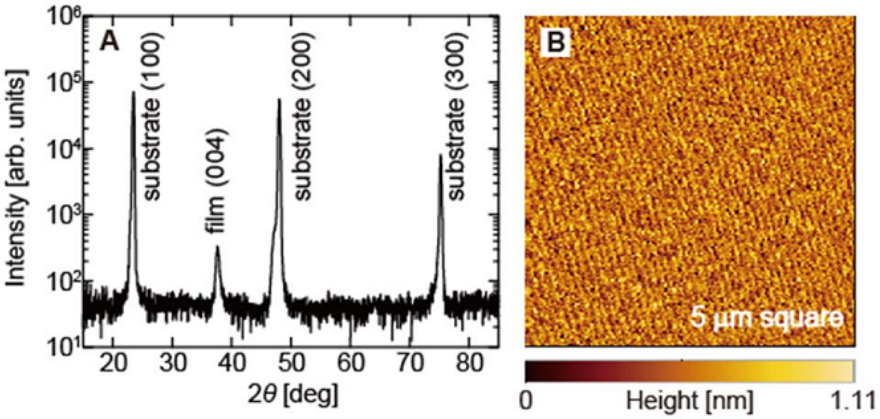

Figure 1.6 (A) X-ray diffraction pattern of anatase $Ti_{0.90}Co_{0.10}O_{2-\delta}$ (001) film/anatase TiO_2 buffer layer/$LaAlO_3$ (001) substrate and (B) its atomic force microscope image from Y. Yamada, K. Ueno, T. Fukumura, H. T. Yuan, H. Shimotani, Y. Iwasa, L. Gu, S. Tsukimoto, Y. Ikuhara, and M. Kawasaki, *Science* **332**, 1065 (2011). Reprinted with permission from AAAS.

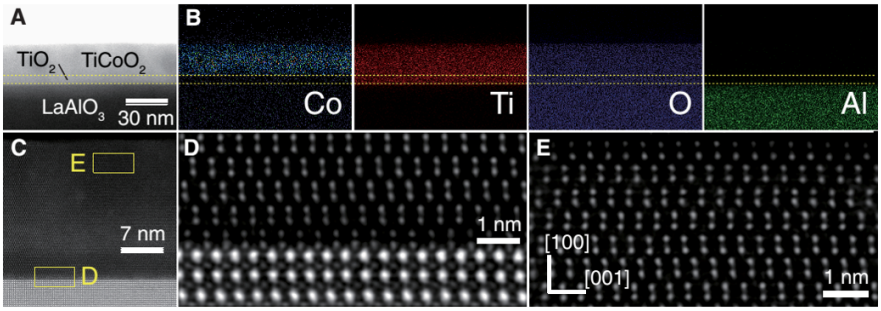

Figure 1.7 (A) STEM image and (B) EDS mapping of of anatase $Ti_{0.90}Co_{0.10}O_{2-\delta}$ (001) film. (C) STEM image near film/substrate interface, (D) and (E) are zoom-in region in (C). From Y. Yamada, K. Ueno, T. Fukumura, H. T. Yuan, H. Shimotani, Y. Iwasa, L. Gu, S. Tsukimoto, Y. Ikuhara, and M. Kawasaki, *Science* **332**, 1065 (2011). Reprinted with permission from AAAS.

Besides the establishment of growth conditions for $(Ti,Co)O_2$ films, the transport and magnetic properties have also been investigated extensively. The electron carriers in $(Ti,Co)O_2$ films can be controlled via chemical doping [13] or field gating [16]. Recently, paramagnetic to ferromagnetic switching induced by electric field gating at room temperature was successfully performed in an electric double layer transistor (EDLT) with anatase $(Ti,Co)O_2$ channel. Figure 1.8 shows electric field dependence of anomolous Hall effect at 300 K of anatase $Ti_{0.90}Co_{0.10}O_{2-\delta}$ (001) film. By applying an external

electric field, electron carriers were induced into the film and ferromagnetic hysteresis loop was obtained. This result indicates the important role of electron carriers to the ferromagnetism in (Ti,Co)O_2. This is also an important step for future applications of ferromagnetic semiconductors with gate-control ferromagnetism at room temperature although all solid-state device which is more preferable, is still needed to be developed.

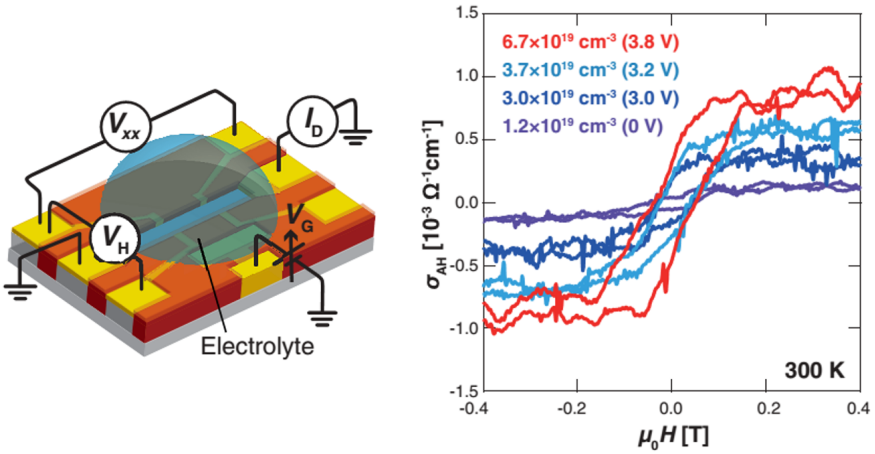

Figure 1.8 (left) Schematic structure of an electric double layer transistor (EDLT) with anatase (Ti,Co)O_2 channel and (right) electric field dependence of anomolous Hall effect at 300 K of anatase $Ti_{0.90}Co_{0.10}O_{2-\delta}$ (001) film from Y. Yamada, K. Ueno, T. Fukumura, H. T. Yuan, H. Shimotani, Y. Iwasa, L. Gu, S. Tsukimoto, Y. Ikuhara, and M. Kawasaki, *Science* **332**, 1065 (2011). Reprinted with permission from AAAS.

The studies of anatase (Ti,Co)O_2 have been done in various approaches which especially includes the investigations on intrinsic magnetization, optimal film growth condition for high quality films and, the control of magnetization via electron carriers. However, there are some issues that are still needed to be examined. The first issue is how the ferromagnetism appears in a microscopic scale and also magnetic domain structure as functions of sample parameters. The second issue is related to a limitation of ferromagnetic materials with surface magnetically dead layer which obstruct practical applications. And, the last issue is what origins and mechanisms for the high T_C in (Ti,Co)O_2 are. In the following sections, the details of these topics will be introduced.

1.3.1 Magnetic domain structure

The magnetic domain [17] is a uniform direction of magnetization resulting from total free energy minimization to reduce exchange potential between magnetic moments. There are six terms of energy that may have to be considered:

$$E_{total} = E_{ex} + E_a + E_d + E_Z + E_{stress} + E_{ms}. \tag{1.1}$$

The first three terms are energies caused by exchange, magnetocrystalline anisotropy and the demagnetizing field which always present in ferromagnetic materials. The other three terms are the response to an applied field, stress and magnetostriction, respectively. These last three terms may sometimes be neglected due to its small contribution.

At temperature lower than T_C, a ferromagnetic material will form a magnetic domain structure spontaneously. Magnetic domain separated by boundaries (magnetic domain wall) is governed by the competition of two main factors between magnetocrystalline anisotropy (E_a) which is minimized by aligning magnetization along an easy axis, and demagnetization energy (E_d) which is reduced by minimizing the length of magnetic loop outside the material. When a magnetic domain structure is formed, several micromagnetic parameters such as domain size, domain wall width and magnetic stiffness constant can give quantitative understanding of intrinsic properties in the materials.

Several measurement techniques such as scanning superconducting quantum interference device (SQUID) microscopy, magnetic force microscopy (MFM) and scanning Hall probe microscopy have been developed for magnetic domain observation. For (Ga,Mn)As, a well-know III-V ferromagnetic semiconductor, the magnetic domain structure was reported to be a conventional stripe shape observed under no external magnetic field [18, 19]. The domain size is generally in an order of μm. One example of magnetic domain applications is current induced magnetic domain wall propagation which is applicable to memory devices. This kind of memory device is based on the concept of

spin-polarized current induced magnetic reversal via spin transfer (Figure 1.9) which is an alternative way beside of conventional concept using external magnetic field. Racetrack memory was proposed by Parkin et al. suggesting a promising nonvolatile memory device [20]. The racetrack, having both vertical and horizontal structures, is a ferromagnetic nanowire containing data as a pattern of magnetic domains. These domains can shift by using spin-polarized current. By integrating an array of racetrack on a chip such as Si, 3D microelectronic device and high-density storage may be achieved.

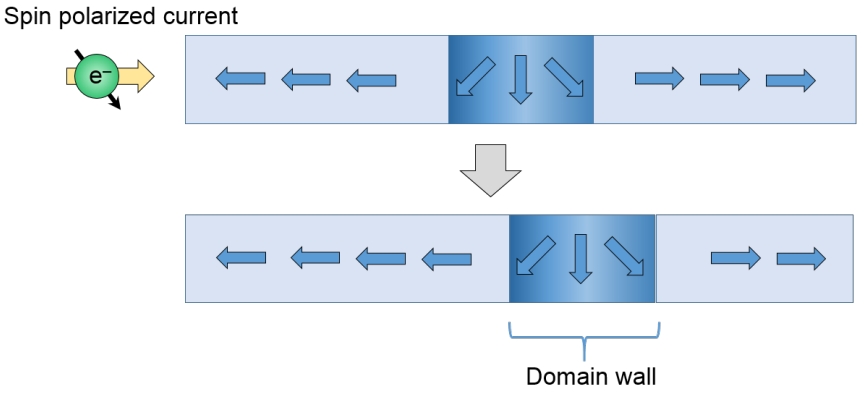

Figure 1.9 Schematic concept of spin-polarized current induced magnetic domain wall propagation.

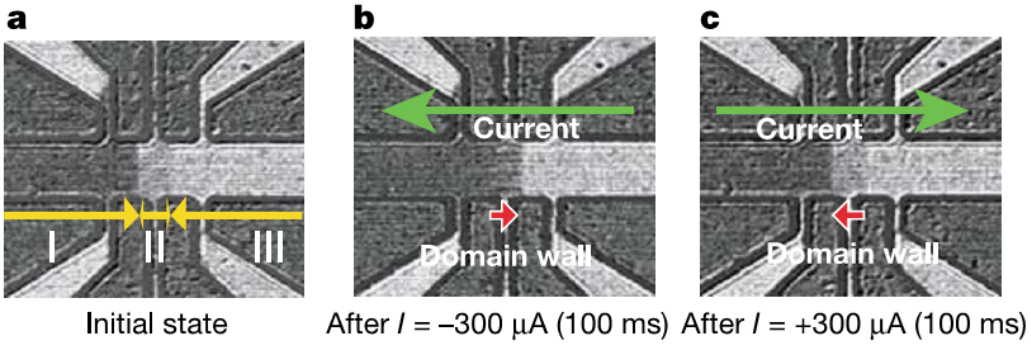

Figure 1.10 Domain wall propagation induced by electrical current observed by magneto-optical Kerr effect microscope at ∼80 K. (a) Initial state with magnetic domain wall in the region II (b) After the application of negative current pulse (c) After the application of positive current pulse. Reprinted by permission from Macmillan Publishers Ltd: Nature [21], copyright 2004.

The magnetic domain wall propagation was studied in several ferromagnetic metals

such as NiFe alloy [22], Co nanowires [23,24] and CoFe [25]. Recently, it was also successfully performed in a ferromagnetic semiconductor (Ga,Mn)As [21,26,27] as shown in Figure 1.10 despite its low Curie temperature. By using positive and negative current, the magnetic domain wall can shift to the opposite directions. The domain wall switching can be achieved by using low current density of 10^5 Acm^{-2}, much lower than that 10^7 Acm^{-2} required for ferromagnetic metal.

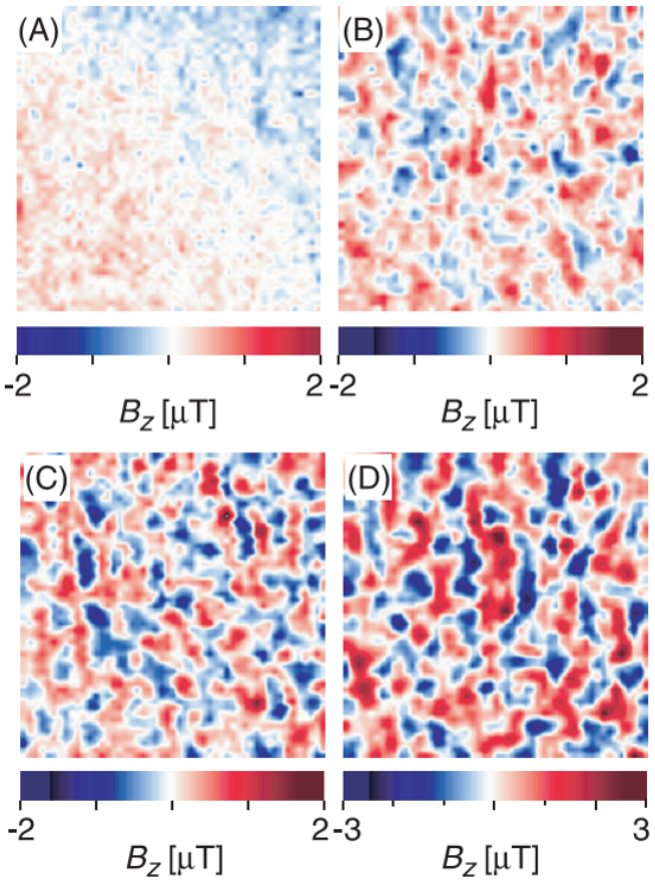

Figure 1.11 Magnetic domain structure of anatase $Ti_{1-x}Co_xO_{2-\delta}$ thin film with x = (a) 0%, (b) 2%, (c) 3% and (d) 6% measured by scanning SQUID microscope at 3 K from Y. Matsumoto, M. Murakami, T. Shono, T. Hasegawa, T. Fukumura, M. Kawasaki, P. Ahmet, T. Chikyow, S. Koshihara, and H. Koinuma, *Science* **291**, 854 (2001). Reprinted with permission from AAAS.

For both anatase [9] and rutile [28] (Ti,Co)O_2 , the microscopic magnetic domain structures were obtained by scanning SQUID microscope at low temperature despite a coarse spatial resolution of μm. Figure 1.11 shows the magnetic domain structure of

anatase $Ti_{1-x}Co_xO_{2-\delta}$ thin film with different Co contents observed by scanning SQUID microscopy, which resolve magnetic domains of $\sim$20 μm. In contrast, no magnetic domains were observable in pure anatase TiO_2 [9]. However, further investigation of the magnetic domain structure at room temperature, particularly its dependency on sample parameters is still required.

Generally, magnetic domain structure can be obtained at room temperature by using magnetic force microscope (MFM) which posses higher lateral resolution. A number of room temperature ferromagnetic oxide semiconductors were reported based on transition metal doped TiO_2, which includes Ni [29], Fe [30], V [10, 31, 32] and Cr [31] doped TiO_2. Since the principle of MFM is based on the interaction between the sample and the magnetic probe during the measurement, the obtained data sometimes contains both surface and magnetic information. The deduction of surface information can be achieved by using two successive scanning method, however, very rough surface morphology can not be completely subtracted. For $(Ti,Co)O_2$ thin films, the observation of magnetic domain structure was also attempted at room temperature by using MFM as shown in Figure 1.12. The figure indicates large effect of grain boundaries and also surface effect as clearly seen from dark spots in the square and circle areas. Other reports on anatase $(Ti,Co)O_2$ also attempted to obtain clear magnetic domain structure but most of them faced the problem of rough surface and small remanent magnetization resulting in failure to detect distinct domain like signal [33, 34].

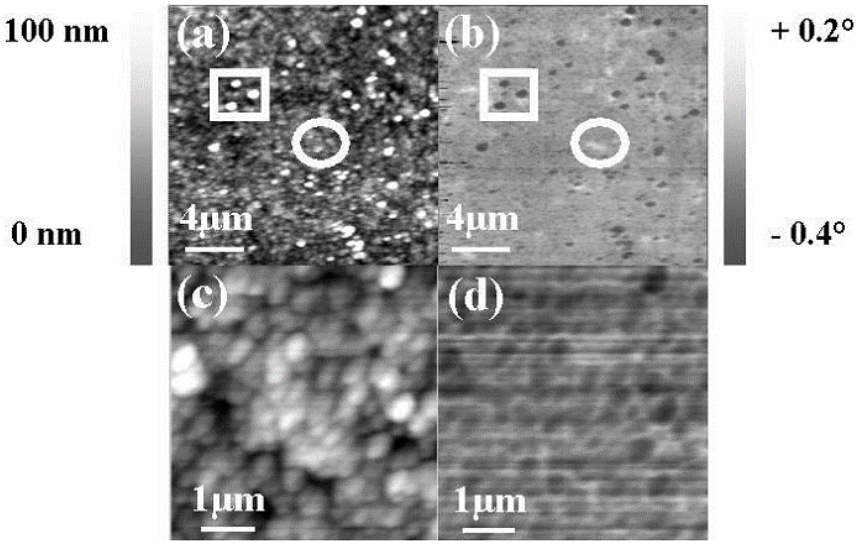

Figure 1.12 (a) Topographic (b) the corresponding MFM image of anatase $(Ti,Co)O_2$ films in the measurement area of $20 \times 20 \mu m^2$. (c) and (d) are zoom-up images of (a) and (b) in an area of $5 \times 5 \mu m^2$. Square and circle are for an eye-guide of the same region [35]. © IOP Publishing. Reproduced with permission. All rights reserved. *

Therefore, high quality films are required to investigate more details of magnetic domain structure in anatase $(Ti,Co)O_2$ films with sensitive MFM measurement. Here, the recently well-established fabrication condition will be useful to obtain atomically flat $(Ti,Co)O_2$ films. The microscopic study of anatase $(Ti,Co)O_2$ films is an important task to relate its bulk ferromagnetism to the microscopic magnetic domain which will give one evidence for microscopic ferromagnetism and also another step for magnetic domain manipulation by using room temperature ferromagnetic semiconductors.

1.3.2 Magnetically dead layer

Magnetically dead layer is one of the common issue for magnetic materials. Generally, the dead layer exists at surface or interface of both forms in bulk and thin film. For example, NiFe alloy films showed about 1 nm-thick dead layer. In this case, the

*Original link to the article (DOI): 10.1088/0953-8984/16/30/015

thickness of the dead layer depended on the thickness of interfacial seed layer or surface capping layer of Ta due to intermixing at the interface [36]. For CoFeB ferromagnetic metal films, the intermixing between films and substrate also generated noncollinear spin region which is magnetically inactive [37]. A perovskite oxide, (La,Sr)MnO_3, also showed magnetically dead layer with magnetic disorder at surface probably associated with structural disorder [38, 39]. For $SrRuO_3$ films, the surface oxidation might induce structural defect resulting in the formation of the dead layer [40]. The origins of magnetically dead layer are mainly categorized to surface/interface disordering and surface oxidization. For oxide compounds, the surface oxidation is usually found at which the oxygen compensation takes place spontaneously at ambient condition.

For (Ti,Co)O_2 films, magnetically dead layer was found in both rutile and anatase form clearly evidenced from x-ray magnetic circular dichroism (XMCD) measurement [41, 42]. The XMCD measurement with total electron yield (TEY) and total fluorescence yield (TFY) modes were used to reflect surface and bulk magnetic properties, respectively. Figure 1.13 shows the result of magnetization as a function of magnetic field obtained from XMCD with TFY mode (bulk sensitive) and TEY mode (surface sensitive) of anatase $Ti_{1-x}Co_xO_{2-\delta}$ films compared with magnetization curves obtained from SQUID magnetometer [42]. For metallic and intermediate films, the carrier density is high enough to mediate ferromagnetic interaction and results in large magnetic moment of Co ~ 2 μB/Co obtained from SQUID magnetometer. Whereas, the insulating sample showed a decreased magnetization due to lack of carrier density. The magnetization from TFY mode well agreed with bulk measurement from SQUID magnetometer whereas significantly decreased magnetization was observed at the surface by TEY mode. The thickness of the magnetically dead layer was deduced to be ~ 5 nm according to probing depth of TEY mode.

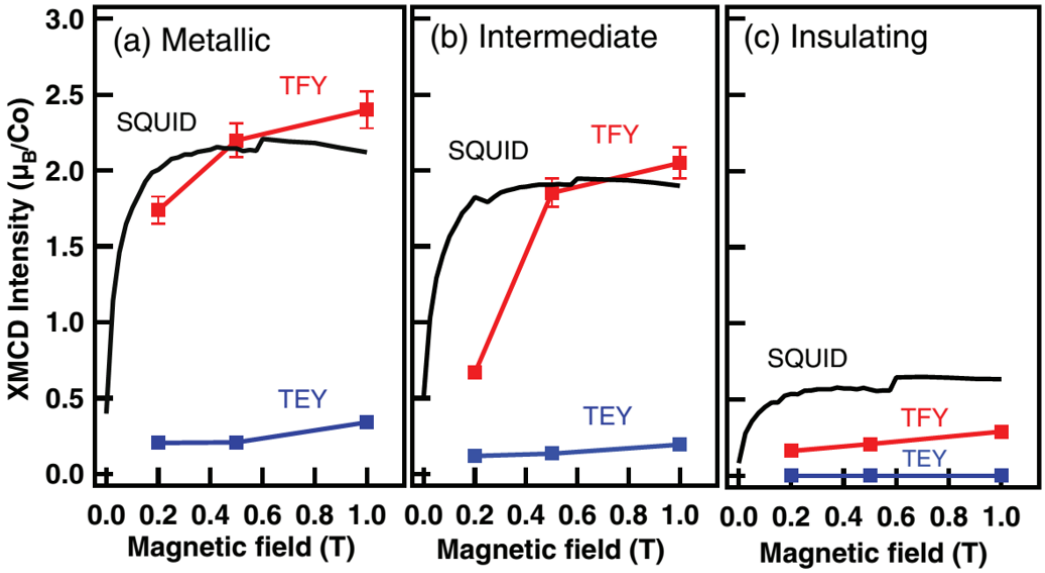

Figure 1.13 Magnetization obtained from XMCD with TFY mode and TEY mode of anatase $Ti_{0.95}Co_{0.05}O_{2-\delta}$ films compared with magnetization curves obtained from SQUID magnetometer. Reprinted with permission from V. R. Singh, K. Ishigami, V. K. Verma, G. Shibata, Y. Yamazaki, T. Kataoka, A. Fujimori, F.-H. Chang, D.-J. Huang, H.-J. Lin, C. T. Chen, Y. Yamada, T. Fukumura, and M. Kawasaki, *Appl. Phys. Lett.* **100**, 242404 (2012). Copyright 2012, AIP Publishing LLC.

According to the experiment on photoinduced carriers, the origin of magnetically dead layer in (Ti,Co)O_2 films might attribute to oxidation where surface depletion layer was formed with less carriers compared to bulk region [43]. By illuminating the sample with ultraviolet light, x-ray photoemission spectroscopy (XPS) detected the shift of binding energy indicating that the photoinduced carriers were generated and ejected into the depletion layer. This suggested that the depletion layer due to the band bending with Co spins disordering could be resolved by photoinduced carriers resulting in alignment of Co spins. The thickness of depletion layer was dependent on the carrier density in the films and was found to vary from several nanometers to several ten nanometers.

As the consequence of dead layer, when decreasing film thickness, the film loses its magnetic properties. This is important especially when applying materials to devices such as all-solid-state transistor which requires thin channel layer. In general, the most

effective method to recover the magnetically dead layer with surface disordering is annealing while applying capping layer is known to be a common method to protect surface oxidation [44–47]. For anatase (Ti,Co)O_2 films with surface depletion layer, the capping layer might be useful to avoid decreased surface magnetization.

1.3.3 High T_C ferromagnetism

Room temperature ferromagnetic semiconductor is a promising material for spintronic application but so far, there is still lack of understandings how the material can exhibit high T_C which is important information in order to design new high T_C materials. The mechanism of high T_C in (Ti,Co)O_2 is also unclear despite a long debate on this issue.

Generally, there are two main ferromagnetic mechanisms. One is *carrier mediation* in which mobile carriers play an important role to mediate the exchange coupling between magnetic impurity spins. Another mechanism is *bound magnetic percolation* or *bound magnetic polarons* in which carriers are mainly localized and magnetic impurity spins are bound around them by antiferromagnetic interaction to form so called magnetic polarons. The ferromagnetism emerges when those polarons overlap with ferromagnetic exchange interaction between them. The carrier mediation and bound magnetic percolation are illustrated in Figure 1.14.

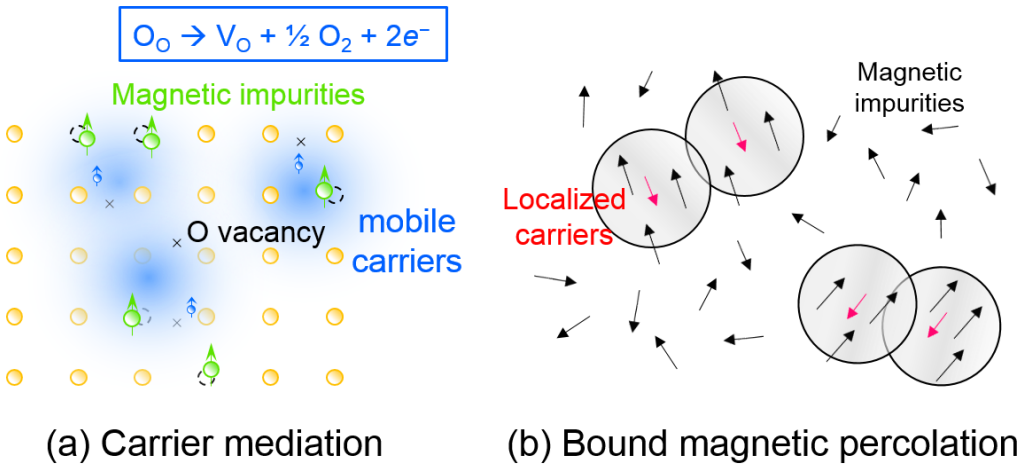

Figure 1.14 Illustration of two main ferromagnetic mechanisms: (a) carrier mediation and (b) bound magnetic percolation.

For (Ti,Co)O_2, both mechanisms of exchange coupling were proposed. An indirect exchange of bound magnetic polarons formed with localized carriers of shallow donors was suggested for a strongly insulating system probably associated with defect centers of oxygen vacancies [48, 49]. On the other hand, carrier mediated exchange coupling was also discussed with the evidences of carrier induced ferromagnetism [16, 43, 50]. In general, higher T_C might be expected in a conducting system rather than insulating system with the percolation since the polaron size will decrease significantly when temperature arises. Some groups also proposed that both mechanisms might cooperate together to generate high T_C [51, 52]. For example, thermally activated carriers might be taken into account, and thus a combination of percolation at low temperature and RKKY ferromagnetism at high temperature may result in high T_C in ferromagnetic oxide semiconductors.

In order to discuss about the high T_C mechanism, the relation of T_C vs. n (carrier density) is very useful. The relationships between T_C and n for carrier mediation and

bound magnetic percolation are described as the following equations:

$$k_B {T_C}^{RKKY} = \frac{1}{3} J {a_0}^3 \sqrt{n n_i} \sqrt{(S+1)(s+1)} \tag{1.2}$$

$$k_B {T_C}^{perc} \sim sSJ(\frac{a_0}{a_B})^3 ({a_B}^3 n)^{1/3} \sqrt{\frac{n_i}{n}} \exp(-\frac{0.86}{({a_B}^3 n)^{1/3}}) \tag{1.3}$$

where k_B, J, an a_0 are Boltzmann's constant, the exchange coupling constant, and lattice parameter, n and n_i are the density of carrier and magnetic impurity (density of dopant) and, s and S are the magnetic spins of carrier and magnetic impurity, respectively. ${T_C}^{RKKY}$ and ${T_C}^{perc}$ denote T_C for carrier mediation and bound magnetic percolation, respectively. Here, the monotonic relation of T_C vs. n is expected for carrier mediation mechanism while non-monotonic relation or a dome-shaped T_C vs. n is predicted for bound magnetic percolation.

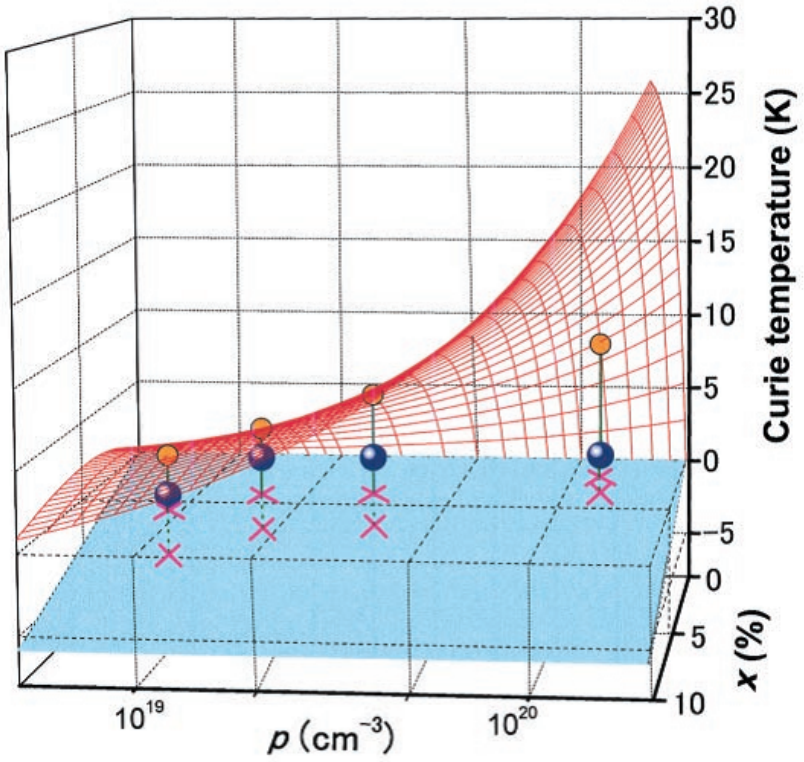

Figure 1.15 T_C of (Ga,Mn)As as functions of carrier (hole) density and Mn content. Blue spheres mark experimental data and red mesh and yellow spheres represent theoretical prediction by hole-induced ferromagnetic interaction from T. Dietl, H. Ohno, F. Matsukura, J. Cibert, and D. Ferrand, *Science* **287**, 1019 (2000). Reprinted with permission from AAAS.

For an archetypal ferromagnetic semiconductor, (Ga,Mn)As, T_C as functions of carrier (hole) density and Mn content has been studied both experimentally and theoretically as shown in Figure 1.15. The T_C of (Ga,Mn)As increases monotonically with both sample parameters indicating carrier-induced ferromagnetism [3, 53].

However, the systematic study of T_C in anatase (Ti,Co)O_2 as functions of carrier density and Co content has not been performed since the high T_C requires the measurement at high temperature at which spontaneous annealing occurs and alters the carrier density. Therefore, estimation of T_C by extrapolating the data measured at low temperature would enable the investigation of relation of T_C vs. n in a qualitative manner.

In addition, spinodal nanodecomposition was recently proposed to explain high T_C in (Ga,Mn)As, (Ga,Mn)N and other III–V ferromagnetic semiconductors [54, 55]. The concept of spinodal nanodecomposition is that each decomposition region has high T_C and when these regions correlate together, for example, by overlapping or contacting, the global high T_C of the material is obtained. The idea of spinodal nanodecomposition might be a clue of nucleation center of magnetic polarons.

For (Ti,Co)O_2 , a similar scenario was proposed that complexes of $Ti^{3+} - V_o - Co^{2+}$ might be responsible for its ferromagnetism and high T_C can be obtained even in low Co content films [56]. Recently, x-ray fluorescence holography (XFH) measurement revealed an existence of suboxidic structure embedded in rutile (Ti,Co)O_2 , which could be an alternative explanation for the high T_C instead of the previously proposed complexes [57]. Therefore, the study of substructures in anatase (Ti,Co)O_2 by means of theoretical prediction is important from a viewpoint of possible nucleation center.

1.4 Purposes of this study

As mentioned above, there are still some remaining issues of anatase (Ti,Co)O_2 compound: microscopic ferromagnetism, recovery of magnetically dead layer and origin of the high T_C . For the first topic, *microscopic ferromagnetism*, I conducted microscopic investigation of ferromagnetism in anatase (Ti,Co)O_2 thin film by means of the observation of magnetic domain structure. By utilizing well-established fabrication condition of anatase (Ti,Co)O_2 epitaxial thin film, magnetic domain structure were studied at room temperature in order to verify ferromagnetism from microscopic scale and correlate it to the bulk magnetization. Moreover, micromagnetic parameters as functions of both carrier density and Co content were examined. For the second topic, *recovery of magnetically dead layer*, I examined non-magnetic capping layer in order to improve surface magnetization and to obtain magnetically active (Ti,Co)O_2 film with thinner thickness. For the third topic, *high T_C ferromagnetism*, I systematically evaluated the T_C of anatase (Ti,Co)O_2 thin films as functions of carrier density and Co content from transport and magnetization properties at $T < 400$ K which are free from the effect of spontaneous annealing. I evaluated T_C from two independent measurements. The relation of T_C vs. n of anatase (Ti,Co)O_2 was investigated systematically. Moreover, possible local structures around Co which might relate to the origin of high T_C was also examined by using density functional theory (DFT) calculation.

From these studies, more understanding of microscopic ferromagnetism and its origin is expected. Furthermore, a practical method for preparing magnetically active (Ti,Co)O_2 film with less dead layer will be developed, which is useful for realizing the (Ti,Co)O_2-based spintronics devices.

Chapter 2

Experimental Techniques

In this chapter, the fabrication and characterization techniques will be described. The anatase $Ti_{1-x}Co_xO_{2-\delta}$ epitaxial thin films were fabricated by pulsed laser deposition (PLD) equipped with *in situ* reflection high energy electron diffraction (RHEED) system. In order to examine crystal structures of films, x-ray diffraction (XRD) measurement is performed. Electrical transport properties are investigated by four-probe measurement of Hall bar patterned samples from which temperature dependence of resistivity and also the resistivity under magnetic field can be measured. Magnetization and magnetic domain structure of the films were investigated by superconducting quantum interference device (SQUID) magnetometer and magnetic force microscope (MFM), respectively.

2.1 Pulsed Laser Deposition (PLD)

Among several thin film fabrication techniques such as chemical vapour deposition (CVD) or sputtering, pulsed laser deposition (PLD) is known as one of the physical methods suited for fabricating oxide thin films and especially multi-layer films. PLD technique is simple, cheap and versatile with a great benefit of easy controllability of the oxygen pressure during film fabrication. The partial gas pressure can be varied from Ultra-High Vacuum (UHV) to mTorr range leading to tunable crystal phase and oxygen stoichiometry of thin film [58, 59].

A schemetic of PLD system in this experiment is illustrated in Figure 2.1. There are two separated chambers, the load lock chamber (L/L) and the main chamber. Without interrupting the main chamber with high pressure atmosphere, samples or targets are first transferred into the L/L chamber and then transferred into the main chamber after

an optimal vacuum level is reached. Therefore, in the main chamber, high vacuum with low impurity gas can be maintained. In both L/L and main chamber, rotary pumps (RP) are used for pre-vacuum, and further evacuated by turbo molecular pumps (TMP) to base pressure of 10^{-9} Torr. The distance between target and substrate holder is fixed and spot sized of laser is known. During film fabrication, substrate temperature can be controlled in the main chamber by using a diode heating laser, which heats substrate from the back-side, and oxygen pressure can be controlled precisely through a variable leak valve (VLV). The target holder always rotates during film deposition in order to generate homogenous atomic plume of targets.

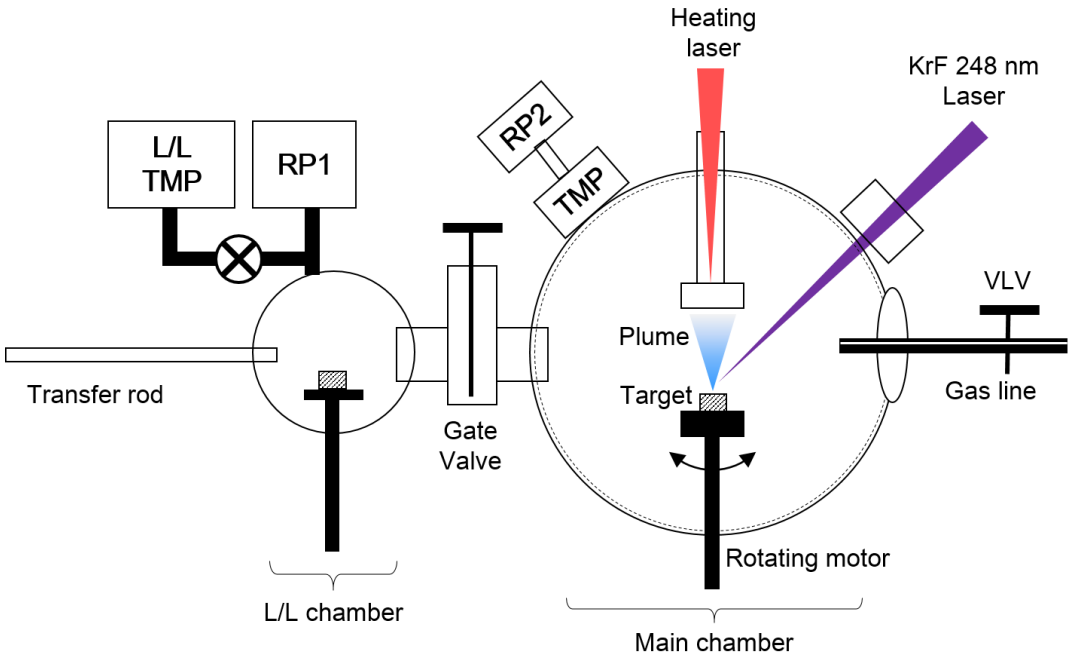

Figure 2.1 Schematic of pulsed laser deposition (PLD) chamber.

In general, the working processes of PLD in the main chamber are composed of initial laser-target interaction, propagation of the material's plume, and the eventual coating of gas phase species onto substrate [60]. When a ceramic target is ablated by the laser, plasma plume of target is firstly generated and all components in a ceramic target evaporate stoichiometrically. Then, the ionized or atomized plume will diffuse to the substrate

position. The diffusion process depends on the mass of each element, velocity, density of plume and background pressure in the chamber. Finally, film growth occurs when atoms and ions reach the substrate surface and lose their kinetic energy forming as a thin film. In this step, crystallization may happen, therefore the substrate temperature (temperature at the surface of substrate) is usually raised in order to promote nucleation and surface migration. The growth rate of film is determined by the diffusion-like process while growth mode or mechanism of film deposition depends on nucleation and migration processes.

In PLD technique, chemical doping into the films is relatively simple. By changing composition in a ceramic target, the generated plume may be assumed to consist of elements with the same composition ratios as the target due to high evaporation energy of pulsed laser. Consequently, the film composition is approximately the same as that of the target when homogeneous elemental distribution in target and plume is assumed.

Parameters for film fabrication by PLD are type of substrates, growth temperature, type of gases during the fabrication and its partial pressure. Moreover, laser ablation and laser frequency are also controllable parameters which determine the deposition rate and are sometimes important to obtain unstable or metastable phase. For oxide compounds, the oxygen partial pressure during the film fabrication determine the oxygen amount in the films. Therefore, the amount of oxygen vacancies which act as electron donors can be controlled and the conductivity of the films can be tuned.

In this thesis, all $Ti_{1-x}Co_xO_{2-\delta}$ thin films were fabricated by PLD method. A KrF excimer laser PLD (λ = 248 nm, Coherent Inc., COMPexPro50) equipped with vacuum systems provided by PASCAL CO., LTD. was used.

2.2 Reflection High Energy Electron Diffraction (RHEED)

Reflection high-energy electron diffraction (RHEED) is a well-established analytical technique which is very useful for characterizing thin films during film growth as it is usually installed in the deposition chambers of physical vapor deposition systems such as molecular beam epitaxy (MBE) or pulsed laser deposition (PLD). Similar to other methods using electron beam, for example transmission electron microscopy (TEM) and low-energy electron diffraction (LEED), an electron beam is irradiated on a sample and the diffracted pattern of electrons provides crystallographic information.

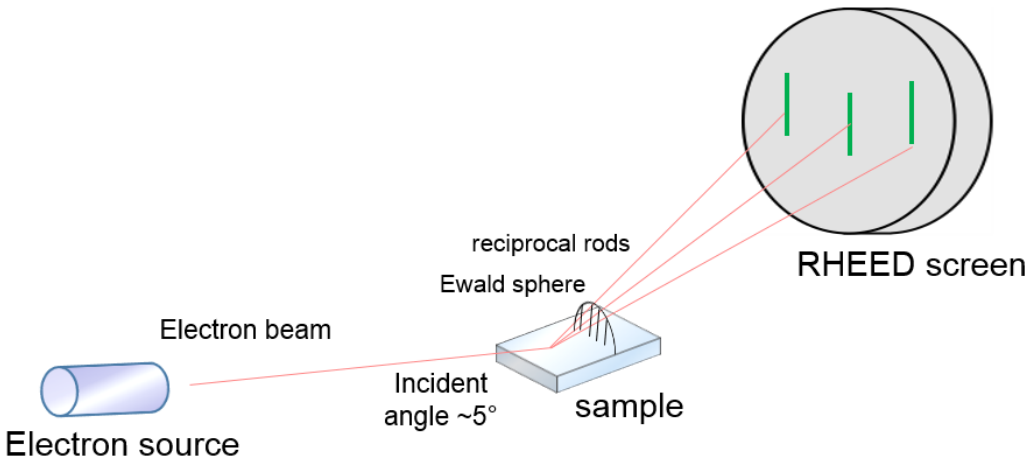

Figure 2.2 Schematic setup of RHEED system.

A RHEED system consists of an electron gun generating electron beam controlled by high voltage, sample stage and photo-luminescent screen (RHEED screen). A typical setup of the measurement is shown in Figure 2.2. The image data on the screen is recorded by an external video camera which is synchronized with the laser pulse. In RHEED observation, the electron beam produced by the electron gun reaches the sample with a small angle to the sample surface. The penetration depth is only several few atomic layers on the surface due to the grazing incident angle. Because RHEED process is surface sensitive, 2D reciprocal lattice (reciprocal rods) which aligns perpendicular to the surface

plane, can be imaged. The diffracted electron beam can constructively interfere resulting in the streak-like or spot-like pattern on the screen. If the sample surface is flat enough, a streak-like pattern (RHEED pattern) which is a series of lines can be observed. Moreover, the distance between adjacent streak lines also gives information of in-plane lattice spacing. RHEED is also commonly utilized to determine the surface reconstruction and growth mode of thin film from its pattern and oscillation behavior.

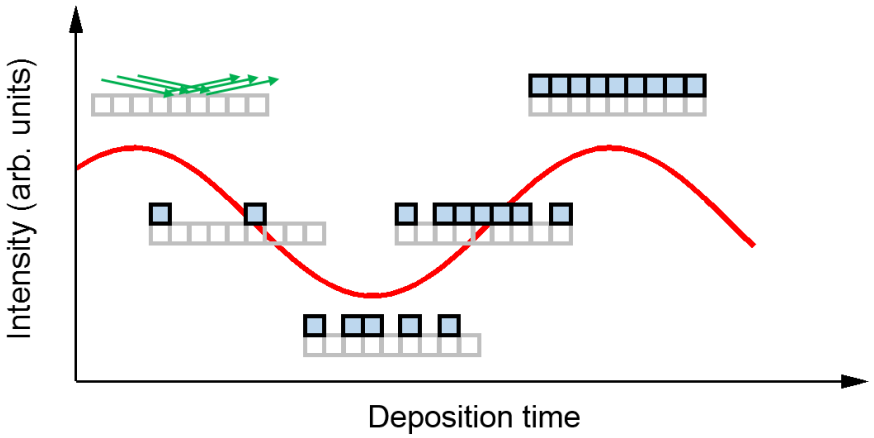

Figure 2.3 Scheme of the origin of RHEED oscillation.

In-situ RHEED measurement provides information about growth mode by analyzing RHEED intensity. Figure 2.3 schematically shows how the RHEED intensity oscillates during the film deposition. When the surface is completely covered with an atomic layer, the RHEED intensity is maximized. Therefore, at the initial stage before film deposition, high intensity is expected because of flat surface of the substrate. When film deposition starts, the RHEED intensity varies depending on the surface conditions and RHEED oscillation can be observed during the film growth. The RHEED oscillation behavior will reflect the film growth modes. Generally, there are three main growth modes: layer-by-layer, step-flow and island growth modes.

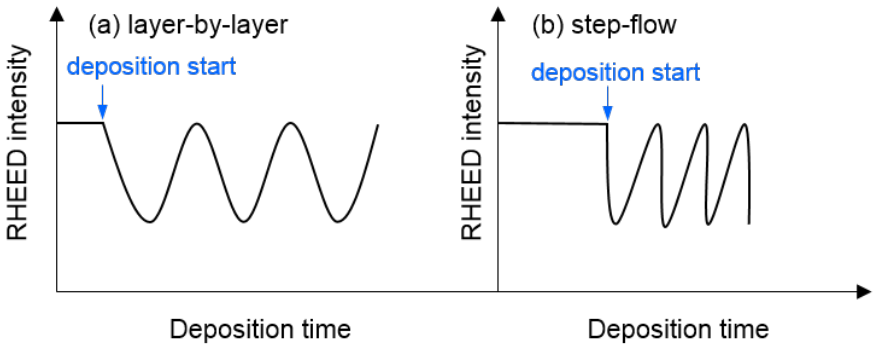

Figure 2.4 RHEED oscillation behavior for (a) layer-by-layer and (b) step-flow mode.

The RHEED oscillation behaviors of layer-by-layer and step-flow modes are simply illustrated in Figure 2.4. For layer-by-layer growth, RHEED intensity of each streak line oscillates periodically with the sinusoidal-like curve. The oscillation period gives information about the height of unit cells, for example, one oscillation may correspond to a half of unit cell or a unit cell. For step-flow growth mode, the RHEED oscillation behavior is similar to that of layer-by-layer growth mode but it exhibits a sharp drop at the end of each period instead of symmetrical shape.

In this experiment, RHEED is used to observed growth mode and surface quality of buffer layer in order to obtain high quality target film on it.

2.3 X-ray Diffraction (XRD) [61]

X-ray Diffraction or XRD is a powerful analytical method which provides information of crystal structure without destroying the sample. XRD measurement is usually done in ambient condition and *ex situ* although *in situ* XRD can be performed with a special setting. Comparing to electron diffraction techniques, XRD shows higher peak resolution and crystal structure can be determined precisely because of their short wavelength in the range of 0.01 to 10 nanometers which is the same level of crystal lattice. The penetration depth of XRD is generally deeper than film thickness, therefore total

film structure and coherent relationship between film and substrate can be investigated.

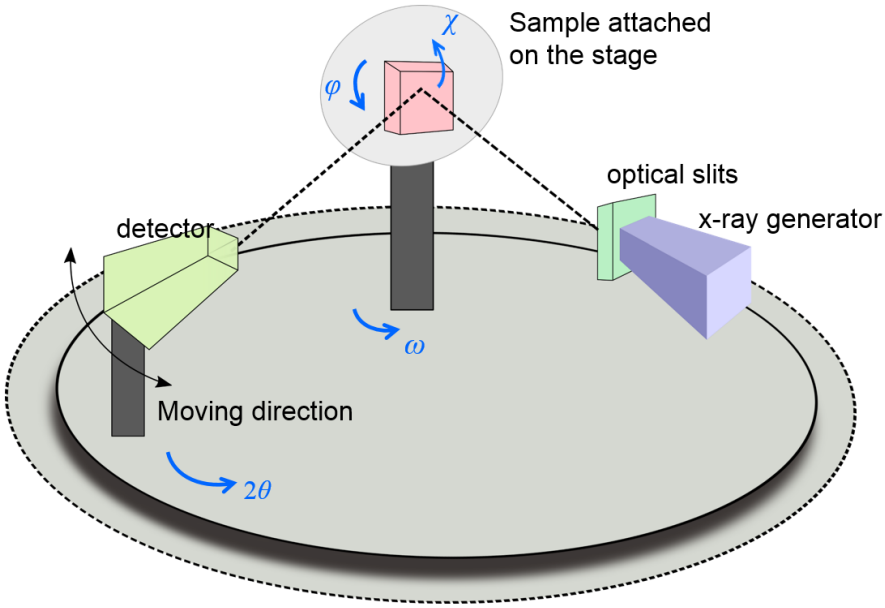

Figure 2.5 Illustration of x-ray diffractometer (XRD).

The scheme of XRD diffractometer is illustrated in Figure 2.5. In XRD system, there are main three parts of x-ray generator tube, sample holder (specimen holder) and detector (counter). For the x-ray generator part, monochromatic x-ray (wavelength, λ = 1.5418 Å) called Cu K_α is generated after passing through optical slits. General process in x-ray generator tube is that a tungsten coil in the tube is heated and the thermally accelerated electrons move toward and impact the copper cathode (target) generating x-ray. The other important part is the detector which can be categorized into three kinds of, 0D, 1D and 2D detectors. By using different kinds of detectors, different resolution and information can be obtained. Higher dimensional detector has larger detection range despite lower resolution. Generally, 2D detector is widely used for survey measurement searching for new phases or new compounds while a fine measurement with higher resolution peak separation usually prefers 1D and 0D detectors.

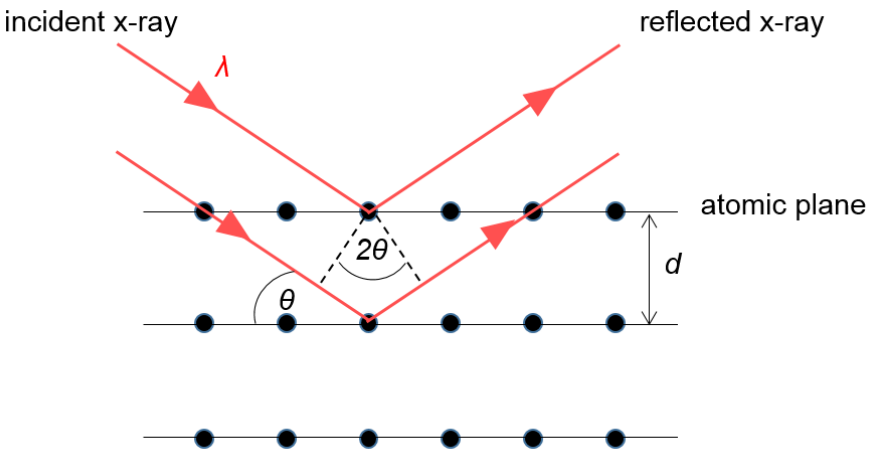

Figure 2.6 Illustration of x-ray diffraction in crystal lattice.

In the principle of XRD measurement, Bragg's law is applied to determine the crystal structure from the angle between the incident beam and the diffracted beam (θ) presented in Figure 2.6 at which constructive interference occurs when

$$2d\sin\theta = n\lambda \tag{2.1}$$

where d, θ, n and λ are the distance between lattice plane, the Bragg angle, an integer and the wavelength of incident x-ray (in this case, λ = 1.5418 Å), respectively. Using the equation, lattice constants of the sample can be obtained from 2θ positions. The crystal lattice in its momentum space (k-space), or reciprocal lattice, can be used to describe XRD diffraction pattern. For a three-dimensional lattice, the reciprocal vectors can be written as:

$$\begin{aligned} \boldsymbol{b_1} &= \frac{\boldsymbol{a_2}\times\boldsymbol{a_3}}{\boldsymbol{a_1}\cdot(\boldsymbol{a_2}\times\boldsymbol{a_3})} \\ \boldsymbol{b_2} &= \frac{\boldsymbol{a_3}\times\boldsymbol{a_1}}{\boldsymbol{a_1}\cdot(\boldsymbol{a_2}\times\boldsymbol{a_3})} \\ \boldsymbol{b_3} &= \frac{\boldsymbol{a_1}\times\boldsymbol{a_2}}{\boldsymbol{a_1}\cdot(\boldsymbol{a_2}\times\boldsymbol{a_3})} \\ \boldsymbol{G} &= h\boldsymbol{b_1} + k\boldsymbol{b_2} + l\boldsymbol{b_3} \end{aligned} \tag{2.2}$$

where $\boldsymbol{b_i}$ and $\boldsymbol{a_i}$ is the primitive vectors of reciprocal and normal lattices, respectively, in

the i-th axis direction, $\boldsymbol{G}$ is the linear combination of these primitive reciprocal vectors, and h, k and l are integers. The diffraction pattern is related to reciprocal vector, $\boldsymbol{G}$, and will always be constructed under the condition of $\boldsymbol{G} = \boldsymbol{\Delta k}$. If one draws an Ewald sphere with a radius of $\boldsymbol{k}$, one can get the diffraction pattern only when the reciprocal lattice points lay on the surface of the Ewald sphere.

For thin film, the epitaxial strain from the substrate can lock the in-plane lattice of the film leading to coherent growth, although out-of-plane lattice of the film might be distorted due to internal pressure in the crystal. There are several scanning modes for XRD, for example, $2\theta - \theta$ scan, rocking curve (ω scan), pole figure, grazing incidence X-ray diffraction (GIXRD), reciprocal space mapping (RSM) etc. Here, three frequently used scanning modes are described as follows.

- $2\theta - \theta$ **Scan:** In this mode, the x-ray source is fixed while the detector and the sample stage are rotated during the measurement. The detector angle represented by 2θ, is always twice of the sample stage angle, θ. The symmetrical diffraction is observed by scanning the crystal plane perpendicular to the scattering plane. The lattice constants and *d-spacing* can be calculated via Bragg's law.

- **Rocking Curve:** By fixing the detector and moving only the sample stage, 2θ is fixed and ω is scanned. In this way, the sample is slightly rocked around the Bragg's peak during the measurement and the lattice perfection or lattice distortion can be examined. The distribution of peak intensity indicates lattice distortion in ω direction. Crystallinity of a film is determined by the full-width of half maximum (FWHM) obtained from Gaussian fit for rocking curve.

- **Reciprocal Space Mapping (RSM):** To obtain RSM, 2θ-ω scans with several ω are performed and cross section in reciprocal space is obtained. The data are usually shown as a map on q_x - q_z plane, where q_x and q_z denote the inverse values of

in-plane and out-of-plane lattice constants, respectively. By using RSM information, the coherent growth of thin film can be examined; the lock of in-plane lattice constant of the film with the substrate implies the coherent growth.

In this experiment, $2\theta - \theta$ scaning mode is mainly used and XRD measurements were performed by the D8 Discover XRD system (Bruker AXS) with a 1D linear detector (VANTEC-1).

2.4 Electrical Measurement

In electrical measurement, a simple two-probe measurement usually suffers from the resistances of wires, electrodes and interfaces resulting in low accuracy especially for samples with low resistivity. Therefore, a standard four-point probe configuration is more common since such parasitic resistances can be ignore. When current (I) is applied to a sample voltage (V) in the same direction is generated and the relationship of I and V follows Ohm's law, $V = I \cdot R$, where R is the electrical resistant of the sample.

In this experiment, films with Hall bar pattern are usually used for in-plane transport measurements. Figure 2.7 shows a layout of Hall bar patterned film and arrangement of eight electrodes. I^- and I^+ are used for applying electrical current while V_2, V_3 and V_4 are used for voltage measurement of channel 2, 3 and 4, respectively. The measurement is performed by using the resistance bridge of Physical Properties Measurement System (PPMS, Quantum Design Co.). In PPMS, temperature dependence of transport properties can be obtained under an external magnetic field. The operated ranges of temperature and magnetic field are 2 K to 380 K and $\pm$9T, respectively.

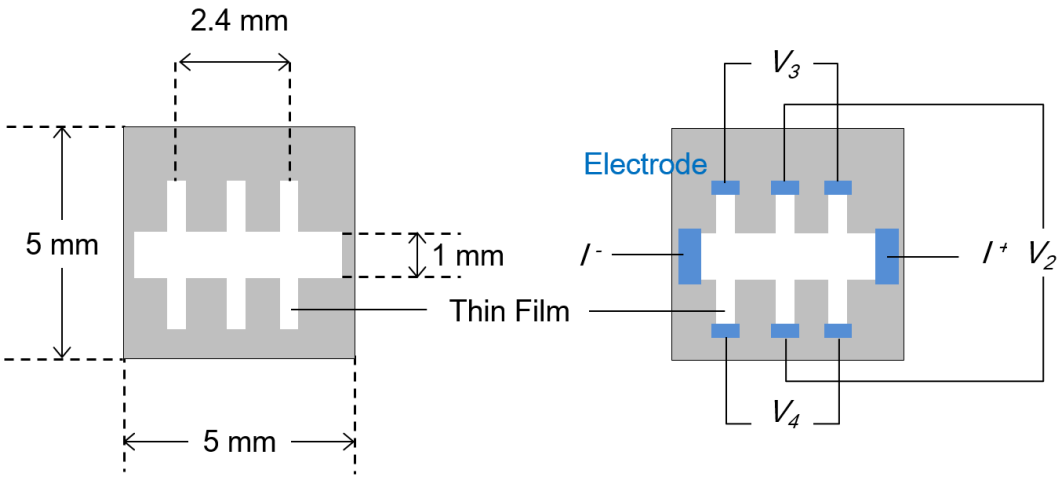

Figure 2.7 Layout of Hall bar patterned film and electrical circuit for 4-probe measurement and Hall effect

2.4.1 Electrical resistivity

The data obtained from PPMS is a set of current, voltage and resistance. Without external magnetic field, V_3 and V_4 electrodes are used for voltage detection and electrical resistivity, ρ, is simply calculated from the average of measured resistance (R) of channel 3 and channel 4 by using the following equation.

$$\rho = \frac{R \times A}{l} \tag{2.3}$$

$$\rho = \frac{R \times w \times t}{l} \tag{2.4}$$

A and l denote the cross-sectional area and the length of current path, respectively. Because A can be obtained from the product of w, width of current path, and t, thickness of the film, Equation (2.3) can transform to Equation (2.4). From electrical resistivity, one may calculate electrical conductivity (σ) by using the relation, $\sigma = 1/\rho$

2.4.2 Hall Effect

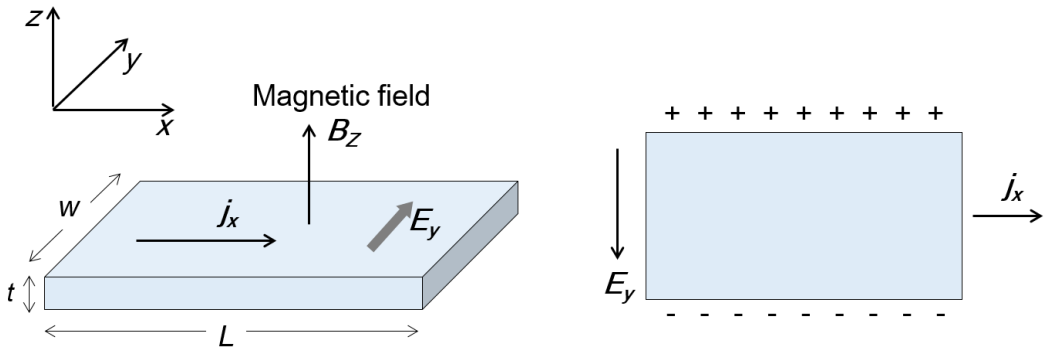

Figure 2.8 The standard geometry for Hall effect with rod-shape specimen of rectangular cross-section placed in a magnetic field, B_z

Hall measurement [61] is a useful method to investigate the carrier density and mobility in semiconductor. Figure 2.8 shows a standard geometry for Hall effect measurements. When a magnetic field is applied in z-direction (B_z), an electric field is developed across a specimen due to the Lorentz force, so called Hall field E_y. Direction of the Hall field is determined by $\mathbf{j} \times \mathbf{B}$, where $\mathbf{j}$ is the current flowing across the magnetic field. From charge balance along y direction a relation between electric field and magnetic field can be written as

$$E_y = \frac{j_x B_z}{nq} \tag{2.5}$$

where j_x, n and q denote the current density in x direction, the carrier density and the carrier charge, respectively. Hall coefficient, R_H, and Hall Resistance, R_{xy}, are defined as,

$$R_H = \frac{E_y}{j_x B_z} \tag{2.6}$$

$$R_{xy} = \frac{V_y}{I_x}. \tag{2.7}$$

By using the relationship $E_y = \frac{Vy}{w}$ and $j_x = \frac{I_x}{w \cdot t}$, the following equation is derived.

$$R_H = \frac{R_{xy} \cdot t}{B_z} \tag{2.8}$$

Therefore, the slope of a plot between R_{xy} vs. B_z will represent R_H/t from which carrier density can be calculated. The sign of the slope also represents the type of carrier: hole (positive slope) and electron (negative slope). Once the carrier density is obtained, mobility can be calculated. If the charge carrier is electron then $q = e$ and we get the formula for carrier density (n) and mobility (μ) as follow:

$$R_H = -\frac{1}{ne} \tag{2.9}$$

$$\mu = \frac{R_H}{\rho} \tag{2.10}$$

Moreover, the mobility is sometimes written as a function of carrier density and resistivity, $\mu = \frac{1}{ne\rho}$.

For ferromagnetic materials, an additional magnetic field from its magnetization could also contribute to the ordinary Hall effect and this is known as "anomalous Hall effect". Therefore, the hyteresis can also be observed in the measurement.

In this experiment, a set of R_{xy} measured under applied magnetic field is obtained at 300 K from voltage measurement of channel 2 (V_2) represented in Figure 2.7. Carrier density and mobility of the films were evaluated at 300 K.

2.5 Magnetization Measursement

SQUID magnetometer which abbreviated from superconducting quantum interference device magnetometer is a powerful method to measure magnetic properties because of high sensitivity to magnetic moment or magnetization. In this method, overall magnetic moment of a sample was evaluated yielding macroscopic magnetic properties.

The SQUID [62] is a ring composed of two parallel Josephson junctions, each of which is formed by separating two superconductors with a thin insulating layer (Figure 2.9). When steady bias current is maintained, the output voltage oscillates with the

change in phase differences influenced by the magnetic flux through the ring. By detecting the change in oscillations, the change of magnetic flux can be evaluated and the magnetic moment of the sample is determined. Because SQUID requires operation at low-temperature, the measurement system is usually equipped with cryogenic baths of liquid helium and liquid nitrogen working as cooling and temperature controlling system.

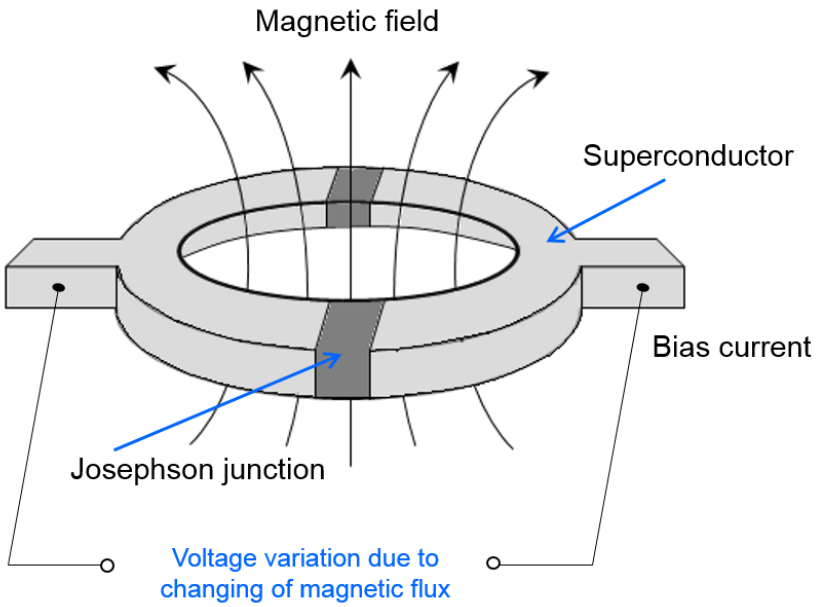

Figure 2.9 SQUID consists of insulating layers between two superconductors detecting the change change in oscillations influenced by magnetic flux.

The measurement system is called magnetic property measurement system (MPMS) which has a SQUID ring inside the He bath. MPMS consists of SQUID antenna (signal-to-flux converter), SQUID transducer (magnetic flux-to-voltage converter) and analyzer. The data is provided as total magnetic moment and can be further converted to magnetization by considering the volume of the sample. Scheme of MPMS is illustrated in Figure 2.10. During the measurement, the sample rod which is made of drinking straw, will move up and down and produce an alternating magnetic flux in pick-up coil region. The signal is transferred to the SQUID device and subsequently to the analyzer.

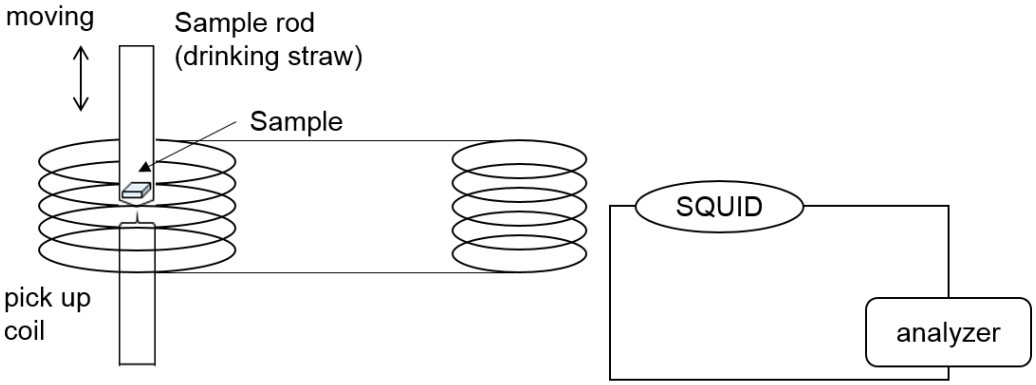

Figure 2.10 Scheme of magnetic property measurement system (MPMS) containing pick up coil region, SQUID device and analyzer.

The sample rod can be prepared from drinking straw. First, the straw is notched at the center in order to hold the sample on this position. Then, a sample is introduced into the straw. The sample can be oriented differently as shown in Figure 2.11 for out-of-plane or in-plane magnetization measurement.

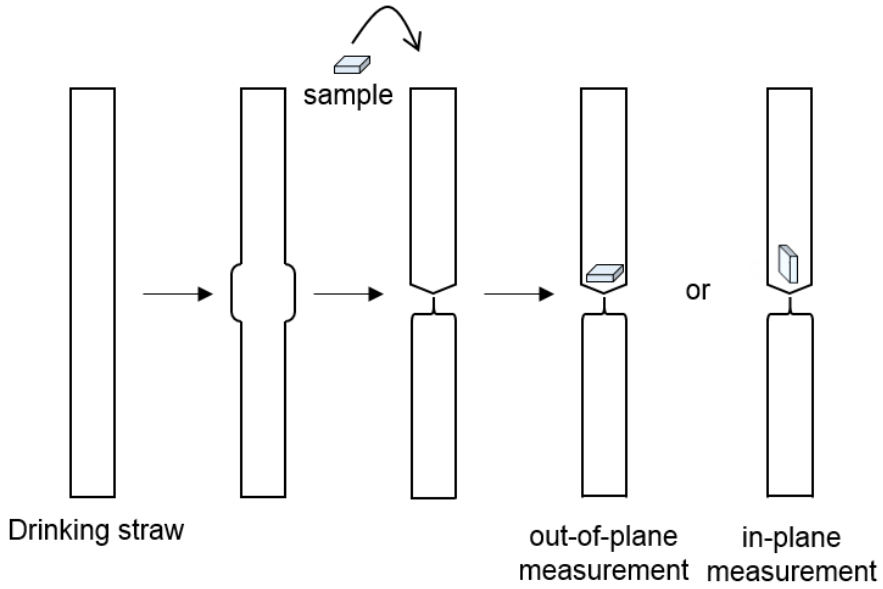

Figure 2.11 Preparation of sample rod by putting a sample at the middle of drinking straw with different orientation of the sample for out-of-plane or in-plane measurement.

In this experiment, MPMS, Quantum Design, is used for the measurement in which temperature and magnetic field can be varied in the range of 2 K to 380 K and ±9T,

respectively. The sensitivity of the system is in an order of 10^{-8} emu.

2.6 Magnetic Force Microscope (MFM) [63,64]

There are several techniques for magnetic domain observation such as bitter methods, magneto-optical method by Kerr microscopy, scanning SQUID (Superconducting Quantum Interference Device) microscopy. Among them, magnetic force microscopy (MFM) which is non-destruction method, has good sensitivity to small variations in magnetization and also low sample preparation requirements. In addition, surface topographic image and magnetic image are obtained simultaneously with dual scanning which enable to distinguish magnetic signal from topographic information. MFM has high-spatial resolution in the order of ten nanometers although the recording time is quite long comparing to other methods.

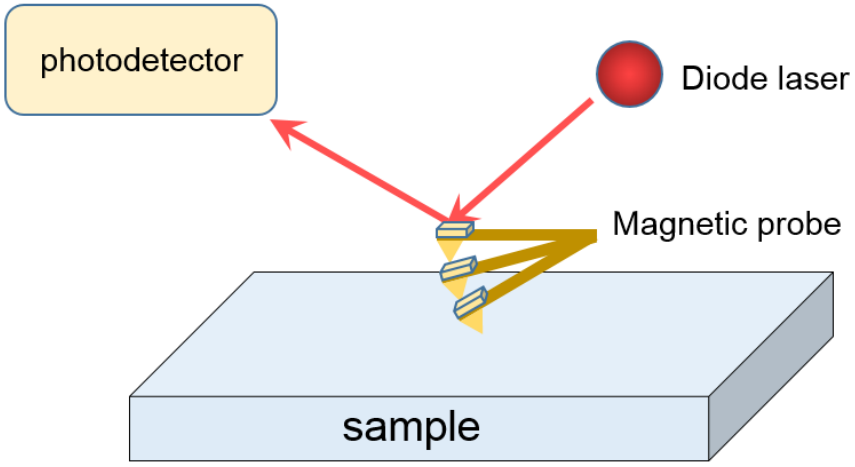

Figure 2.12 Illustration of first scan in MFM measurement: a laser beam focused at the end of cantilever is reflected and detected by the detector leading to topographic image.

MFM can be considered as a variant of scanning force microscopy. By equipping a ferromagnetic tip to the scanning force microscope, MFM is able to detect magnetostatic force between a sample and the tip. MFM system is composed of a cantilever and a magnetic tip and photodetector. In the measurement, a successive two scan is performed.

The principle of the first scan which measures the surface profile with the repulsive mode operation is same as that of atomic force microscopy (AFM) (Figure 2.12). A laser beam which is focused at the end of a tip on the cantilever is reflected and detected by the photodetector while the cantilever moves up and down due to the different atomic force. The second scan is performed with a lift height as illustrated in Figure 2.13. In the second scan, the cantilever is excited at the resonant frequency ω_0 with a certain amplitude δ. When the cantilever detects magnetic stray field from the sample, a phase shift of cantilever oscillation is exerted. By analyzing this phase shift information, magnetic image is obtained.

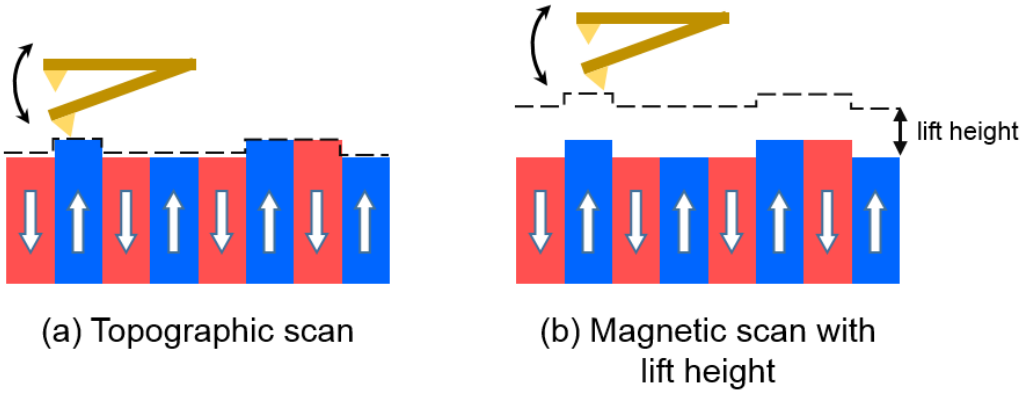

Figure 2.13 A scheme of successive two scans with (a) topographic scan and (b) magnetic scan with lift height.

The resonant frequency of the cantilever relates to its spring constant k, and its effective mass m as follows.

$$\omega_0 = \sqrt{\frac{k}{m}} \tag{2.11}$$

When phase shift occurs due to magnetostatic force, it results in frequency ω with

a modified spring constant k',

$$\omega = \sqrt{\frac{k'}{m}} \tag{2.12}$$

$$k' = k - \frac{\partial F}{\partial z} \tag{2.13}$$

where F and z are the force and the distance between the cantilever and the sample, respectively. When an attractive interaction is detected, $\frac{\partial F}{\partial z} > 0$, the cantilever spring will be soften. On the contrary, a repulsive interaction, $\frac{\partial F}{\partial z} < 0$, will stiffen the spring constant. The cantilever's resonant frequency is modified by this change of spring constant resulting in,

$$\omega = \omega_0 \sqrt{1 - \frac{1}{k}\frac{\partial F}{\partial z}} \tag{2.14}$$

The difference or shift in resonant frequency $\Delta\omega$ is defined as $\omega - \omega_0$ and can be simply approximated when $\frac{\partial F}{\partial z} \ll c$ as,

$$\Delta\omega \approx -\frac{1}{2k}\frac{\partial F}{\partial z}. \tag{2.15}$$

A shift in the resonant frequency results in a change of both oscillation amplitude and phase shift. Phase shift is given by

$$\Delta\phi \approx -\frac{Q}{k}\frac{\partial F}{\partial z}. \tag{2.16}$$

Therefore, the sensitivity of the measurement is dependent on the Q factor which represents the influence of environment medium during the measurement. Q factor is defined as a ratio between resonant frequency and a shift in resonant frequency, $Q = \frac{\omega_0}{\Delta\omega}$ (Figure 2.14).

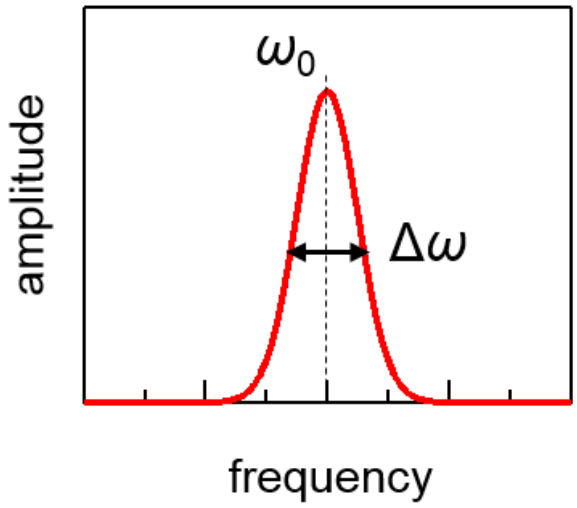

Figure 2.14 Definitions of resonant frequency ω_0 and a shift in resonant frequency $\Delta\omega$ of a cantilever using for MFM measurement.

Generally, Q might range from several hundreds in liquids or ambient air to more than 100,000 in ultra high vacuum (UHV). High Q indicates high sensitivity and can be increased by decreasing air viscosity. Therefore, high sensitive measurement is expected in vacuum chamber [65]. In this thesis, a rotary pump was used to evacuate the chamber pressure down to 10 Pa.

2.7 Thickness Measurement

In this experiment, film thickness was measured by Dektak-6M Stylus Profiler of ULVAC. Films with Hall bar pattern (Figure 2.15) which is suitable for film thickness and electrical transport measurements, can be obtained by covering areas of substrate during film deposition with a Hall bar mask. The principle of thickness measurement is rather simple. First, a sample is set on the movable sample stage. Over the sample, there is a probe with needle-like shape. When the measurement begins, the stage will move along a scanning direction and the probe responses to the difference in height between film and bare substrate. During the measurement, the needle moves from bare substrate

across the film to another bare substrate area and then film thickness is obtained as a result of the upward and downward motion of the probe.

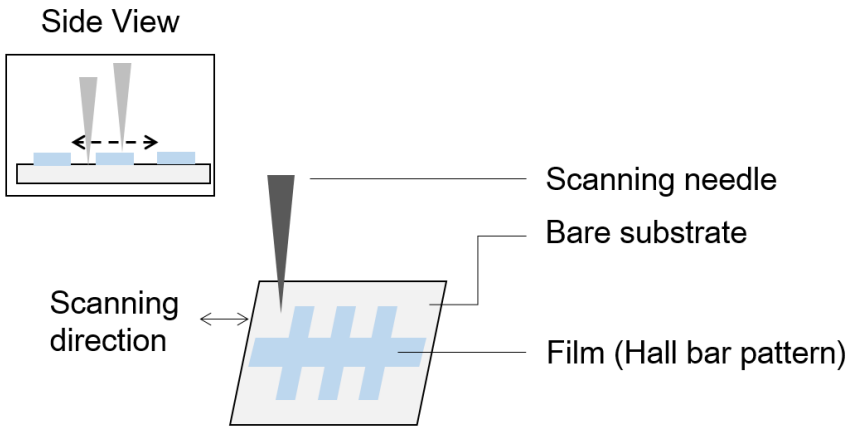

Figure 2.15 Illustration of a film with Hall bar pattern and thickness measurement

2.8 Density functional theory (DFT) [66]

Density functional theory (DFT) bases on electron density where two fundamental theorems by Kohn and Hohenberg, and set of equations by Kohn and Sham are applied. One of Kohn and Hohenberg theorems is that the ground state energy is a unique functional of electron density and E[n(r)] can be used to express the ground state energy E where n(r) denotes the electron density. Another theorem states that true electron density is responsible for the minimized energy of overall functional which is corresponding to the full solution of the Schrödinger's equation. Practically, in the calculation procedure, one can vary the electron density until minimized energy is obtained from the functional. According to Kohn and Hohenberg theorem, the energy functional can be written as

$$E[\Psi_i] = E_{known}[\Psi_i] + E_{XC}[\Psi_i]. \tag{2.17}$$

Here, the energy functional is split into two simple terms of known term $E_{known}[\Psi_i]$ and everything else $E_{XC}[\Psi_i]$. In the known term, electron kinetic energy, Coulumbic interaction between electrons and nuclei, pairs of electrons and pairs of nuclei are included. For

the term, $E_{XC}[\Psi_i]$, it will include all quantum mechanical effects and is defined as "exchange correlation function". This exchange correlation function is important to solve the Kohn-Sham equation at which a single-electron wave function is considered. By using different approximation, the exchange correlation function is varied. For example, when a uniform electron gas is considered with a constant electron density, the approximation will be called *Local density approximation (LDA)* and when spin density is added, it will be modified to *Local spin density approximation (LSDA)*. The higher approximation level is achieved when the electron density and the first-order electron correlation correction is applied, so called *Generalized gradient approximation (GGA)*. There are many kinds of GGA functional and most widely used are the Perdew-Wang functional (PW91) and the Perdew-Burke-Ernzerhof functional (PBE).

In this thesis, structure optimization of proposed substructure for anatase (Ti,Co)O_2 is performed by using Vienna *Ab initio* simulation package (VASP) with PBE function.

Chapter 3

Titania Buffer Layer *

Buffering technique is one of the most useful for epitaxial film growth with low lattice mismatch. In addition, it was also used in order to decrease crystallized temperature leading to less possibility of segregation when doping is applied. This is suitable for obtaining high quality films with no clustering [16,67,68]. In this chapter, the details of fabrication of anatase TiO_2 buffer will be described. In addition, the advantages of buffering technique will be briefly summarized.

Among perovskite substrates, perovskite $LaAlO_3$ (LAO) substrate (*pseudocubic*, a = 0.379 nm) has the small lattice mismatch ($\sim$0.2%) with anatase structure. Lattice constants of anatase TiO_2 are a = 0.3785 nm and c = 0.9514 nm. The growth temperature is optimized by using *in situ* RHEED information and the surface morphology. The thickness of buffer layer is about 5 nm which cannot be directly characterized by XRD since it is too thin. However, indirect evidence that buffer layer is c-axis oriented film can be obtained from XRD by increasing film thickness to 40 nm without any other treatments, defined as non-buffered film.

In this experiment, LAO step substrate was purchased from Shinkosha Co. Ltd. and before the fabrication of thin film, LAO substrate were pre-annealed at 600 °C under vacuum at base pressure for 10 minutes as the surface cleaning process. Titania (TiO_2) buffer films were grown by using rutile single crystal substrate from Shinkosha Co. Ltd. as the

---

*This chapter contains the partial contents of the following publication.

1) T. S. Krasienapibal, T. Fukumura, Y. Hirose, and T. Hasegawa, Jpn. J. Appl. Phys. **53**, 090305 (2014). Copyright 2014 The Japan Society of Applied Physics.

target. Titania buffer layer was fabricated under oxygen atmosphere. The oxygen partial pressure, P_{O_2} was fixed at high pressure of 10^{-4} Torr because the insulating anatase TiO_2 without any oxygen vacancies is preferable for this buffer layer. With less oxygen vacancies defect, high crystallinity film is expected, and also the insulating buffer will not contribute to transport properties of the film grown on it. The growth temperature range, T_G were varied from 500 to 800 °C. The laser power for the ablation is averagely constant at 1.5 J/cm^2 with laser spot size of 0.33 mm^2. All titania buffer films were post-annealed at T_{anneal} 800 °C and P_{O_2} 10^{-3} Torr in order to make flat surface. Then, the buffer film is cooled down to room temperature under the same P_{O_2}. After that, the upper layer of target film will be fabricated on it.

3.1 *In situ* RHEED Observation

The titania buffer layers were fabricated by 5 Hz repetition of laser pulse. The RHEED pattern of LAO substrate and fabricated titania buffer layer at growth temperature of 700 °C ($T_G = 700$ °C) were shown in Figure 3.1. For LAO substrate, spot-like patterns were observed and after pre-annealing under high vacuum, LAO substrate showed clearer spot patterns with relatively smaller spot size. After the starting of the deposition, the spot-like patterns slowly disappeared and changed to the new streak-like pattern of titania buffer layer. The Kikuchi line can be slightly observed after post annealing of buffer film.

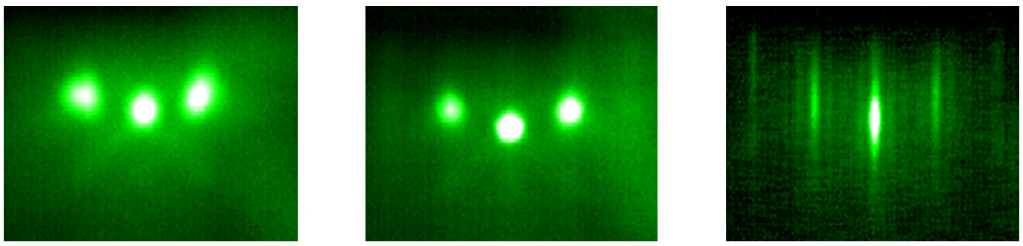

(a) As received LAO substrate (b) Pre-annealed LAO substrate (c) Titania buffer layer

Figure 3.1 RHEED pattern of LAO substrate before and after pre-annealing and titania buffer layer on LAO substrate.

The RHEED oscillations were obtained continuously from few seconds after the starting point until the end of buffer fabrication as presented in Figure 3.2. From the film thickness of ~ 5 nm measured by Dektak, I can estimate one period of the oscillation as half of a unit cell of anatase titanium dioxide. The oscillation pattern confirmed the layer-by-layer growth of anatase TiO_2 buffer layer.

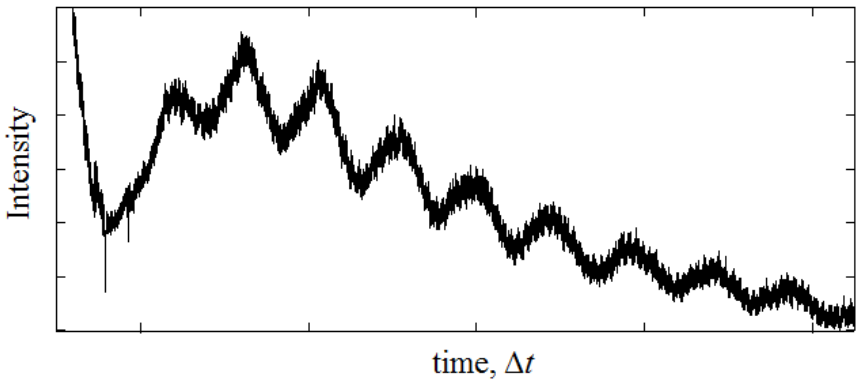

Figure 3.2 RHEED intensity versus time plot illustrating clear RHEED oscillations during the fabrication of TiO_2 buffer layer.

3.2 Surface Morphology

The surface morphology of titania buffer layers were examined by AFM measurement. AFM images of titania buffer layers prepared at different growth temperature were shown in Figure 3.3. As shown in Figure 3.3, The step and terrace can be observed in all

samples with slightly different roughness.

There is no significant difference in the AFM images between 600 °C and 700 °C. The root-mean-square roughness (RMS) of T_G = 600 and 700 °C are 0.17 and 0.15 nm (area = 2×2 μm^2), respectively. The RHEED and AFM results show high quality of titania thin film with very flat surface when T_G is 700 °C, therefore the optimal buffer layer can be fabricated at T_G = 700 °C, P_{O_2} = 10^{-4} Torr with post annealing at T_{anneal} = 800 °C, P_{O_2} = 10^{-3} Torr.

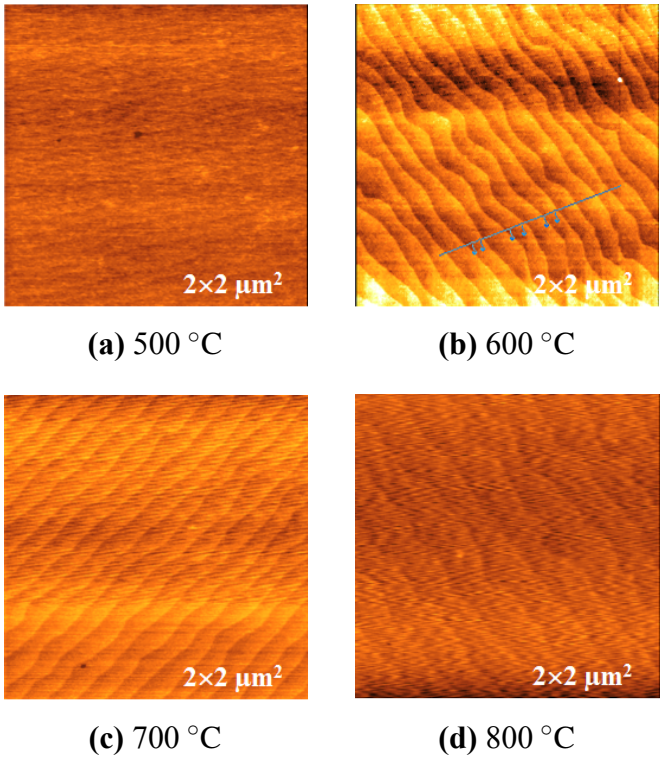

(a) 500 °C **(b)** 600 °C

(c) 700 °C **(d)** 800 °C

Figure 3.3 AFM images of titania buffer at T_G = 500 - 800 °C.

In summary, the optimized condition of the titania buffer layer is growth temperature at 700 °C with post-annealing at 800 °C.

3.3 XRD measurement

As mentioned previously, the thickness of buffer layer film is only about 5 nm which gives very low intensity of XRD pattern. As a consequence, the XRD measurement to characterize anatase TiO_2 or confirm the epitaxial growth becomes difficult. Nevertheless, the thicker film without buffer layer, defined as *non-buffered film*, can be used to examine the crystal structure of the tiatania buffer layer. For the 40-nm thick film obtained by longer deposition time without any treatment after the film fabrication, XRD measurements were performed, as presented in Figure 3.5. The XRD pattern of non-buffered film fabricated at 700 °C and $P_{O_2} = 10^{-4}$ Torr shows only anatase TiO_2 phase with *c*-axis orientation. This result can be an indirect evidence that the buffer film, also grown at the same condition, is an epitaxial film of anatase TiO_2.

3.4 Advantages of titania buffer layer

In order to investigate the advantages of the titania buffer layer, anatase TiO_2 epitaxial films were fabricated on this titania buffer layer (self-buffered film), and film quality and transport proterty were examined. Two film structures of non-buffered and self-buffered are compared in Figure 3.4.

(a) Non-buffered film **(b)** Self-buffered film

Figure 3.4 Scheme of non-buffered and self-buffered film.

The XRD patterns of self-buffered film fabricated at 250 °C and non-buffered film fabricated at 700 °C, under $P_{O_2} = 10^{-4}$ Torr, are compared in Figure 3.5. The result suggests that epitaxial growth of anatase TiO_2 thin films can be achieved at low temperature

of 250 °C by using the buffer layer. It is noted that without buffering, anatase epitaxial thin film cannot be grown at such a low temperature. Accordingly, with this mild condition, the film shows flat morphology with small surface roughness.

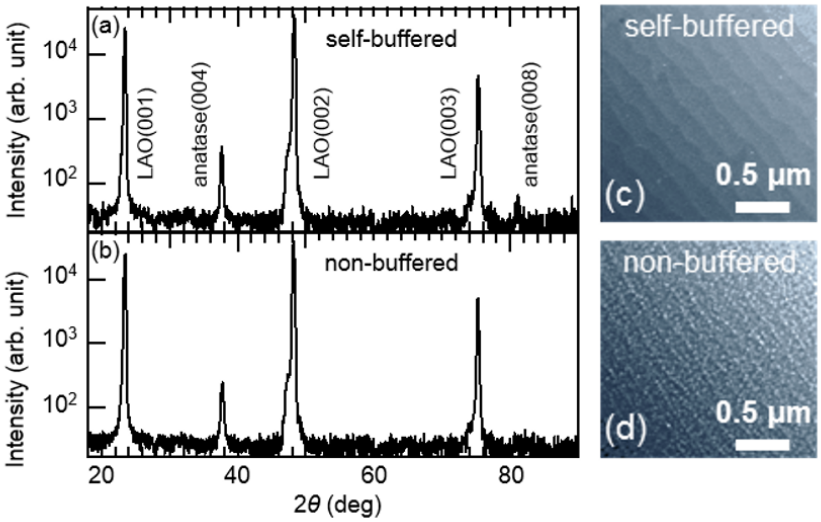

Figure 3.5 XRD patterns of (a) self-buffered film fabricated at 250 °C and (b) non-buffered film fabricated at 700 °C, under P_{O_2} 10^{-4} Torr. (c) and (d) show corresponding surface morphology of the films [69].

The crystallinity of self-buffered and non-buffered film is evluated by rocking curves mode of XRD measurement (Figure 3.6). The full width at half maximun (FWHM) values of the self-buffered and non-buffered film are 0.09 ° and 0.11 ° respectively. The smaller value of FWHM of self-buffered film indicated that self-buffered film shows higher crystallinity than that of conventional non-buffered film. Therefore, high quality film from both aspects of crystallinity and surface morphology is obtained by utilizing the buffering technique.

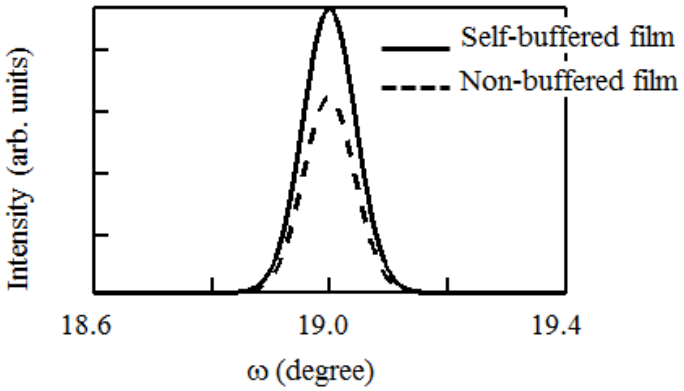

Figure 3.6 Rocking curves of self-buffered film (line) and non-buffered film (dot line).

The temperature dependence of resistivity were compared between self-buffered and non-buffered films (Figure 3.7). Both films were fabricated at $P_{O_2} = 10^{-5}$ Torr. The T_G values of self-buffered and non-buffered film were 250 and 700 °C, respectively. The carrier density of both films was about $\sim 3.5 \times 10^{19}$ cm^{-3}. The self-buffered film exhibited lower resistivity or higher conductivity than non-buffered film over the temperature range indicating the higher mobility for self-buffer film.

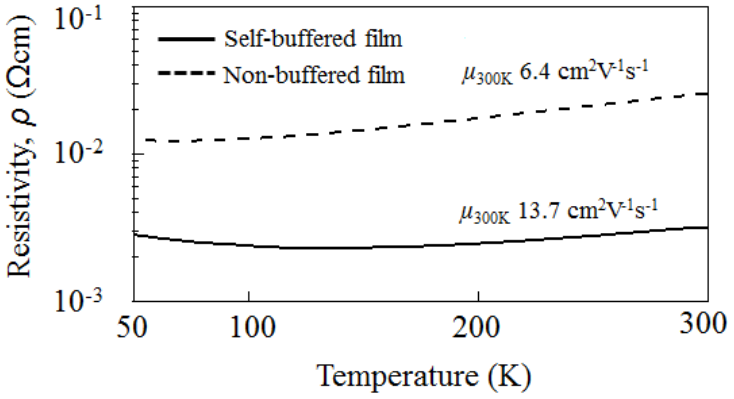

Figure 3.7 Temperature dependence of resistivity compared between self-buffered and non-buffered film.

The temperature dependence of Hall mobility is illustrated in Figure 3.8, it is obvious that the mobility of self-buffered film was enhanced and became higher than that of non-buffered film over the measured temperature range. The decreased mobility at low

temperature probably derives from the carrier scattering by a small amount of neutral impurities, grain boundaries and phonons.

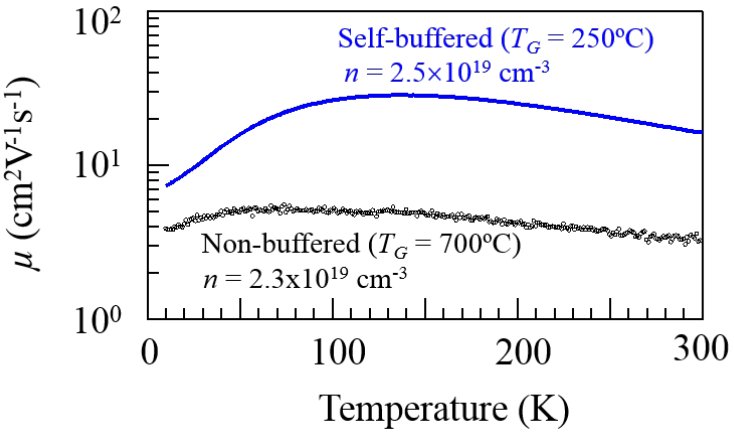

Figure 3.8 Temperature dependence of Hall mobility compared between self-buffered and non-buffered film.

In summary, the buffering technique has the advantages that (1) epitaxial growth can be performed at low temperature (2) surface morphology and film quality are high due to mild condition (low growth temperature) and (3) improved transport properties. These indicate high quality TiO_2 films can be obtained by applying the buffering technique.

Chapter 4

Observation of magnetic domain structure in anatase (Ti,Co)O_2 at room temperature *

In this chapter, the observation of magnetic domain structure in anatase (Ti,Co)O_2 films at room temperature will be discussed. The magnetic domain structures were investigated as functions of carrier density (n) and Co content (x) by means of magnetic force microscopy (MFM) measurement in vacuum. By using stereological method, the average magnetic domain size was estimated and micromagnetic parameters of magnetic anisotropy (K_u), domain wall energy (σ_w) and stiffness constant (A) were evaluated. The relation between microscopic and macroscopic magnetism of anatase (Ti,Co)O_2 epitaxial films at room temperature was studied.

4.1 Introduction

Microscopic study of magnetic domain structure in ferromagnetic material is an important issue from both aspects of fundamental materials science and device applications. Relationship between bulk magnetization and microscopic magnetic domain structure is a key to understanding the underlying science and utilizing the material appropriately. In

---

*A part of this chapter including Figure 4.4, Figure 4.7, Figure 4.8 and Figure 4.13 has been published in *Applied Physic Letters.* Reprinted with permission from "Observation of magnetic domain structure in anatase (Ti,Co)O_2 thin film at room temperature", Thantip S. Krasienapibal, Shun Inoue, Tomoteru Fukumura, and Tetsuya Hasegawa, *Appl. Phys. Lett.,* **2015, 106,** 202402. Copyright 2015 AIP publishing LLC.

case of (Ga,Mn)As, a representative ferromagnetic semiconductor, a conventional stripe domain structure was observed and found to be related with its the macroscopic magnetic property [18]. One promising application concerning magnetic domain structure is magnetic domain wall propagation controlled by current. The current-induced magnetization reversal has attracted much interest as an alternative magnetic memory encoding method. Recently, it was demonstrated by using (Ga,Mn)As thin film despite its low ferromagnetic Curie temperature [21]. The observed current threshold was 2–3 orders of magnitude lower than those of ferromagnetic metals indicating the possibility of lower energy consumption devices. Therefore, the microscopic study of $(Ti,Co)_2$, a high T_C ferromagnetic semiconductor, is important from a viewpoint of practical application.

Although several magnetic domain observations in magnetically doped TiO_2 films were performed previously by magnetic force microscope (MFM) at room temperature, there is an undesirable contribution from the surface topography of the films. Therefore, smooth films is preferable for MFM measurement in order to obtain a magnetic image without any contamination of topological information which sometimes misleads us the interpretation of magnetic domain structure.

Furthermore, small remanant magnetization in $(Ti,Co)O_2$, a nature of diluted system, requires highly sensitive measurement in order to obtain the real magnetic domain structure. The high sensitivity measurement may be achieved by using vacuum atmosphere during the MFM measurement.

4.2 Experimental details

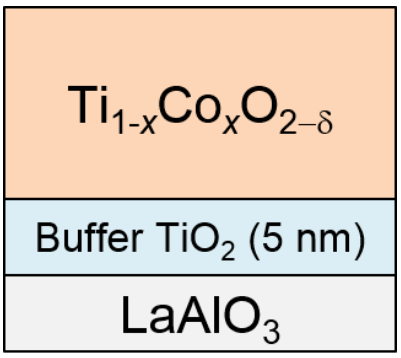

Figure 4.1 Schematic image of film structure with insulating TiO_2 buffer layer.

Anatase $Ti_{1-x}Co_xO_{2-\delta}$ (001) thin films were epitaxially grown on $LaAlO_3$ (001) step substrates (*pseudocubic*, a = 0.379 nm) buffered with 5 insulating TiO_2 unit cells by pulsed laser deposition (PLD) with KrF excimer laser. The laser energy density and laser repetition were 1.5 J/cm^2 and 5 Hz, respectively. The structure of the film is illustrated in Figure 4.1. The buffer layer of TiO_2 was grown at 700 °C in oxygen pressure (P_{O_2}) of 10^{-4} Torr, followed by in-situ post-annealing at 800 °C for 10 minutes, and then was cooled down to room temperature. Anatase $Ti_{1-x}Co_xO_{2-\delta}$ thin films were grown on this buffer layer at 250 °C in different P_{O_2} ranged from 10^{-6} to 10^{-4} Torr to control the carrier density, since the oxygen vacancy served as an electron dopant. The crystal structure of the films were characterized by x-ray diffraction (XRD). The typical film thickness was 45 nm measured by stylus profilometer. The electrical properties were evaluated by four-probe and Hall effect measurements of Hall bar patterned samples. The magnetization was measured by a SQUID magnetometer. The topographic and magnetic images were observed by MFM at room temperature in air and vacuum of 10 Pa without external magnetic field. An MFM tip coated with 35 nm radius of CoPtCr alloy was used. In the MFM measurements, topographic imaging was performed with contact mode followed by magnetic imaging with constant lift height between MFM tip and film surface for

eliminating topographic contribution to the magnetic image.

4.3 Results and Discussions

4.3.1 Characterization and surface morphology of films

The films were confirmed to be epitaxially grown with pure anatase phase by x-ray diffraction. The XRD diffraction patterns of the film with different x fabricated at P_{O_2} = 10^{-4} Torr are shown in Figure 4.2. All films showed anatase (004) peak around 37.9°. A small peak of anatase (008) around 81° was not clearly seen. From the anatase (004) peak, the c-axis lattice constants of $Ti_{1-x}Co_xO_{2-\delta}$ films were evaluated as 0.947 nm, 0.949 nm, 0.947 nm and 0.952 nm for x = 0.01, 0.03, 0.05 and 0.10, respectively. The c-axis lattice constants are close to or slightly smaller than that of bulk anatase TiO_2 (0.9514 nm). The anatase (004) peak was strong and sharp for smaller x while peak broadening was seen in the sample with higher x suggesting that Co was doped into anatase structure.

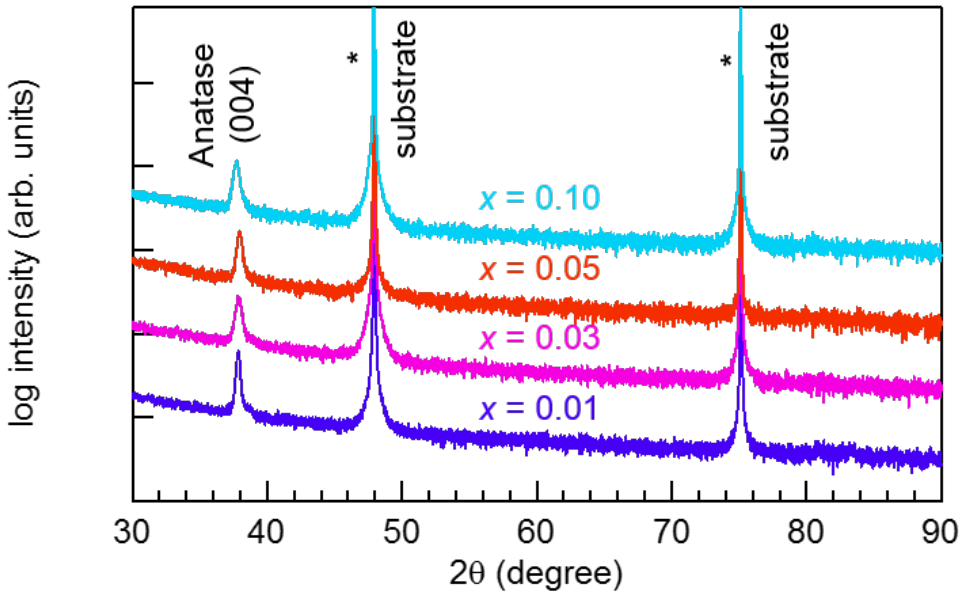

Figure 4.2 X-ray diffraction pattern of anatase $Ti_{1-x}Co_xO_{2-\delta}$ films with x = 0.01, 0.03, 0.05 and 0.10, fabricated on TiO_2 buffer layer at P_{O_2} = 10^{-4} Torr.

Surface morphology of the anatase $Ti_{1-x}Co_xO_{2-\delta}$ films were obtained from the first

scan by the MFM measurement. Despite the different Co contents and oxygen pressure during the films deposition, the films show typical surface roughness of root-mean-square (RMS) roughness less than 0.3 nm in an area of $2 \times 1\ \mu m^2$. The surface morphology of anatase $Ti_{1-x}Co_xO_{2-\delta}$ films with $x = 0.01$, 0.03, 0.05 and 0.10, is presented in Figure 4.3. No trace of Co segregation on the film surface was detected.

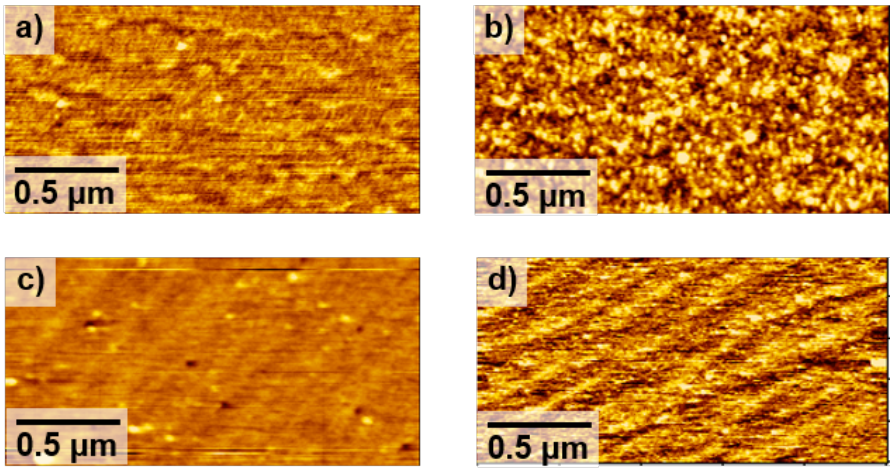

Figure 4.3 Surface morphology of anatase $Ti_{1-x}Co_xO_{2-\delta}$ films with x = 0.01, 0.03, 0.05 and 0.10, fabricated on TiO_2 buffer layer at $P_{O_2} = 10^{-4}$ Torr.

4.3.2 Magnetic domain observation at room temperature

Surface morphology and magnetic images of anatase $Ti_{0.9}Co_{0.1}O_{2-\delta}$ film measured in air and vacuum at room temperature by magnetic force microscopy (MFM) are shown in Figure 4.4. The measurement in vacuum was performed after the film was measured in air and vacuum level of the measurement chamber reached 10 Pa.

The low temperature film growth with TiO_2 buffer layer showed a very flat film surface with step and terrace structure without any segregation at the surface. The step height was corresponding to a quarter of anatase unit cell and the step width was about 150 nm. The RMS roughness was 0.063 nm in an area of $2 \times 2\ \mu m^2$.

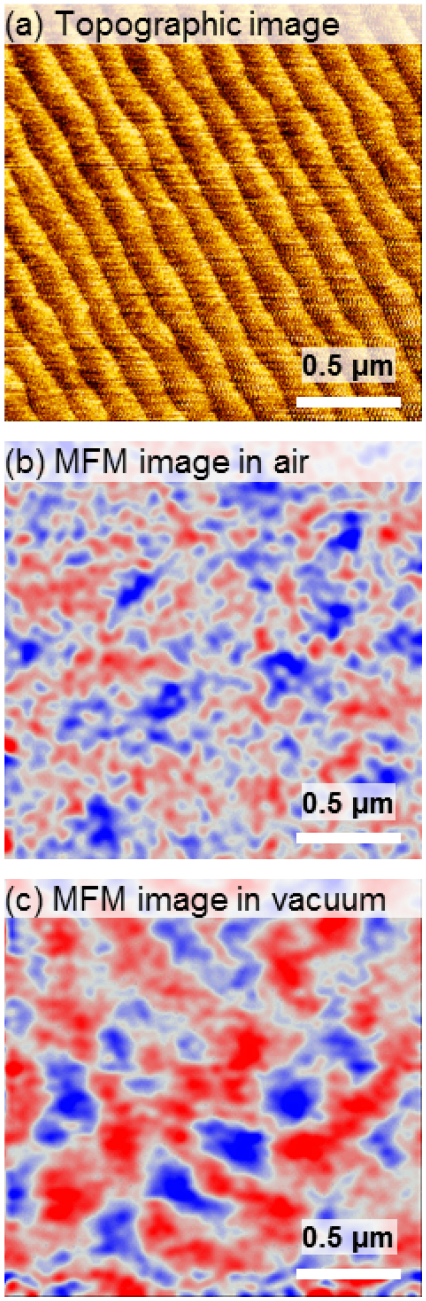

Figure 4.4 (a) Topographic image of anatase $Ti_{0.9}Co_{0.1}O_{2-\delta}$ film and the corresponding MFM images measure in (b) air and (c) in vacuum.

The blue and red colors in the MFM images in Figure 4.4 indicate opposite magnetic directions determining magnetic domain area. Between two magnetic domains, white color can be seen representing magnetic domain walls. The magnetic images obtained in air and vacuum looks very different with different spatial resolution. The magnetic image measured in vacuum exhibited significantly increased MFM signal as well as clear

resolution of submicrometer sized individual magnetic domains without contribution of topographic signal, whereas the magnetic image measured in air showed featureless magnetic image failing to resolve magnetic domains.

The higher sensitivity of MFM in vacuum is related to quality factor (Q-factor) of the cantilever resonance. Q-factor is defined as the ratio of resonance frequency of cantilever ω_0 to its resonance width $\Delta\omega$; $Q = \omega_0/\Delta\omega$. Generally, the sensitivity and resolution of the measurement will be improved when the Q-factor is increased which can be obtained by reducing viscosity of air, i.e. decreasing ambient pressure. In this experiment, the Q-factor was enhanced from 500 to 6000 with decreasing the pressure from atmospheric pressure to vacuum of 10 Pa.

By measuring the atomically smooth film in the vacuum condition, a clear magnetic image without a contribution from topography was obtained. It is noted that the step and terrace structure of a film sometimes generates a step-like MFM image which is difficult to avoid for MFM measurement of the film.

4.3.3 The dependence of magnetic domain structure on carrier density and Co content

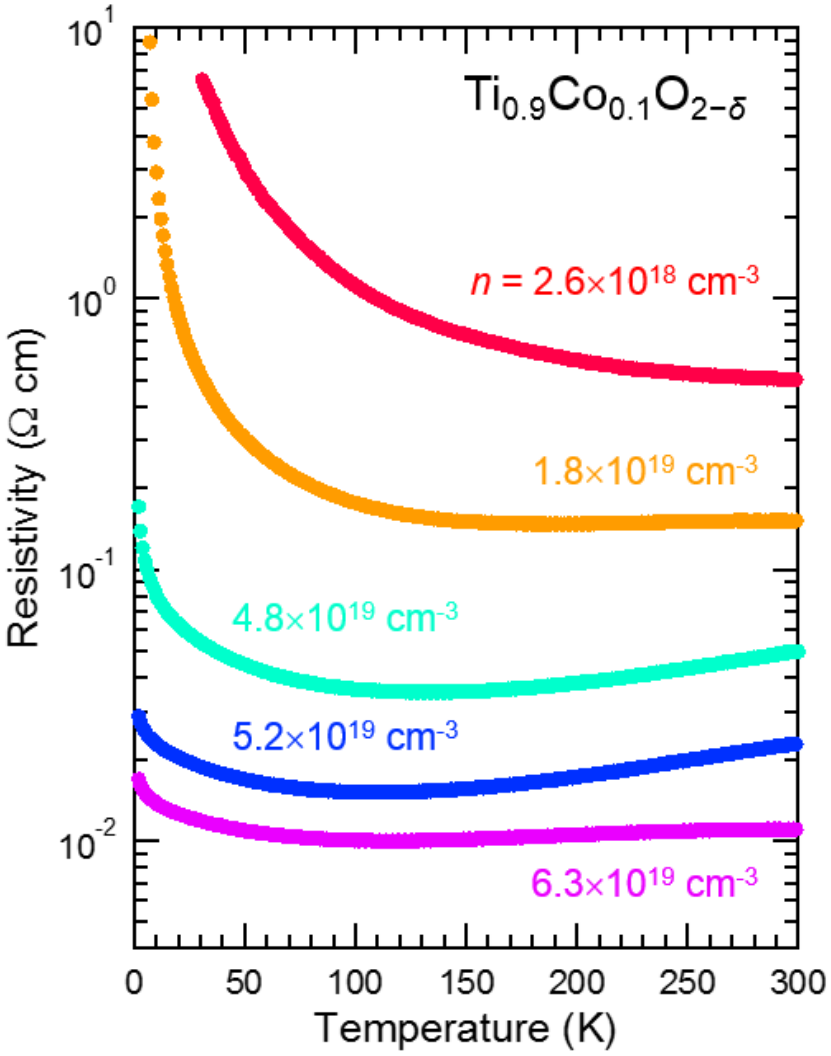

Figure 4.5 The temperature dependence of resistivity of anatase $Ti_{0.9}Co_{0.1}O_{2-\delta}$ films with different carrier density n.

The anatase $Ti_{0.9}Co_{0.1}O_{2-\delta}$ films with different carrier densities were fabricated by controlling the oxygen pressure during the film deposition. The amount of oxygen vacancies acting as electron donors is a good adjustable parameter for controlling the conductivity. Ranging P_{O_2} from 10^{-6} to 10^{-4} Torr, the films exhibited metallic to insulating behavior as shown in Figure 4.5. The carrier density (n) was calculated from

Hall Effect measurement at 300 K labeled in the figure. The range of carrier density was 10^{18} cm^{-3} – 10^{20} cm^{-3}. Magnetization curve of the samples were also measured at 300 K showing increase of hysteresis loop as the carrier density increases, as shown in Figure 4.6.

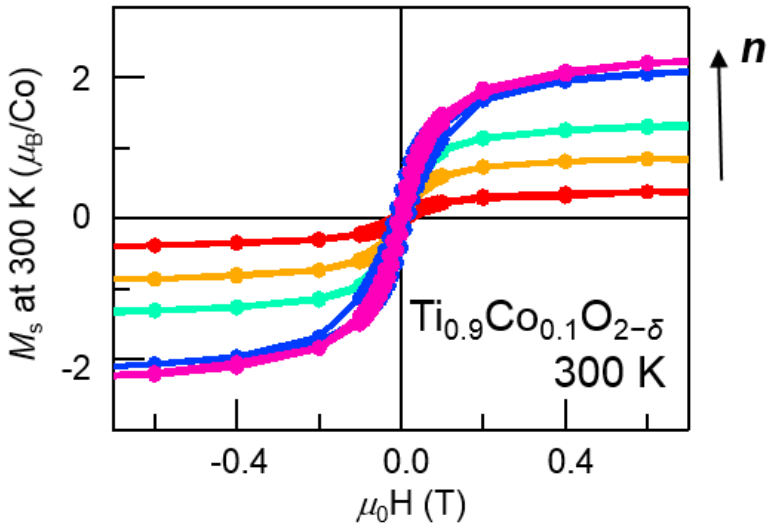

Figure 4.6 The magnetization curve measured at 300 K of anatase $Ti_{0.9}Co_{0.1}O_{2-\delta}$ films with different carrier density *n*. The arrow indicates increasing of *n*.

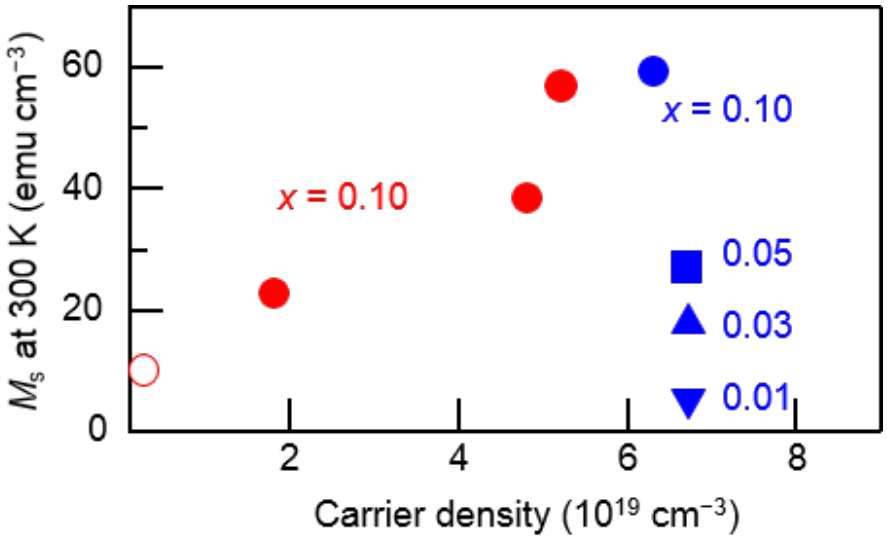

Figure 4.7 The carrier dependence of saturation magnetization at 300 K of $Ti_{1-x}Co_xO_{2-\delta}$ films with different Co contents.

The magnetic domain structure and magnetization were investigated systematically as functions of carrier density (n) and Co content (x). The relationship between carrier density and saturation magnetization (M_s) at 300 K of $Ti_{1-x}Co_xO_{2-\delta}$ films with different Co contents are shown in Figure 4.7.

For x = 0.10, the saturation magnetization (M_s) values were extracted from Figure 4.6 and plotted as red circles showing that M_s increased monotonically with increasing carrier density from 0.4 μ_B/Co to 2.2 μ_B/Co. The white filled red circle at $n = 2.6 \times 10^{18}$ cm^{-3} represents paramagnetic sample determined from almost closed hysteresis loop in magentization curve. The ferromagnetic phase emerged at 2×10^{19} cm^{-3}, being consistent with the previous study of the same x [13] suggesting good reproducibility. The M_s of films with different x were investigated at a similar level of a fixed carrier density, $6.0 - 6.7 \times 10^{19}$ cm^{-3}. A monotonic increase of M_s as a function of x was also observed as blue circles in Figure 4.7.

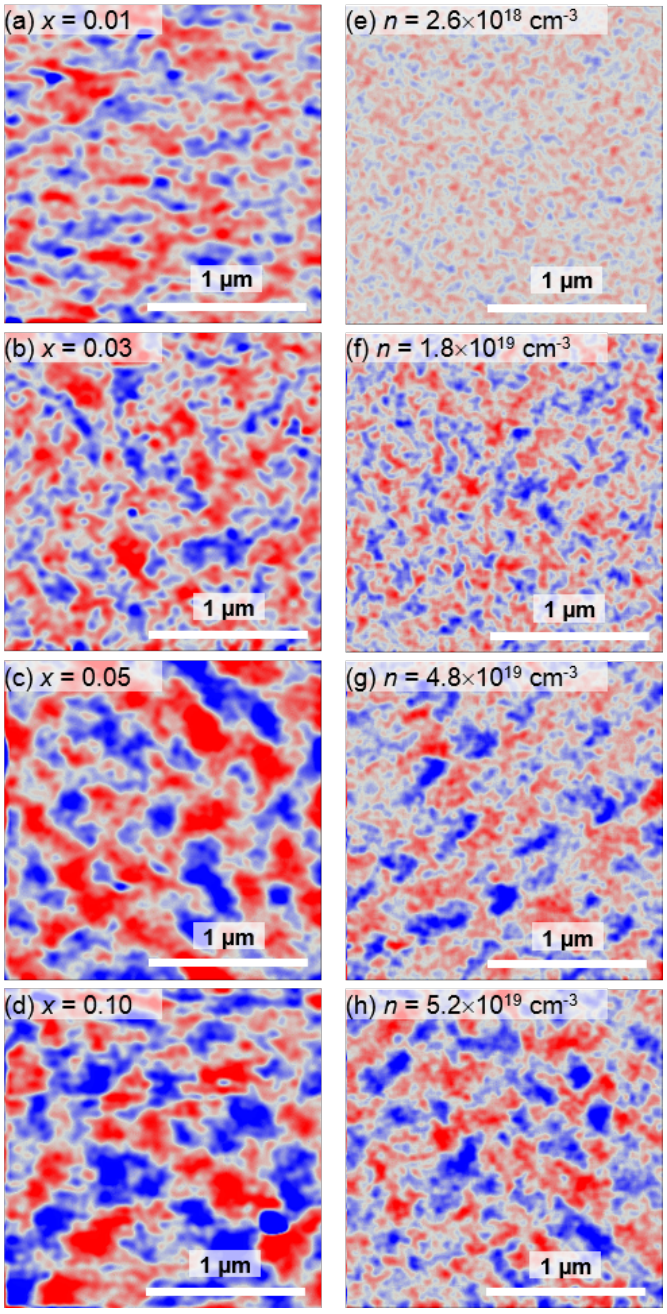

Figure 4.8 Magnetic domain structure in $Ti_{1-x}Co_xO_{2-\delta}$ films observed by MFM at room temperature.

Magnetic domain structures of the above samples were measured at room temperature in vacuum without external magnetic field. Figure 4.8(a)–(d) show magnetic images of the ferromagnetic films with different Co contents varied from x = 0.01 – 0.10. Because of high carrier density, these films showed high contrast magnetic images as their

ferromagnetic nature. From the result, the magnetic domain structure was found to be an increasing function with respect to carrier density and Co content and gradual emergence of magnetic domain was observed suggesting homogeneous ferromagnetism in a microscopic scale. In order to determine the magnetic domain size and other micromagnetic parameters, a quantitative analysis of magnetic domain was performed.

Here, the average magnetic domain width (d) with maze-like domain structure was evaluated by using stereological method, as follows [63]. By drawing random lines across the magnetic domains (Figure 4.9), the average magnetic domain width is determined as $\frac{2\times(\text{Total test line length})}{\pi\times\text{Number of intersections}}$. The carrier density, saturation magnetization and average magnetic domain width of the samples were summarized inTable 4.1.

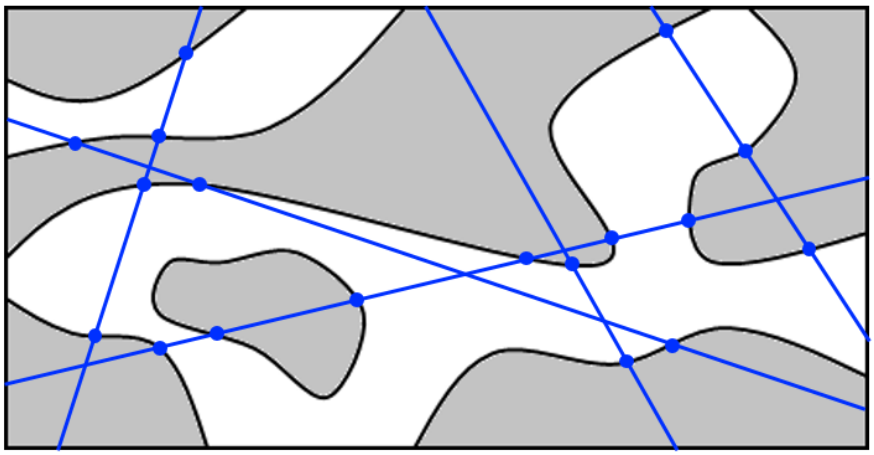

Figure 4.9 Schematic image showing stereological method to estimate average magnetic domain size, d, of maze-like domain structure. Random lines are drawn intersecting with magnetic domain boundaries. $d = \frac{2\times(\text{Total test line length})}{\pi\times\text{Number of intersections}}$.

Table 4.1 Summary of carrier density, saturation magnetization and average magnetic domain width of samples with different Co contents.

Co content	carrier density (cm^{-3})	saturation magnetization (μ_B/Co)	average magnetic domain width (nm)
0.01	6.7×10^{19}	2.0	100
0.03	6.7×10^{19}	2.2	110
0.05	6.7×10^{19}	2.0	160
0.10	6.3×10^{19}	2.3	150
0.10	2.6×10^{18}	0.4	–
0.10	1.8×10^{19}	0.9	70
0.10	4.8×10^{19}	1.4	100
0.10	5.2×10^{19}	2.1	120

The average domain widths for x = 0.01, 0.03, 0.05, and 0.10 were 100, 110, 160, and 150 nm, respectively. A slight increase of average magnetic domain size with x will be discussed based on a micromagnetic model (Equation (4.3)) in the next section. The domain width increased approximately with increasing x, implying stronger and/or longer-range ferromagnetic ordering between adjacent magnetic polarons for higher x. For high concentration of magnetic dopant, the average distance between two adjacent magnetic atoms is smaller than that of low concentration, which results in larger exchange interaction and also thinner domain wall width.

Magnetic images of $Ti_{0.9}Co_{0.1}O_{2-\delta}$ films with different carrier density from 2.6×10^{18} cm^{-3} to 6.3×10^{19} cm^{-3} are presented in Figure 4.8(e)–(h) and (d). At low carrier density, $n = 2.6 \times 10^{18}$ cm^{-3}, the magnetic image showed featureless structure with the level of background signal representing paramagnetic phase (Figure 4.8(e)). For $n = 1.8 \times 10^{19}$ cm^{-3} near paramagnetic-ferromagnetic transition, weak magnetic domain structure was observed (Figure 4.8(f)) associated with an emergence of global ferromag-

netism. For the higher n, the magnetic domain structure became clearer due to the increased magnetization via carrier mediated exchange interaction, and the domain width became larger with increasing carrier density. The average domain widths were 70, 100, 120, and 150 nm for n = 1.8 $\times$ 10^{19} cm^{-3}, 4.8 $\times$ 10^{19} cm^{-3}, 5.2 $\times$ 10^{19} cm^{-3}, and 6.3 $\times$ 10^{19} cm^{-3}, respectively. The observed magnetization vs. carrier density relation is consistent with previous result reported by Yamada *et al.* [13]. A transition from paramagnetic phase to ferromagnetic phase with increasing carrier density is microscopically evidenced in this study, representing close connection between the bulk magnetic properties and magnetic domain structure. At the intermediate carrier density, near the ferromagnetic transition, the non-zero ferromagnetic magnetization despite of negligible anomalous Hall effect reported previously [13] might imply the existence of phase separation state. Ferromagnetic embryos embedded in paramagnetic phase were also discussed in (Ti,Co)O_2 [50]. Probably, the magnetic domain structure with less magnetic force signal like in Figure 4.8(e) and (f) might represent such state while further carrier doping results in global ferromagnetism as seen in Figure 4.8(g), (h) and (d). However, in order to observe such ferromagnetic embryo clearer, more sensitive measurement by using e.g. scanning SQUID microscope will be needed for further investigation.

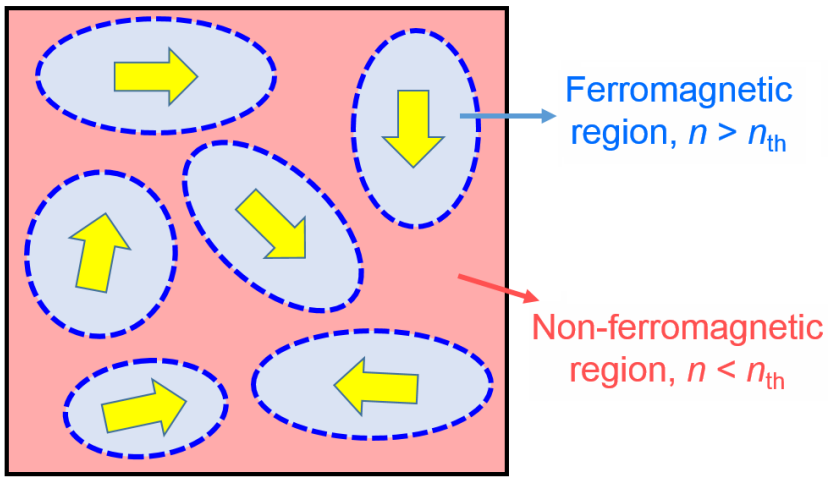

Figure 4.10 Illustration of discrete multi-domains where ferromagnetic region separated by large paramagnetic region. n_{th} denotes threshold carrier density for ferromagnetic transition.

It is noted that (In,Fe)As with carrier density just above the ferromagnetic transition threshold showed magnetic domain structure representing discrete multi-domains, similar to phase separation state. The difference in local carrier density originated ferromagnetic region which was separated by large paramagnetic region as illustrated in Figure 4.10 [70]. Such an inhomogeneous ferromagnetic state of (In,Fe)As was observed by magneto-optical imaging under zero magnetic field at 4 K.

Before continuing the next part, I would like to note that the magnetic domain as a function of Co content was also reproduced in a moderately high carrier density region ($n = 4 - 5 \times 10^{19}$ cm^{-3}) despite the smaller MFM signal and average magnetic domain width (Figure 4.11) compared to those previously discussed in this session. The increase of magnetic contrast and magnetic domain size for higher Co content films measured by MFM in this experiment was also consistent with those measured by a scanning SQUID microscope [9].

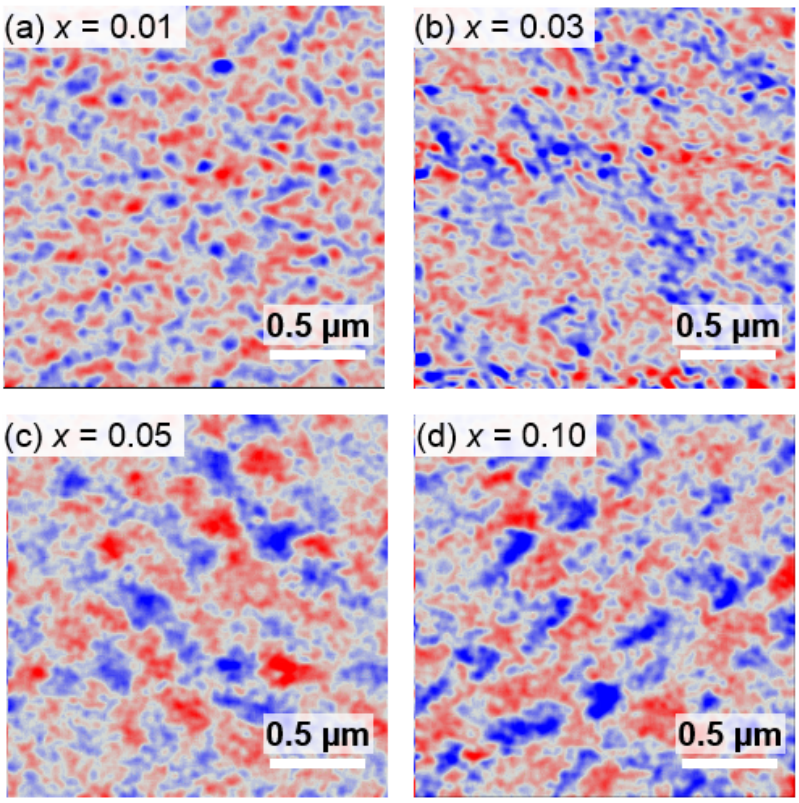

Figure 4.11 The magnetic domain structure in $Ti_{1-x}Co_xO_{2-\delta}$ films at moderate carrier density, n= 4 – 5 × 10^{19} cm^{-3}.

4.3.4 Micromagnetic parameters

I evaluated micromagnetic parameters of uniaxial magnetic anisotropic constant (K_u), magnetic domain wall energy (σ_w), and exchange stiffness constant (A) at 300 K. K_u was obtained via modified Sucksmith-Thomsons method by using magnetization curve of each sample [71,72]. The modified Sucksmith and Thompson equation is shown in Equation (4.1),

$$\frac{H \cdot \alpha}{M - M_r} = \frac{2 \cdot K_1}{M_s^2} + \frac{4 \cdot K_2}{M_s^4}\left(\frac{M - M_r}{\alpha}\right)^2 \tag{4.1}$$

where α is defined as $\frac{M_s - M_r}{M_s}$, H is the magnetic field (T), M, M_s and M_r are the magnetization, the saturatiion magnetization and the remanant magnetization, and K_1 and K_2 are the first and second order magnetic anisotropy constant.

By using magnetization at the initial state of the in-plane magnetization measurement, I can obtain the plot between $\frac{H \cdot \alpha}{M - M_r}$ and $(\frac{M - M_r}{\alpha})^2$. From the slope and y-intercept , one can determine K_1 and K_2 by using curve fitting. The uniaxial magnetic anisotropy (K_u) is obtained from K_1 + K_2. An example of modified Sucksmith-Thompson plot of $Ti_{0.95}Co_{0.05}O_{2-\delta}$ film is shown in Figure 4.12.

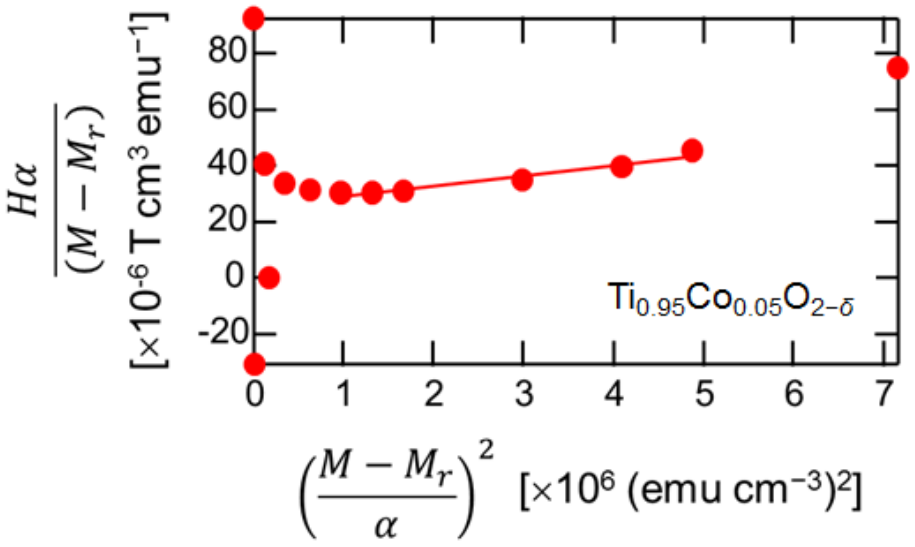

Figure 4.12 Modified Sucksmith-Thompson plot of anatase $Ti_{0.95}Co_{0.05}O_{2-\delta}$ films.

The results of K_1 and K_2 are positive indicating out-of-plane magnetization in (Ti,Co)O_2 films. For $x = 0.05$, the uniaxial anisotropy constant, K_u, was estimated as 4.2×10^3 J/m^3. Generally, one can use the quality factor, $Q' = \frac{K_u}{K_d}$, where K_d is the shape anisotropy related to demagnetizaing field, in order to classified whether magnetization of films lies in-plane or out-of-plane. The K_d can be calculated as $K_d = \frac{1}{2} \cdot \mu_0 {M_s}^2$. When $Q' < 1$, the demagnetizing field is considered to be dominant and the magnetization of the film lies in-plane totally. On the other hand, when $Q' > 1$, the uniaxial magnetic anisotropy governs the formation of magnetic domains resulting in a system of stripe domain and development of out-of-plane component. In the present films, the $Q \gtrsim 1$ was obtained suggesting that the (Ti,Co)O_2 film has a mixture between strip domain and maze like

pattern which is consistent with maze-like domain with vague domain walls observed in this experiment.

Next, domain wall energy (σ_w) was estimated from the dipolar length (D_0) described as the $D_0 = \frac{\sigma_w}{2 \cdot \pi \cdot {M_s}^2}$. The D_0 deduced from thickness dependence of magnetic domain width [73] was approximately 15 nm for $x = 0.05$. Assuming same D_0 for other x, σ_w for each films with different Co contents and carrier densities were estimated. The magnetic stiffness constant A was calculated from K_u and σ_w according to Equation (4.2).

$$\sigma_w = 4 \cdot \sqrt{A \cdot K_u} \tag{4.2}$$

The obtained micromagnetic parameters were plotted as solid symbols and interpolated by color mapping as shown in Figure 4.13. All three micromagnetic parameters increase as carrier density and Co content increase. The relationship between d, M_s and σ_w (Equation (4.3)) suggests that the magnetic domain with is governed by the balance of both of M_s and σ_w which are increasing functions of carrier density and Co content. Film with higher x and n has higher σ_w and M_s resulting in larger average magnetic domain size which is consistent with the result in Figure 4.8.

Since the magnetic domain is governed by both of M_s and σ_w, the increase of M_s for very high carrier films suppresses an increase of magnetic domain size as expressed in Equation (4.3), resulting in a small decrease of magnetic domain size at very high x.

$$d \propto \frac{\sqrt{\sigma_w}}{M_s} \tag{4.3}$$

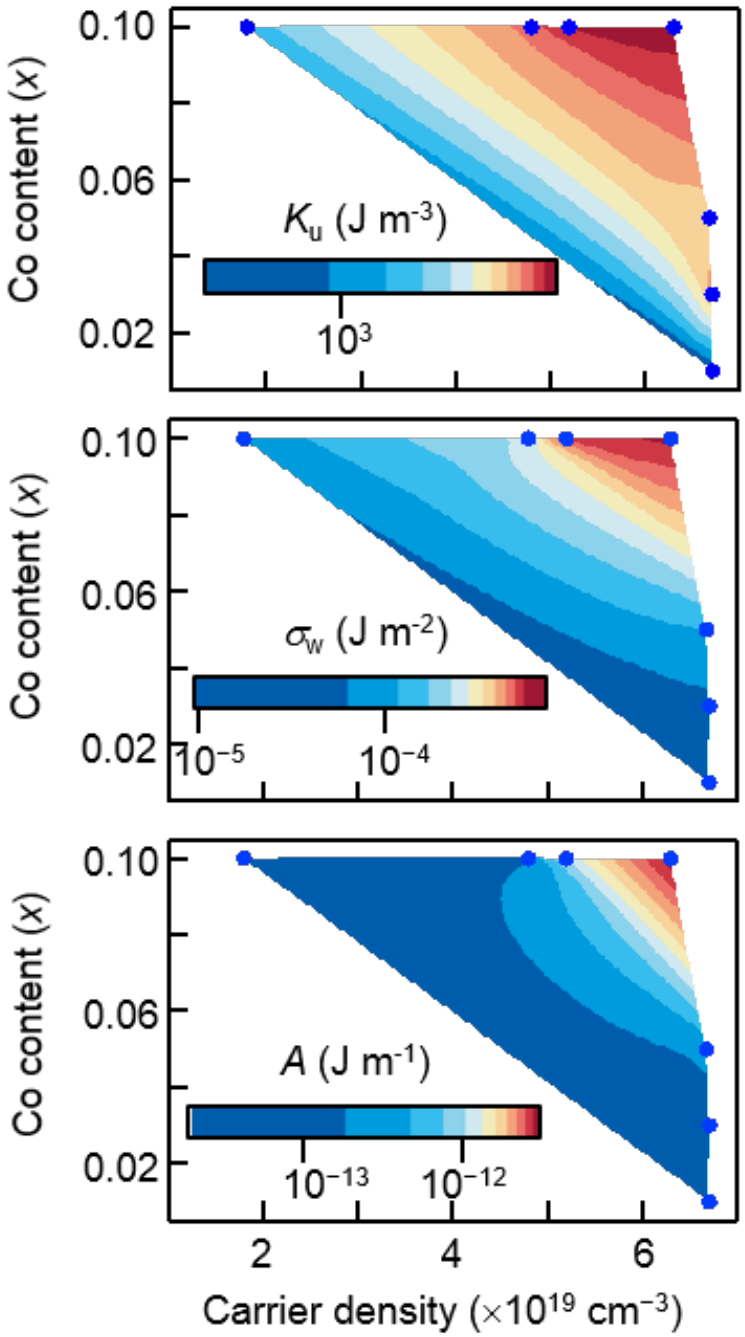

Figure 4.13 Micromagnetic parameters at 300 K as functions of Co content (x) and carrier density (n). Solid symbols correspond to the evaluated data points that are interpolated by color mapping.

From the results, the range of K_u, σ_w and A is 10^3 to 10^4 J/m^3, 10^{-6} to 10^{-3} J/m^2 and 10^{-16} to 10^{-12} J/m, respectively. These value ranges of microparameters are comparable

to those of (Ga,Ma)As, previously reported in both theoretical and experimental studies [74–76]. In addition, the small value of stiffness constant (A) in comparison to that of ferromagnetic metal also indicates the diluted nature in (Ti,Co)O_2 system. The stiffness constant is roughly propotional T_C and also the exchange constant (J); $A \approx JS^2Z_c/a_0$. Therefore, the small A value also indicates small exchange constant, J.

Table 4.2 Summary of evaluated micromagnetic parameters.

	(Ti,Co)O_2 (in this study)	(Ga,Mn)As [18, 75]
Magnetic anisotropy (J/m^3)	$10^3 - 10^4$	$10^3 - 10^4$
Domain wall energy (J/m^2)	$10^{-6} - 10^{-3}$	$10^{-5} - 10^{-4}$
Stiffness constant (J/m)	$10^{-16} - 10^{-12}$	$10^{-14} - 10^{-13}$
Average magnetic domain wall width (nm)	80 – 160	1500

It should be noted that the A derived from magnetic domain structure in this experiment has a very large error due to the experimental uncertainties and assumption used for calculating the value. Generally, the best way to derive A is estimation from spin-wave stiffness in magnon dispersion since the energy of spin waves is directly connected to a gradual change of the magnetization.

4.4 Conclusions

Magnetic domain structure in anatase $Ti_{1-x}Co_xO_{2-\delta}$ epitaxial thin films was successfully observed by magnetic force microscope at room temperature in vacuum condition. Without external magnetic field, the magnetic domain structure can be obtain

revealing maze-like structure. Systematic study of the domain as functions of carrier density and Co content was performed indicating homogeneous microscopic ferromagnetism. For high carrier density and Co content, the magnetic domain structure was clearly observed. The magnetic domain structure showed systematic dependence on carrier density with homogeneous magnetic domains: negligible magnetic domain structure for $n < 10^{19}$ cm^{-3} and emerged magnetic domain structure for $n \geq 2 \times 10^{19}$ cm^{-3}, showing good coincidence of bulk magnetization measurement. In addition, micromagnetic parameters of uniaxial magnetic anisotropic constant, magnetic domain wall energy, and exchange stiffness constant at 300 K were evaluated indicating increasing functions of both carrier density and Co content. The range of these micromagnetic parameters also indicates the diluted nature in (Ti,Co)O_2 system.

This microscopic study of (Ti,Co)O_2 is a step-forward for magnetic domain manipulation with room temperature ferromagnetic semiconductor in which lower energy consumption comparing to the conventional ferromagnetic metal, might be expected. In addition, the good consistency between microscopic and macroscopic magnetism as well as no apparent phase separation is an important evidence for homogeneous ferromagnetism with high T_C in this compound.

Chapter 5

Development of non-magnetic capping layer TiO_2

The existence of magnetically dead layer at surface or interface is a common issue in magnetic materials for both bulk and thin film forms. A remedy for surface magnetization with prohibiting or reducing a formation of uncontrollable magnetically dead layer is necessary for device applications, which sometimes require ultrathin film. Furthermore, it is also important from a viewpoint of magnetization stability. In this chapter, I reported the development of non-magnetic capping layer of TiO_2 for $Ti_{1-x}Co_xO_{2-\delta}$ films. The result suggested improved magnetization as well as enhanced magnetic anisotropy. The capped films show higher magnetization stability at least for 2 years. In addition, the total film thickness can be reduced down to 10 nm without degrading magnetization which enables the observation of magnetic domain structure even in very thin films. The simple capping process will be advantageous for utilizing $(Ti,Co)O_2$ in further device manipulations.

5.1 Introduction

For $(Ti,Co)O_2$, the significant decrease of surface magnetization was previously evidenced by x-ray magnetic circular dichlorism (XMCD) measurement [42]. A possible reason for this magnetically dead layer is attributed to surface oxidation or depletion layer, where the carrier density is suppressed due to the different surface and bulk electronic structure. The x-ray photoemission spectroscopy (XPS) clearly indicated a smaller amount of Ti^{3+} at film surface comparing to bulk region [77]. This surface ox-

idation or depletion region could be resolved under ultraviolet illumination on anatase $Ti_{1-x}Co_xO_{2-\delta}$ thin films resulting in introduction of photoinduced carriers to compensate the deficient carriers at the surface [43]. Use of capping or seeding layer is known to be a common method to protect surface oxidation or interface problem [46, 47]. In this chapter, I developed non-magnetic ultrathin capping layer for anatase (Ti,Co)O_2 epitaxial thin film and investigated its magnetic properties in comparison with non-capped film. Moreover, thickness dependence of magnetization in capped films was also evaluated suggesting that the capping layer could reduce the magnetically dead layer at the surface.

5.2 Experimental details

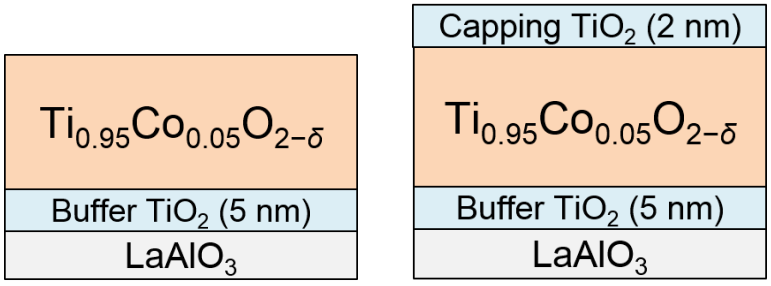

(a) non-capped film **(b)** capped film

Figure 5.1 Schemes of film structure (a) non-capped film and (b) capped film.

Anatase $Ti_{0.95}Co_{0.05}O_{2-\delta}$ (001) thin films were epitaxially grown on $LaAlO_3$ (001) step substrates buffered with 5 insulating TiO_2 unit cells by pulsed laser deposition (PLD) with KrF excimer laser using the same procedure as the previous chapter. On the buffer layer, anatase $Ti_{0.95}Co_{0.05}O_{2-\delta}$ epitaxial thin film were grown at 250 °C, $P_{O_2} = 1 - 3\times10^{-6}$ Torr. Then, non-magnetic capping layer of TiO_2 was fabricated soon after the deposition of $Ti_{0.95}Co_{0.05}O_{2-\delta}$ layer. The growth temperature for capping layer was fixed at 250 °C, same as the growth temperature of $Ti_{0.95}Co_{0.05}O_{2-\delta}$ films, and $P_{O_2} =$

10^{-4} Torr in order to obtain relatively insulating TiO_2. The structures of non-capped film and capped film are compared in Figure 5.1. Epitaxial growth of pure anatase phase with *c*-axis orientation was confirmed by XRD in all films. Electric transport and magnetic properties of the films were investigated by four-probe method and SQUID magnetometer, respectively. The topographic and magnetic images of capped and non-capped films were observed by magnetic force microscope (MFM) at room temperature under vacuum (10 Pa) without external applied magnetic field.

5.3 Results and Discussions

5.3.1 Characterization of capped films

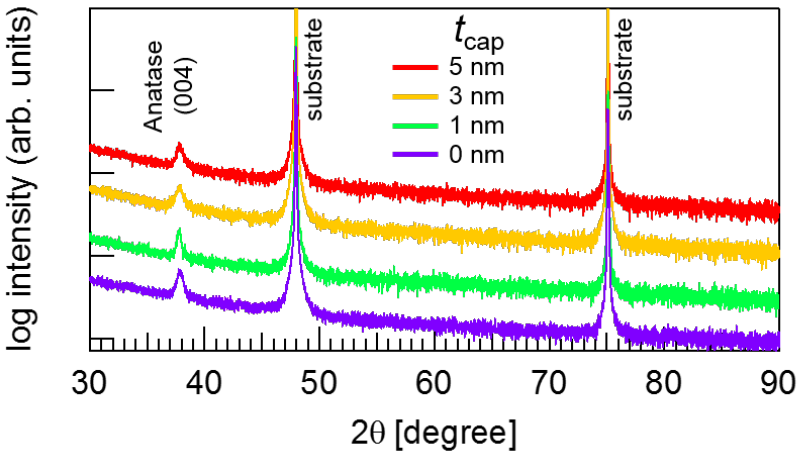

Figure 5.2 XRD diffraction patterns of capped films with different capping thickness, t_{cap} = 5, 3, 1 and 0 nm.

The capped films with different capping thickness, t_{cap} = 5, 3, 1 and 0 nm were grown and their XRD diffraction patterns are shown in Figure 5.2. The total film thickness was ∼35 nm. All films showed anatase (004) peak around 37.8° without other impurity phases. The intensity of anatase (004) peaks were not so different among those with different capping thicknesses. The peaks showed broadening due to large amounts of oxygen vacancies in the films grown at low oxygen pressure (∼ 10^{-6} Torr). The cal-

culated *c*-axis lattice constants showed a small deviation in the range of 9.50-9.52 Å, comparable to that of bulk anatase TiO_2.The topographic images of the films are presented in Figure 5.3. Root-mean-square roughness in an area of $2 \times 2\ \mu m^2$ is less than 1 nm.

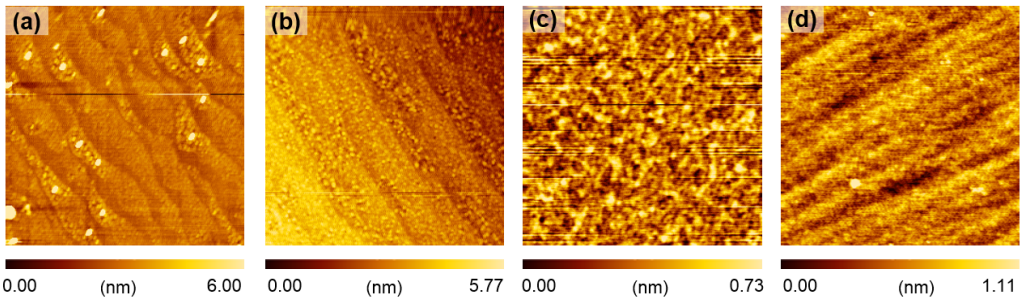

Figure 5.3 Topographic images of capped films with different capping thickness, (a)-(d) t_{cap} = 5, 3, 1 and 0 nm.

5.3.2 Electrical transport properties of capped films

Temperature dependence of resistivity of the films with non-magnetic capping layer of 0 nm to 5 nm were measured by 4-probe method with Hall bar patterned samples as shown in Figure 5.4.

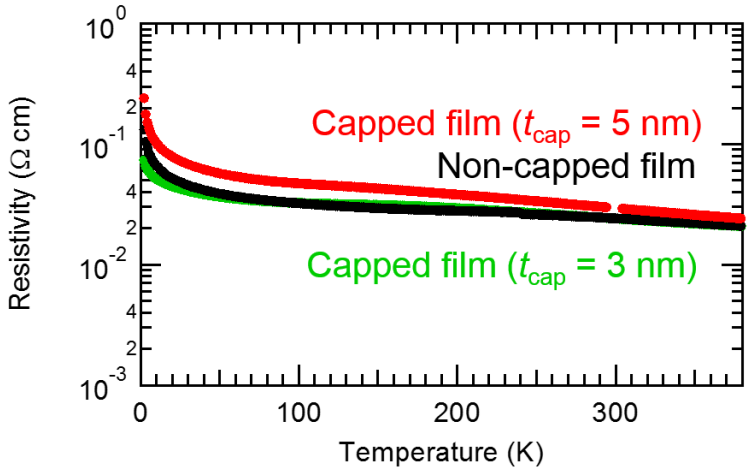

Figure 5.4 Temperature dependence of resistivity of capped films with t_{cap} = 5 and 3 nm, compared with non-capped film.

The resistivity was calculated by assuming that only (Ti,Co)O_2 layer contributes to electric conduction. The 3 nm capped film showed almost no different with non-capped film while 5 nm capped showed a slight increase in resistivity probably due to slightly decreased carriers within an experimental error range. That is, no significant change in resistivity was found for the capped films. This suggests that carrier doping at the interface does not occur in this case. According to Hall measurement at 300 K, the carrier density at 300 K was calculated to be $\sim 5 \times 10^{19}$ cm^{-3} and the Hall mobility of these films was 4.5–5.4 cm^{2}V^{-1}s^{-1}. At this high carrier density, one may estimate the depth of magnetically dead layer, if it exists, to be about 10 nm [43]. It should be noted that the capping layer might not be a complete insulator due to low growth temperature of 250°C, as discussed in previous study [69], and may cause overestimation of the film conductivity.

5.3.3 Effect of capping layer on magnetization

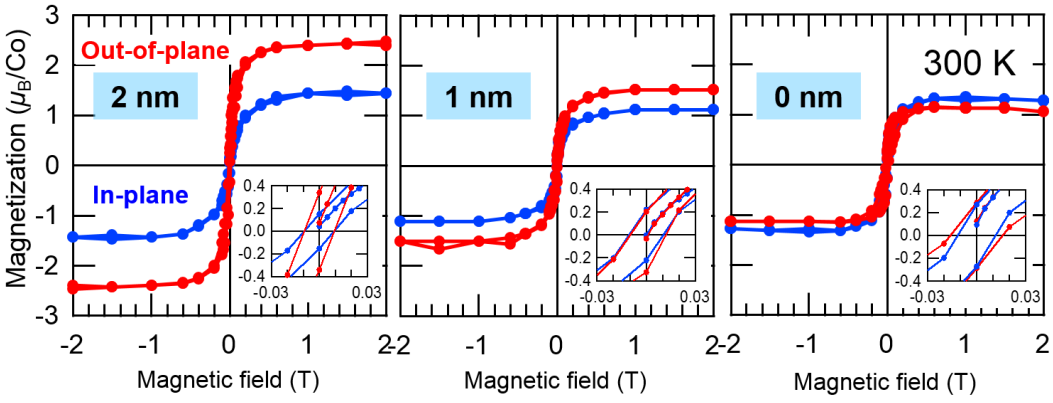

Figure 5.5 Out-of-plane (red) and in-plane (blue) magnetization curves at 300 K of anatase $Ti_{0.95}Co_{0.05}O_{2-\delta}$ epitaxial thin films with different of capping layers varied from 0 to 2 nm is labelled in the figure.

Figure 5.5 shows out-of-plane (red) and in-plane (blue) magnetization curves measured at 300 K of anatase $Ti_{0.95}Co_{0.05}O_{2-\delta}$ epitaxial thin films with different thicknesses

of capping layers of 0, 1 and 2 nm. These films have a moderate carrier density of $\sim 4.5 \times 10^{19}$ cm^{-3}. The out-of-plane magnetization was increased from 1.1 μ_B/Co to 2.4 μ_B/Co for the capped film with t_{cap} = 2 nm, whereas the in-plane magnetization was almost unchanged. In addition, the capped films showed slightly larger coercive force. Because higher carrier generally resulted in higher magnetization, the improved magnetization in the capped films might come from carriers induced by the overlayer as reported at the interfaces of TiO_2/$LaAlO_3$ and TiO_2/$LaTiO_3$ [78]. However, the results of transport measurements clearly ruled out this possibility and therefore, the increased out-of-plane magnetization shown in Figure 5.5 was not attributed to such transport properties.

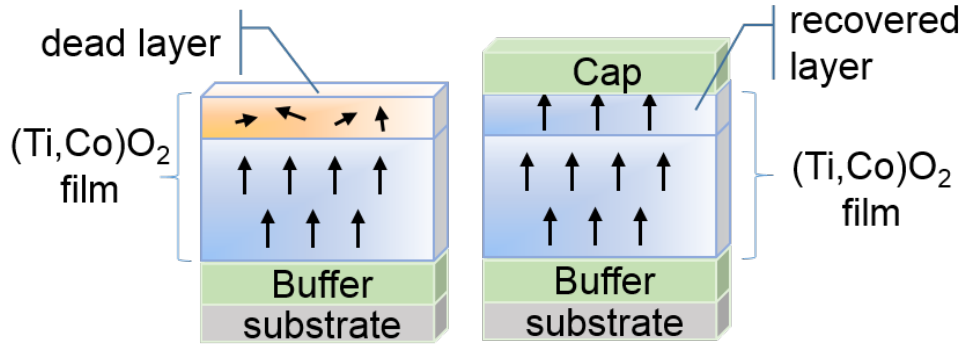

Figure 5.6 Illustration of a possible reason for recovered magnetization at top surface by using capping layer.

Besides the improved magnetization, out-of-plane magnetic anisotropy was also enhanced. Actually, (Ti,Co)O_2 films with enough thickness usually show out-of-plane magnetic anisotropy (supporting material of ref. [16]) with uniaxial magnetic anisotropic constant $\sim 10^3 - 10^4$ J/m^3 although the origin of the magnetic anisotropy is still unknown. I speculate that surface magnetization at the top several nanometers was recovered by using the cap layer and competed with shape anisotropy which induces in-plane anisotropy for very thin film, resulting in enhanced out-of-plane magnetization (Figure 5.6). Enhanced magnetic anisotropy was also reported to be related with capping layer thickness and different capping layer [79, 80], and the induced interfacial per-

pendicular anisotropy was used to explain the different magnetic anisotropy. Thus it is also possible that the enhanced magnetic anisotropy originates from the perpendicular anisotropy at the TiO_2/(Ti,Co)O_2 interface.

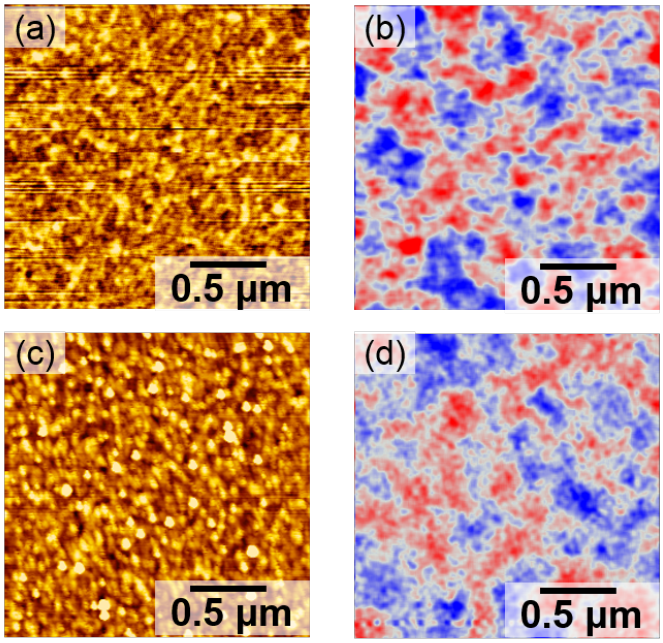

Figure 5.7 (a) and (b) show topographic and its corresponding MFM images of capped film. (c) and (d) are topographic and its corresponding MFM images of non-capped film.

Topographic and magnetic images of the capped film with t_{cap} = 2 nm and non-capped film are shown in Figure 5.7. Both films exhibit similar surface morphology and magnetic images with similar maze-like domain patterns and domain widths. For the capped film, the MFM image exhibits a little higher magnetic contrast probably due to enhanced magnetization as presented in Figure 5.6.

Next, I also investigated the stability of non-capped and capped films as time dependence of magnetization. After the films were fabricated and their physical properties were measured, the films were kept in a desiccator at ambient condition without other treatments. The out-of-plane magnetization at 300 K for as-deposited, 1 year aged and 2 years aged $Ti_{0.95}Co_{0.05}O_{2-\delta}$ thin films were investigated and compared between

capped film with t_{cap} = 2 nm and non-capped film. The carrier density at 300 K of both films evaluated as deposited was $\sim 6 \times 10^{19}$ cm^{-3}. At this high carrier density, both films showed large magnetization indicating thinner dead layer in higher carrier density film [43]. Figure 5.8 represents time dependence of magnetization of the capped and non-capped films. The hysteresis curve of non-capped film showed that the magnetization was decreased to about half after 2 years, on the other hand, only a slight decrease of magnetization was observed in the capped film. The coercive field of capped films are almost unchanged. This result demonstrated a potential of film protection from natural oxidization process at ambient condition by using the non-magnetic capping layer.

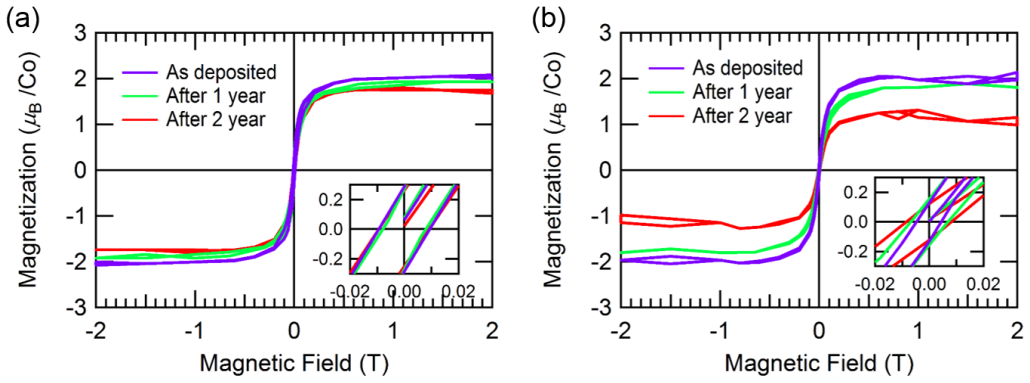

Figure 5.8 Out-of-plane magnetization measured at 300 K for as deposited, 1 year aged and 2 years aged (a) capped film and (b) non-capped film.

5.3.4 Thickness dependence of magnetization of capped films

The 2 nm-TiO_2 capped $Ti_{0.95}Co_{0.05}O_{2-\delta}$ thin films with approximate film thickness, t (including the thickness of both TiO_2 buffer and (Ti,Co)O_2 layer) of 45, 35, 20 and 10 nm were subjected to the out-of-plane magnetization measurements at 300 K by SQUID magnetometer. Figure 5.9 shows thickness dependence of magnetization curves of the capped films indicating that the magnetization can be maintained even at very thin 10 nm film which is in contrast with the decreased magnetization due to magnetically dead layer in non-capped films. This suggests that the TiO_2 capping layer can reduce or

eliminate magnetically dead layer for $Ti_{0.95}Co_{0.05}O_{2-\delta}$ films.

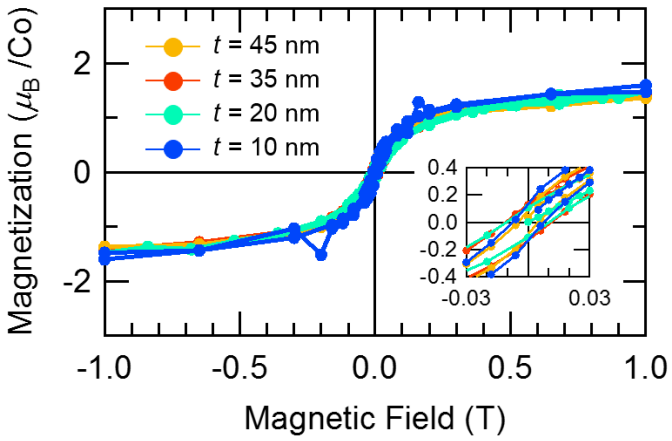

Figure 5.9 Out-of-plane magnetization measured at 300 K of 2-nm TiO_2 capped $Ti_{0.95}Co_{0.05}O_{2-\delta}$ films with film thickness (t) varied from 10 – 45 nm.

Figure 5.10 shows topographic and magnetic images of the $(Ti,Co)O_2$ films capped with 2-nm TiO_2 measured by MFM. The film thickness, t, was varied in the range of 10–45 nm. The magnetic domain structure of the capped $(Ti,Co)O_2$ films with t = 30 and 40 nm, showed high contrast although the non-magnetic capping layer would slightly shield the magnetic stray field. For the film with films with t = 15 nm, a decrease of magnetic domain size as well as its intensity was observed in the capped films. Intriguingly, for the film with t = 10 nm, a finite magnetic domain was observed in contrast with almost featureless magnetic domain structure seen in the non-capped film (Figure 5.11). Comparing to the surface topography (Figure 5.10(d)), this magnetic domain was not related to any surface structures. Therefore, the magnetic domain observation for very thin film was enabled as a result of a protection of surface magnetization by the capping layer.

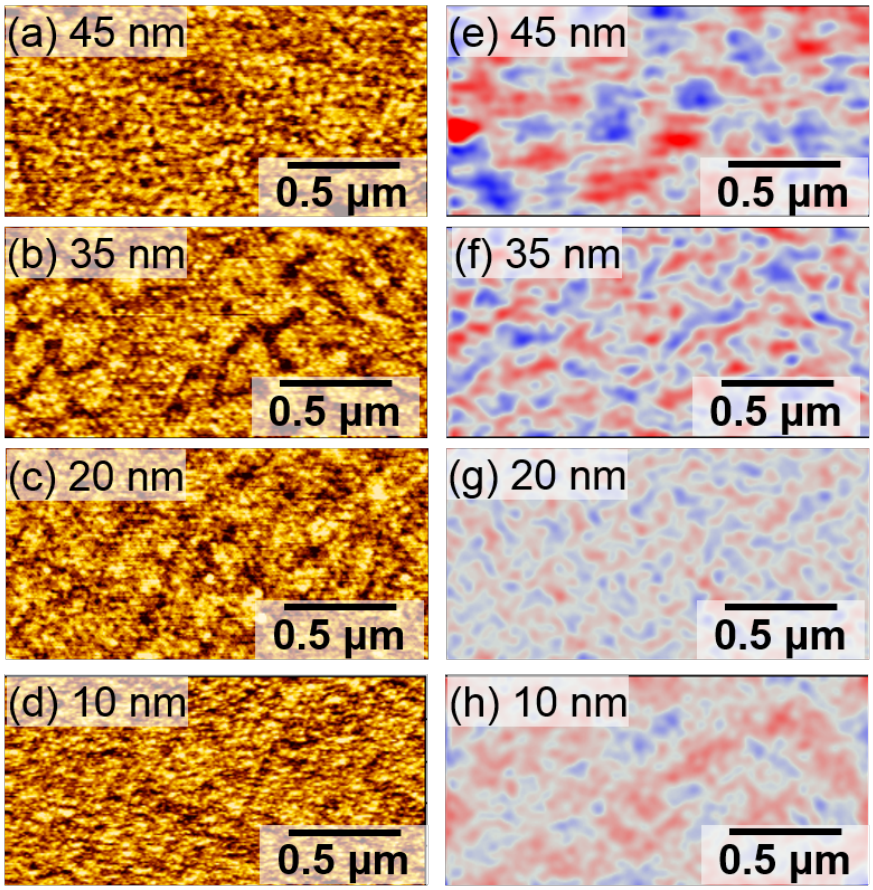

Figure 5.10 (a)-(d) Topographic images of 2-nm TiO_2 capped $Ti_{0.95}Co_{0.05}O_{2-\delta}$ films and (e)-(h) the corresponding magnetic images measured at room temperature. The film thickness t, (including the thickness of both TiO_2 buffer and $(Ti,Co)O_2$ layer) was labelled in the figure.

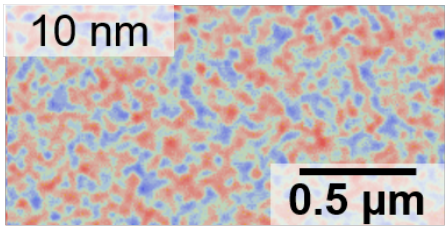

Figure 5.11 The magnetic images of non-capped $Ti_{0.95}Co_{0.05}O_{2-\delta}$ film with t = 10 nm measured at room temperature.

The average magnetic domain width of the films in Figure 5.10 were evaluated by stereological method [63]: 160, 120, 80 and 160 nm for the capped films with t = 45, 35, 20 and 10 nm, respectively. The averaged magnetic domain width tended to decrease

with decreasing t but it became very large at the very thin film. This behavior is similar to that of ferromagnetic metal with stripe domain such as FePt [73]. The increase of magnetic domain size at very thin film suggests that the film could not have perpendicular anisotropy.

From the thickness dependence of magnetic domain width, a specific parameter of dipolar length (D_0) can be determined. Magnetic domain width (d) is known to be an increase function of film thickness (t), when t is considerably large and can be expressed as,

$$d \propto \sqrt{t \times D_0} \tag{5.1}$$

On the other hand, a different function is derived when film thickness is very thin and comparable to dipolar length,

$$d \propto t \times e^{\pi D_0 / 2t} \tag{5.2}$$

Dipolar length can be deduced by plotting $\ln(d/t)$ vs. $1/t$. Dipolar length can be obtained from the slope of linear fitting. The dipolar length of $Ti_{1-x}Co_xO_{2-\delta}$ film with x = 0.05, was deduced to be about 15 nm as shown in Figure 5.12. Thus, the dipolar length is comparable to the film thickness. This explains why the magnetic domain width is enlarged in the film with the thickness of (Ti,Co)O_2 layer = 10 nm. The deduced D_0 was used to estimate the micromagnetic parameters in Chapter 4.

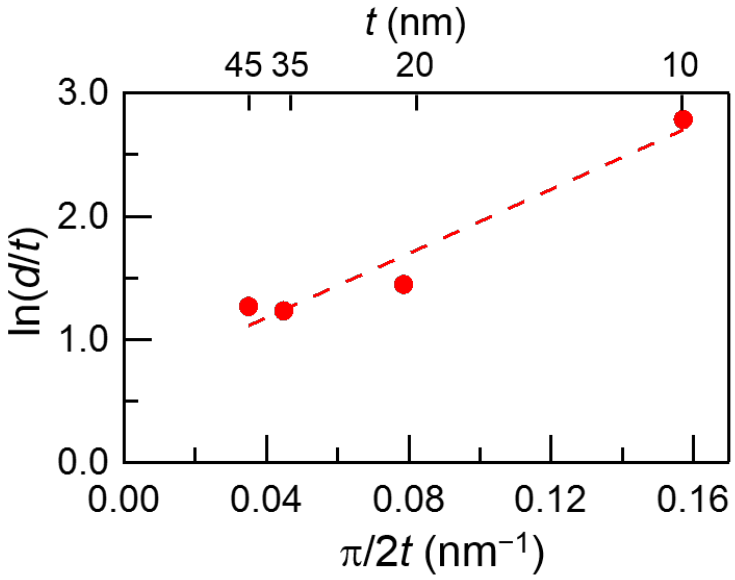

Figure 5.12 A plot of $\ln(d/t)$ vs. $1/t$, where d and t are average magnetic domain width and film thickness of anatase $Ti_{0.95}Co_{0.05}O_{2-\delta}$ films capped with TiO_2 capping layer. Dash line represents linear fitting of the data.

5.4 Conclusions

In conclusion, ultrathin TiO_2 capping layer was developed for anatase (Ti,Co)O_2 (001) epitaxial thin film. The effect on magnetism was investigated at 300 K proving improved magnetization and enhanced perpendicular anisotropy with 2 nm-TiO_2 capping layer. In addition, the capping layer was useful to maintain magnetization stability at least for two years during which the magnetization was almost undegraded. The magnetic domain structure was investigated at room temperature as a function of film thickness and clear magnetic domains were observed even in the very thin capped film. Considering nearly unchanged electric properties for non-capped and capped films, the role of capping layer is to prevent formation of surface depletion region with deficient electron carriers. The capping layer will be useful for decreasing the thickness of magnetically active (Ti,Co)O_2 film and thus, for future spintronics devices based on this material.

Chapter 6

Relation of T_C vs. n and high T_C ferromagnetism in anatase (Ti,Co)O_2 *

Curie temperature (T_C) of (Ti,Co)O_2 is known to be very high over than room temperature ($\sim$600 K). Although it is well established that the electron carriers play an important role for its ferromagnetism, the origin of the high T_C is still unclear. In this chapter, I systematically investigated the T_C of anatase (Ti,Co)O_2 thin films from electrical transport and magnetization measurements at lower temperatures than T_C. The estimated T_C from both measurements showed a good agreement. The relation of T_C vs. n in (Ti,Co)O_2 was investigated indicating that T_C was not monotonically increasing function of carrier density in contrast with an ordinary carrier-mediated exchange coupling. A combination of two mechanisms, carrier mediation and bound magnetic percolation, might account for high T_C in ferromagnetic oxide semiconductors.

Moreover, I also studied possible substructures which might reside inside anatase (Ti,Co)O_2. The substructure scenario recently attracts much attention from a view point of high T_C's origin and nucleation center of bound magnetic polarons. Here, I performed density functional theory (DFT) calculation in order to optimize and propose possible substructures by considering total structure stability.

---

* A part of this chapter including figures has been accepted for publishing in *AIP Advances* in May 2016 special issues (A proceedings of *13th Joint MMM-Intermag Conference*).

6.1 Introduction

Curie temperature (T_C) is one of fundamental parameters of ferromagnetic materials. T_C as a function of carrier density (n) could be a key information for investigation of the origin of high T_C in ferromagnetic oxide semiconductors. However, the T_C of (Ti,Co)O_2 has not been investigated systematically doubting some researchers whether the T_C of (Ti,Co)O_2 exhibits abrupt or gradual increase function of carrier density. In a system which delocalized or weakly localized carriers are dominated, T_C is an increase function of carrier density and magnetic impurity as explained by Zener model. On the other hand, in a system of low carrier where localized carriers account for majority, a dome-shaped T_C vs. n or non-monotonic function of carrier density and magnetic impurity is predicted and bound magnetic polaron mechanism is taken into account.

In order to investigate ferromagnetic T_C of (Ti,Co)O_2 systematically, sample parameters of carrier density and Co content were varied and T_C was evaluated by two independent measurements using a characteristic behavior in temperature dependence of resistivity, and temperature dependence of remanent magnetization. By extrapolating from low temperature measurements, T_C could be evaluated and T_C as functions of sample parameters could be obtained to discuss on its high T_C ferromagnetic mechanism.

6.2 Experimental details

Anatase $Ti_{1-x}Co_xO_{2-\delta}$ (001) epitaxial thin films were grown on $LaAlO_3$ (001) step substrates buffered with TiO_2 by pulsed laser deposition (PLD) with KrF excimer laser. The detail of film growth was described in the previous chapters. Two parameters of carrier density (n) and Co content (x) were controlled. In order to control the carrier density, oxygen pressure (P_{O_2}) during film growth was varied from 10^{-6} to 10^{-4} Torr. Co content were tuned by changing amount of Co in a ceramic target using for fabrication

process by PLD. The anatase $Ti_{1-x}Co_xO_{2-\delta}$ (001) epitaxial thin films were confirmed to be pure phase by x-ray diffraction. The typical film thickness was 45 nm. The transport properties were evaluated by four-probe and Hall effect measurements of Hall bar patterned samples. The carrier density was measured at 300 K. The magnetization was measured by SQUID magnetometer. The remanent magnetization (M_r) was measured from 2 to 380 K after field cooling in 0.5 T.

6.3 Results and discussions

6.3.1 Structural characterization

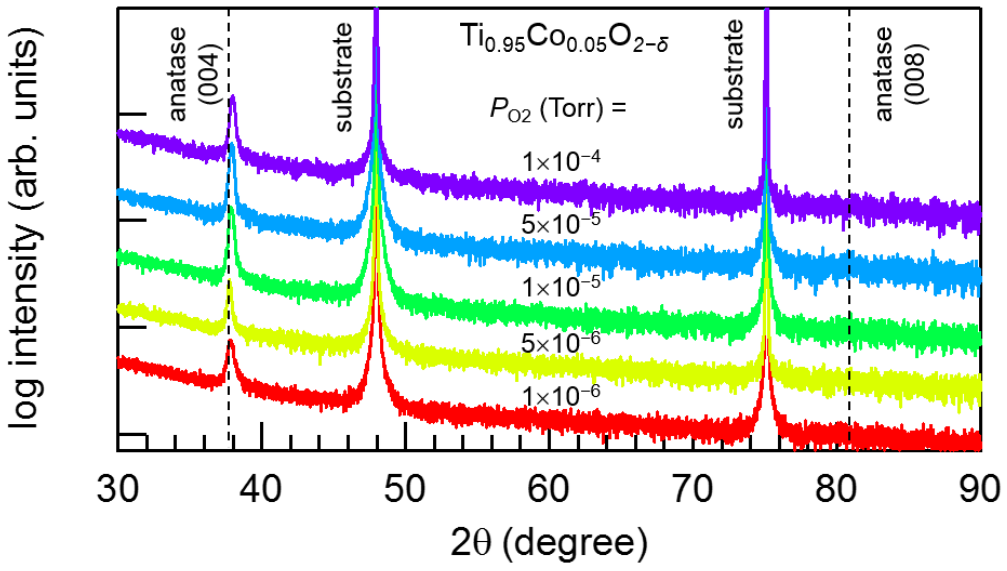

Figure 6.1 X-ray diffraction patterns of anatase $Ti_{0.95}Co_{0.05}O_{2-\delta}$ films fabricated under different oxygen partial pressure (P_{O_2}).

Figure 6.1 shows XRD diffraction patterns of anatase $Ti_{1-x}Co_xO_{2-\delta}$ films with x = 0.05 with various oxygen partial pressure (P_{O_2}) varied from 10^{-6} to 10^{-4} Torr. All films exhibit anatase (004) peak and small trace of anatase (008) peak. By decreasing P_{O_2}, the peak intensity of anatase (004) slightly decreased as well as sharpness of the peaks. This suggested that oxygen vacancies is introduced into the films and crystallinity get worse

due to the distorted anatase structure. The amount of oxygen vacancies is also related to the *c*-axis lattice constant of the films as shown in Figure 6.2. The *c*-lattice constant was increased as oxygen pressure decreased.

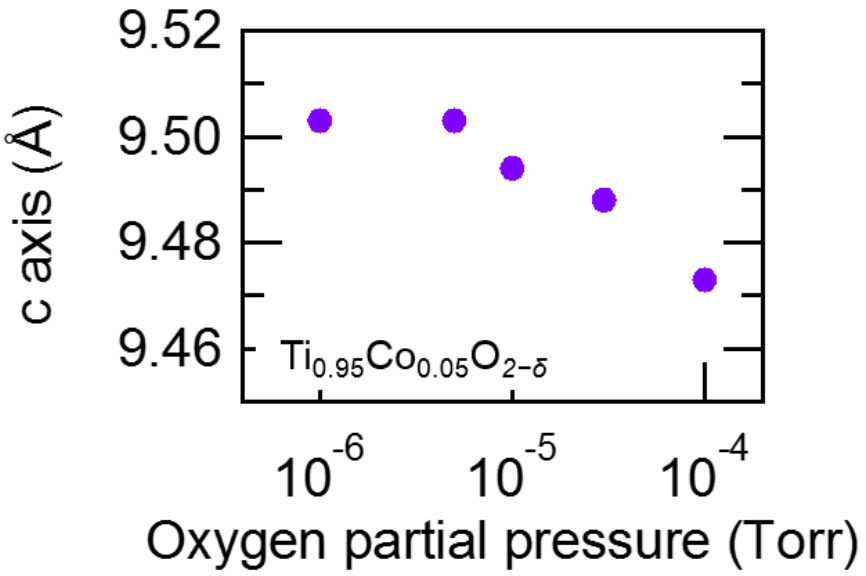

Figure 6.2 Relationship between *c*-lattice constant and oxygen partial pressure (P_{O_2}) of anatase $Ti_{0.95}Co_{0.05}O_{2-\delta}$ films.

For other series of Co contents (x = 0.01, 0.03, 0.07 and 0.10) varying with P_{O_2}, XRD patterns were also investigated and tendencies of both peak intensity and *c*-axis lattice constant were similarly observed. For moderately to highly doped films, x = 0.05, 0.07 and 0.10, the change of *c*-lattice constant is quite clear as well as the change of carrier density. On the other hand, for lightly doped films, x = 0.01 and 0.03, the change of *c*-lattice constant is not apparent probably relating to the opposite tendency of *c*-lattice constant in non-doped TiO_2 film [69].

6.3.2 Evaluation of T_C from transport and magnetization properties

In order to investigate ferromagnetic Curie temperature (T_C) in anatase $Ti_{1-x}Co_xO_{2-\delta}$ films, temperature dependence of transport and magnetization were evaluated. Here, the

details of evaluation of T_C will be described by using $Ti_{0.95}Co_{0.05}O_{2-\delta}$ films as representative data series. For other data series of Co contents (x = 0.01, 0.03, 0.07 and 0.10), the same data analysis and procedure were applied.

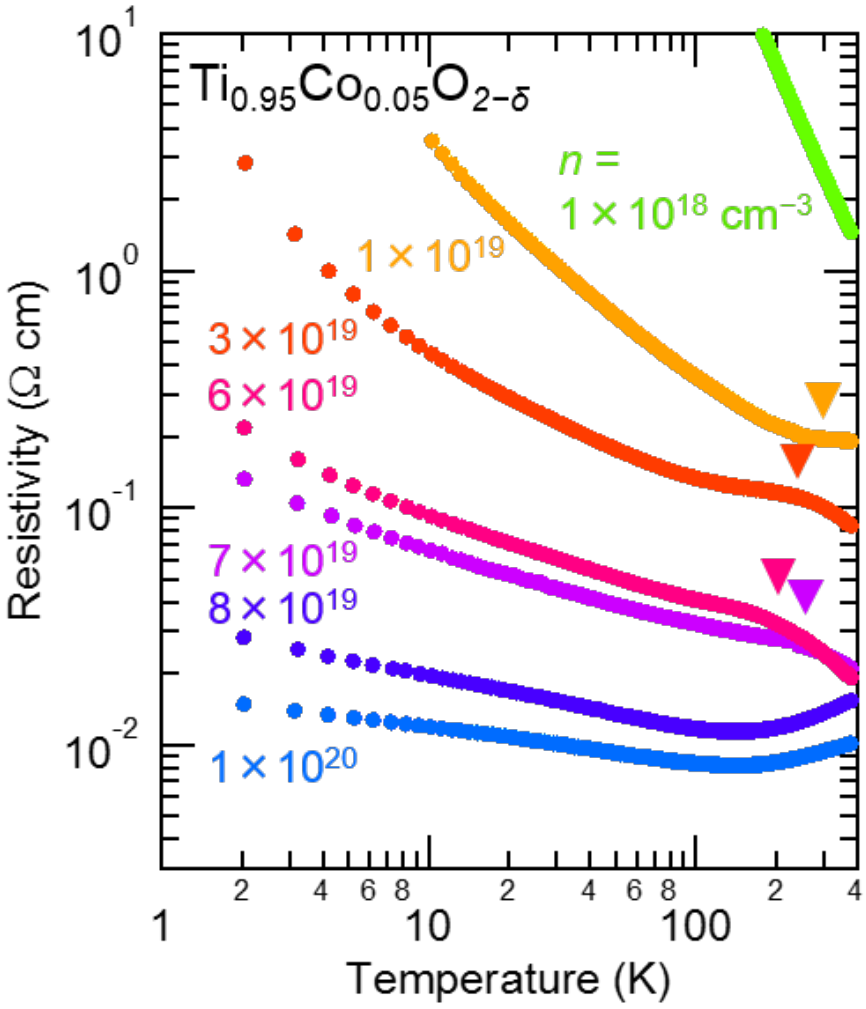

Figure 6.3 Temperature dependence of resistivity of anatase $Ti_{0.95}Co_{0.05}O_{2-\delta}$ films with different carrier density (n) labelled in the figure. Triangles mark position of kink structure for an eye guide.

Figure 6.3 shows temperature dependence of resistivity for anatase $Ti_{0.95}Co_{0.05}O_{2-\delta}$ films with different carrier density. The carrier density labeled as n in the figure was calculated from Hall measurement at 300 K. The temperature dependence of resistivity exhibited metallic to insulating behavior varied by decreasing carrier density. For highly

conducting films, a resistivity minimum was observed probably attributed to the Kondo effect, as discussed previously [81, 82].

Triangle marks labeled in Figure 6.3 represent the positions of kink structure. This behavior relates to carrier scattering induced by magnetic spin fluctuation near T_C and therefore, it is sometimes used to determine T_C . For anatase $Ti_{0.95}Co_{0.05}O_{2-\delta}$ films, only small kinks with large background were observed in contrast with distinguished kink observed in perovskite manganites [83–85]. This result possibly originates from the diluted nature and small magnetoresistance of (Ti,Co)O_2 compound. The observed kink structure was limited to moderately conducting samples with carrier density of $1 \times 10^{19} \leq n \leq 7 \times 10^{19}$ cm^{-3}. And the kink was not observed for paramagnetic insulating samples with carrier density $n = 1 \times 10^{18}$ cm^{-3} and for highly conducting samples with carrier density $n \geq 8 \times 10^{19}$ cm^{-3}. To conclude, temperature dependence of resistivity with kink structure was associated with the magnetism and reflected T_C for each sample.

Since the kink structure in (Ti,Co)O_2 compound is usually small even in log scale of temperature axis, the temperature derivative of resistivity (dρ/dT) is calculated in order to define the kink point more apparently. In addition, magnetoresistance (MR) defined as $\frac{\rho(9\mathrm{T}) - \rho(0)}{\rho(0)} \times 100$ (in %) were evaluated where $\rho(9\mathrm{T})$ and $\rho(0)$ are the resistivity under external magnetic field at 9 T and 0 T, respectively.

The temperature dependence of resistivity (ρ), temperature derivative of resistivity (dρ/dT) and magnetoresistance (MR) for anatase $Ti_{0.95}Co_{0.05}O_{2-\delta}$ film with intermediate carrier $n = 6 \times 10^{19}$ cm^{-3} are shown in Figure 6.4. A kink in the resistivity curve (Figure 6.4(a)) became more apparent by taking the temperature derivative indicating the local maximum and minimum (Figure 6.4(b)). The saddle point between the local maximum and minimum in the temperature derivative corresponded to the kink. The kink with dρ/d$T \neq 0$ (saddle point) indicates that the large background with a negative slope

is dominant. This differs from other compounds whose $d\rho/dT = 0$ (critical point) can represent the maximum resistivity or kink structure. Intriguingly, the temperature dependence of magnetoresistance (Figure 6.4(c)) showed similar behavior to that of $d\rho/dT$ and the largest negative magnetoresistance is approximately close to the local minimum of $d\rho/dT$ curve at which the location of T_C is expected. It is noted that the local minimum was not always observed in all samples because of the limitation of temperature range for the transport measurement and high resistivity background in insulating samples.

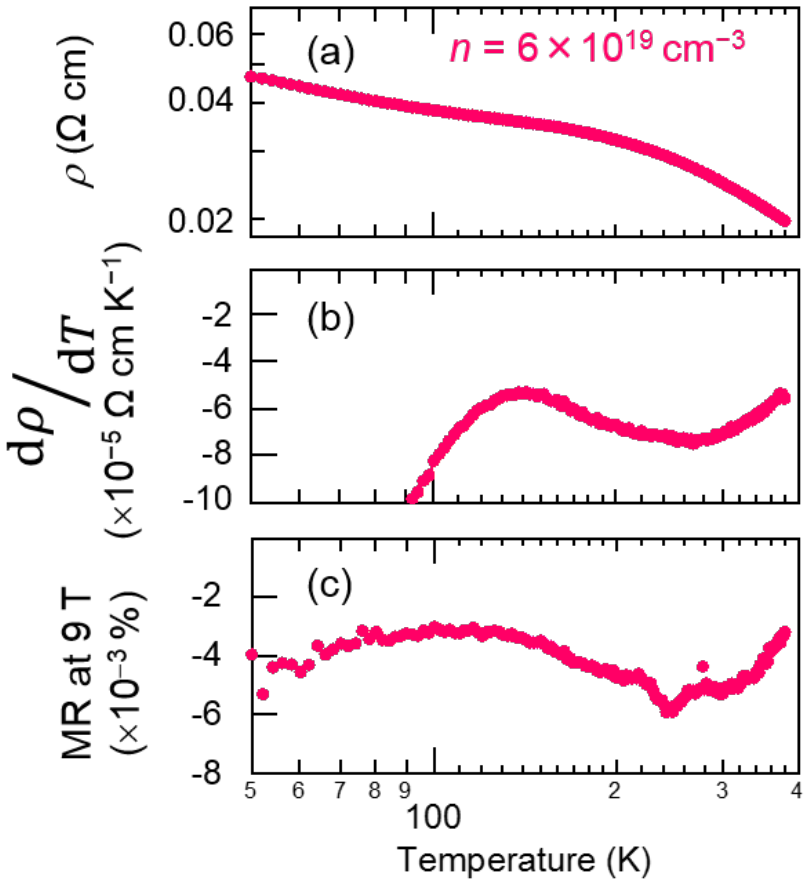

Figure 6.4 Temperature dependence of (a) resistivity (ρ), (b) temperature derivative of resistivity ($d\rho/dT$) and (c) magnetoresistance (MR) at 9 T for anatase $Ti_{0.95}Co_{0.05}O_{2-\delta}$ film with intermediate carrier $n = 6 \times 10^{19}$ cm^{-3}.

The suitable range of moderate carrier density was required to evaluate T_C by transport measurement via the local minimum of $d\rho/dT$ curve, on the other hand, the mag-

netization measurement was applicable to all films and may be used to evaluate the relationship of T_C vs. n. At the critical region below T_C the power-law of magnetization can be applied, $M_r \propto (1 - \frac{T}{T_C})^{\beta}$. The relation of $\mathrm{dln}M_r/\mathrm{d}T)^1 - T$ curve can be plotted, so called Kouvel-Fisher (KF) plot. From the KF plot, T_C can be obtained from the intercept of linear fitting on T-axis as also previously used in various compounds such as (Ga,Mn)As [86], $LaSrCoO_3$ [87], and (Pr,Sr)MnO_3 [88].

Temperature dependence of remanent magnetization ($M_r - T$) and its corresponding KF plots for $Ti_{0.95}Co_{0.05}O_{2-\delta}$ films with different carrier density are shown in Figure 6.5. The obtained $M_r - T$ curve shows concave behavior suggesting insulating-like system at which bound magnetic polarons could be present. For conducting sample with $n = 7 \times 10^{19}$ cm^{-3}, steep decrease in M_r was observed with increasing T (Figure 6.5(a)), whereas only slight decrease in M_r was observed for insulating sample with $n = 1 \times 10^{18}$ cm^{-3} (Figure 6.5(b)).

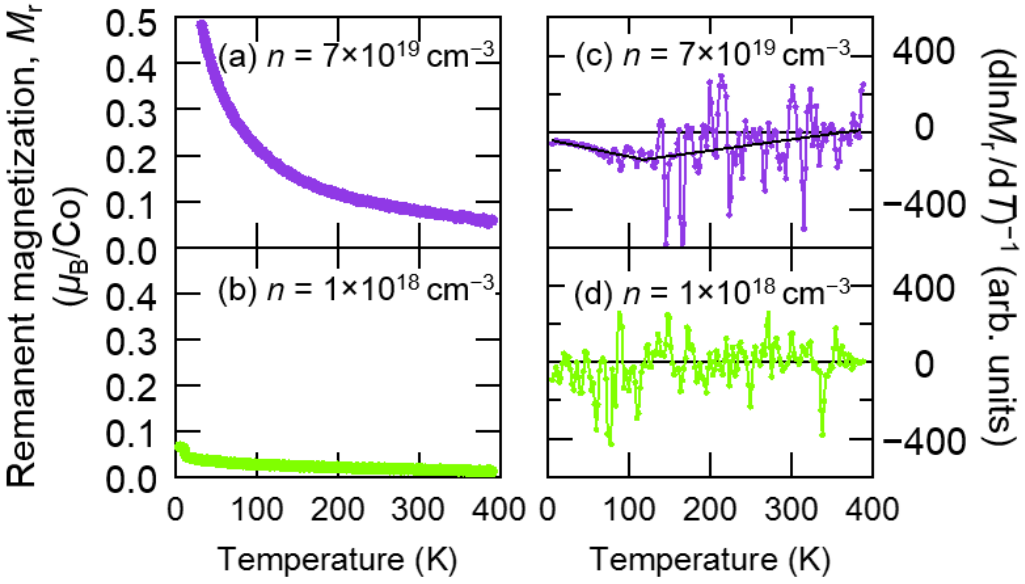

Figure 6.5 Temperature dependence of (a)–(b) remanent magnetization ($M_r - T$) and (c)–(d) its corresponding KF plots for $Ti_{0.95}Co_{0.05}O_{2-\delta}$ films with different carrier density $n = 7 \times 10^{19}$ cm^{-3} and 1×10^{18} cm^{-3}.

The corresponding KF plots of Figure 6.5(a) and (b) are shown in Figure 6.5(c) and (d), respectively. The KF plot of conducting sample (Figure 6.5(c)) exhibited a negative linear slope at much below T_C and a positive linear slope near T_C indicating inapplicable of the power law at much below T_C . The T_C was evaluated from $(\mathrm{dln}M_r/\mathrm{d}T)^{-1}$ $(T = T_C)$ = 0, i.e. T_C = 377 $\pm$ 134 K. On the contrary, insulating sample (Figure 6.5(d)) exhibited almost zero $(\mathrm{dln}M_r/\mathrm{d}T)^{-1}$, indicating T_C = 0, i.e. the sample was paramagnetic.

6.3.3 T_C as functions of carrier density and Co content

By using the local minimum of $\mathrm{d}\rho/\mathrm{d}T$ curves from electrical transport measurement and KF plots from magnetization measurement, T_C of anatase $Ti_{1-x}Co_xO_{2-\delta}$ films was systematically evaluated as functions of both carrier density (n) and Co content (x), for the first time. Figure 6.6 shows the summary of T_C as a function of n with different Co content, x = 0.01, 0.03, 0.05, 0.07 and 0.10.

For x = 0.03 and 0.05, the T_C values estimated from the local minimum of $\mathrm{d}\rho/\mathrm{d}T$ curves was obtained showing similar tendency to that obtained from KF plots despite the limited number of samples (Figure 6.6(b) and (c)). This result suggests that the local minimum of $\mathrm{d}\rho/\mathrm{d}T$ curves could be used to estimate T_C . For x = 0.01, the T_C increased with n for $n \lesssim 6 \times 10^{19}$ cm ^{3} (Figure 6.6(a)). It should be noted that for low Co content of x = 0.01, high carrier density is difficult to obtained due to the low film growth temperature. For moderate x, x = 0.03, 0.05, and 0.07, the T_C increased with n for $n \lesssim 6 \times 10^{19}$ cm ^{3} while decreased or saturated T_C was observed at the higher n (Figure 6.6(b)-(d)). For highly doped sample, x = 0.10, the T_C increased with n for $n \lesssim 1 \times 10^{20}$ cm ^{3} (Figure 6.6(e)). From these data, one may consider Co content dependence of T_C by focusing on the similar carrier density. It seems that the T_C was not a monotonically increasing function of x for the intermediate n, on the other hand, the T_C monotonically increased as x increased for the higher n samples.

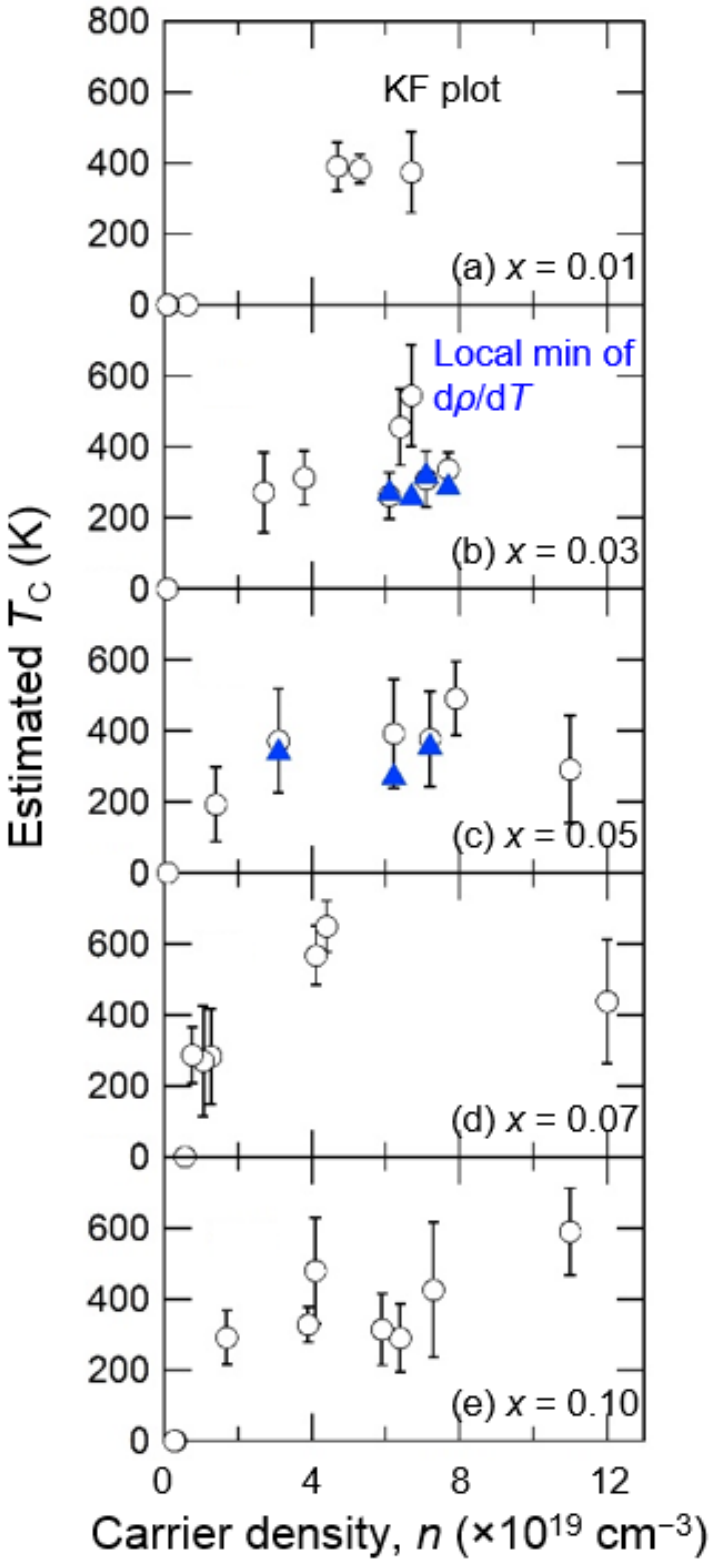

Figure 6.6 Estimated T_C as a function of carrier density for anatase $Ti_{0.95}Co_{0.05}O_{2-\delta}$ films with different x obtained from the local minimum of $d\rho/dT$ curves (solid triangle) and the KF plots (open circle). From (a) to (e), x = 0.01, 0.03, 0.05, 0.07 and 0.10.

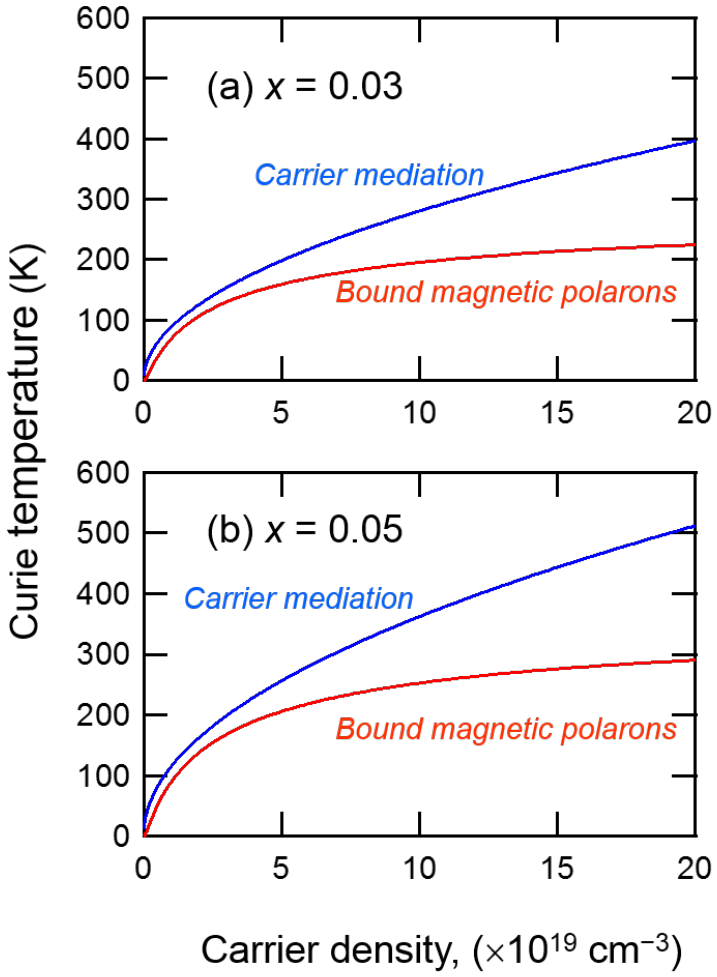

Figure 6.7 Theoretically estimated T_C of anatase $Ti_{1-x}Co_xO_{2-\delta}$ with (a) x = 0.03 and (b) x = 0.05. Blue and red line show the result from carrier mediation and bound percolation, respectively.

Theoretically calculated relation of T_C vs. n of anatase $Ti_{1-x}Co_xO_{2-\delta}$ with x = 0.03 and 0.05 by using the equations describing T_C for carrier mediation and bound magnetic percolation described in Chapter 1, are plotted in Figure 6.7 assuming $J = 1$ eV, $S = 1.5$, $s = 0.5$ and $a_B = 15$ Å. By either of these two mechanisms, the high T_C of (Ti,Co)O_2 cannot be explained. The non-monotonic relationship is clear for bound magnetic percolation while higher T_C could be expected for carrier mediation. From the result of T_C vs. n in this experiment, a non-monotonic relationship was observed suggesting the formation of bound magnetic polarons [89]. Therefore, in addition to

carrier mediated strong exchange interaction [16], the bound magnetic polaron also plays a principal role in the high T_C ferromagnetism, i.e. a combination of both mechanisms seems plausible.

The combination of two scenarios is similar to the idea previously proposed by Calderón et al. [52] that the cooperation between bound magnetic percolation at low temperature and Ruderman-Kittel-Kasuya-Yosida mechanism at high temperature could result in very high T_C up to ~700 K in ferromagnetic oxide semiconductors. For (Ti,Co)O_2, it is possible that some nucleation of polarons exists as substructure in a subatomic scale and is responsible for bound magnetic polaron, yielding in strong ferromagnetic exchange interaction associated with mobile carriers (Figure 6.8).

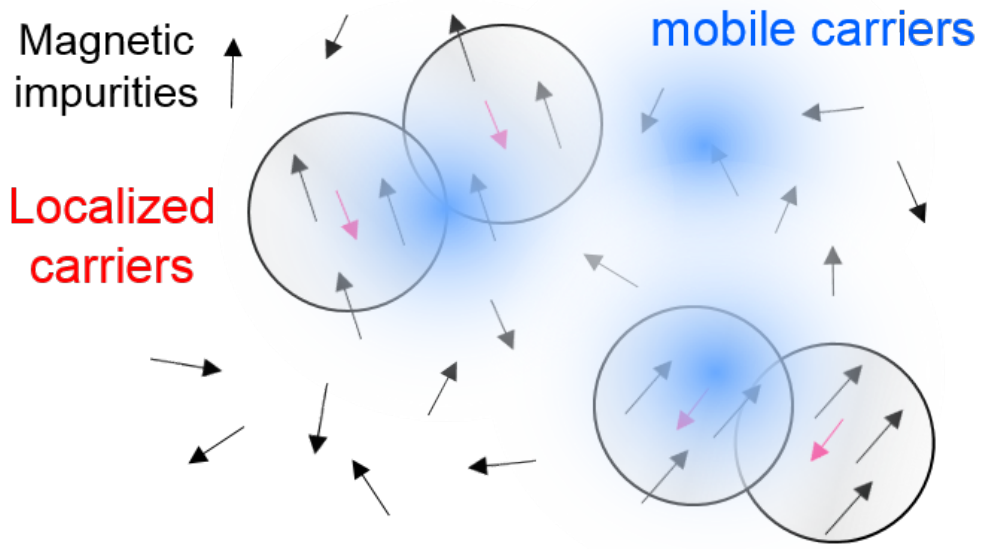

Figure 6.8 Illustration of bound magnetic polaron associated with mobile carriers which might responsible for strong ferromagnetic exchange interaction and high T_C .

6.3.4 Possible substructures in anatase (Ti,Co)O_2

Recently, substructure scenario has attracted much attention as it might be an explanation for high T_C. X-ray fluorescence holography (XFH) measurements, a method

for probing local structure, revealed formation of substructure around Co, although its detailed structure is unknown [*unpublished*]. Because magnetic polaron formed around this substructure could be the origin of the strong exchange interaction, I performed density functional theory (DFT) calculation with the Vienna *Ab initio* simulation package (VASP) in order to determine the entire structure of anatase (Ti,Co)O_2 containing the substructure. The structure optimization of $(2 \times 2 \times 1)$ unit cells was performed by using PBE function [90, 91] together with simulated annealing process.

The proposed substructures embedded in anatase structure are shown in Figure 6.9. Among them the structure P3 is the most stable structure considering from structural energy. The projections of the structure P3 comparing with original anatase TiO_2 are shown in Figure 6.10. This result suggests that there is no significant change in the total structure but only small distortion.

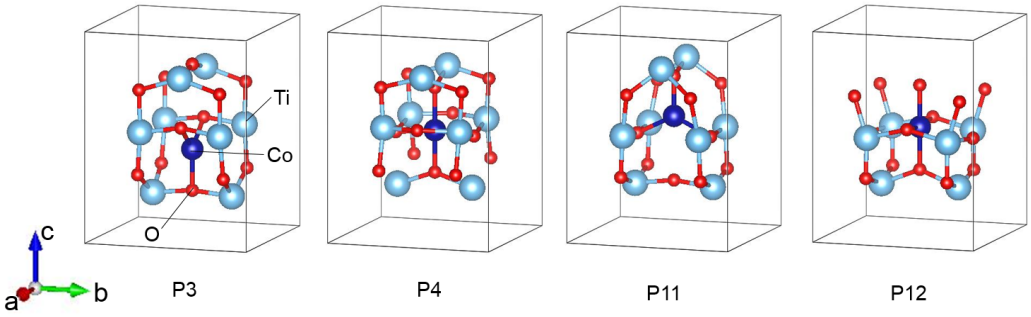

Figure 6.9 The proposed substructures embedded in anatase structure with $(2 \times 2 \times 1)$ unit cells.

The structures shown here were produced by VESTA software; K. Momma and F. Izumi, "VESTA 3 for three-dimensional visualization of crystal, volumetric and morphology data," *J. Appl. Crystallogr.*, **44**, 1272-1276 (2011).

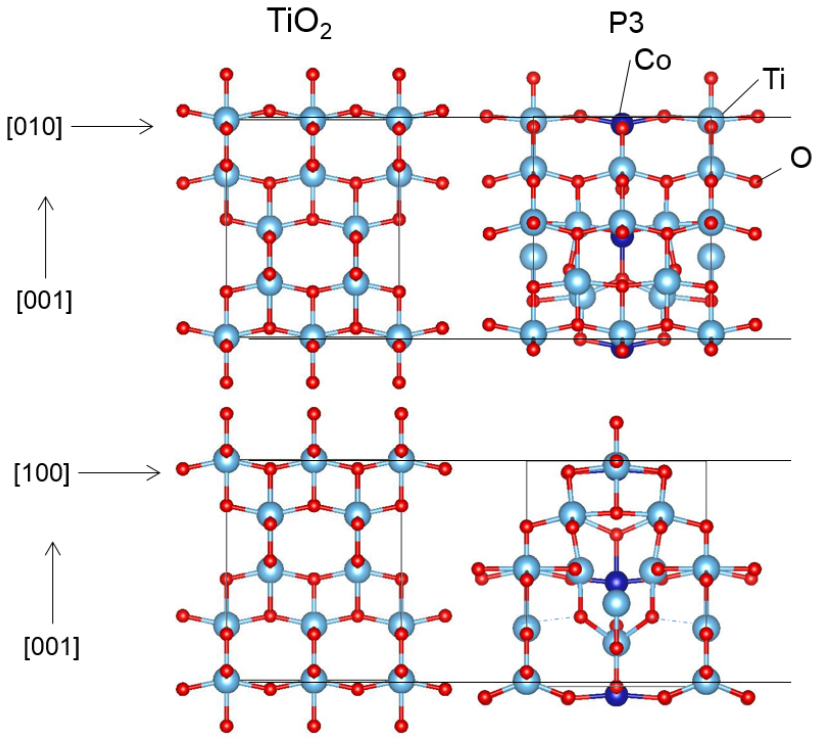

Figure 6.10 Comparison between original anatase strucuture of TiO_2 and the highest stable proposed substructures embedded in anatase structure.

The most stable substructure was further investigated to obtain its global minimum structure by using simulated annealing process. The structure P3 was annealed to 700 K and cooled down to 0 K, and then re-optimize process was performed. The obtained result suggests slight displacement of central part to gain more stable energy, $\Delta E \sim 0.4$ eV. The optimized P3 is presented in Figure 6.11 together with the suboxidic structure previously proposed for rutile $(Ti,Co)O_2$. The main different between the substructures in anatase and rutile $(Ti,Co)O_2$ is that the substructure in anatase is smaller and less complex due to less atomic density in anatase structure. The distance of Co–O and Co–Ti are 2.0 Å and 2.8 Å for the substructure embedded in anatase. Further detailed theoretical calculation

---

The structures shown here were produced by VESTA software; K. Momma and F. Izumi, "VESTA 3 for three-dimensional visualization of crystal, volumetric and morphology data," *J. Appl. Crystallogr.*, **44**, 1272-1276 (2011).

is still required to explain its contribution to the high T_C as well as its agreement to the experiments.

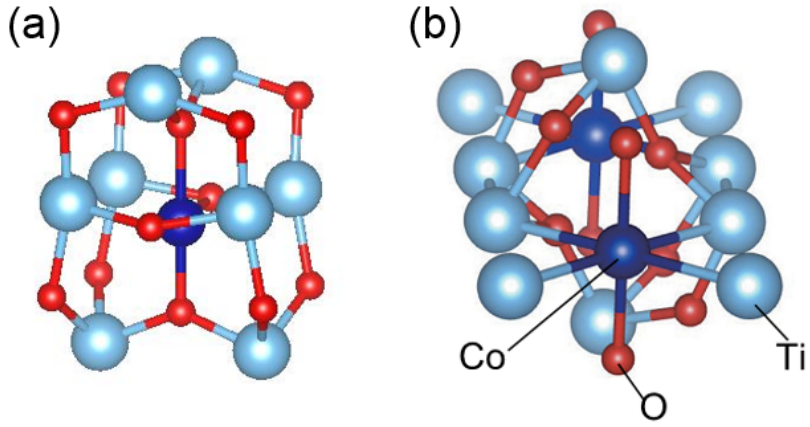

Figure 6.11 Comparison between proposed substructure (a) for anatase in this study and (b) for rutile in previous report [57]. Reprinted with permission from W. Hu, K. Hayashi, T. Fukumura, K. Akagi, M. Tsukada, N. Happo, S. Hosokawa, K. Ohwada, M. Takahasi, M. Suzuki, and M. Kawasaki, *Appl. Phys. Lett.* **106**, 222403 (2015). Copyright 2015, AIP Publishing LLC.

6.4 Conclusion

Ferromagnetic Curie temperature of anatase (Ti,Co)O_2 thin films was systematically investigated as functions of carrier density and Co content by using transport and magnetization measurements at low temperature regime below T_C. Temperature dependence of resistivity shows a characteristic behavior of kink structure which relates to magnetic property and T_C for each sample. The local minimum in its temperature derivatives, $d\rho/dT$, suggests T_C coinciding with the largest negative magnetoresistance. In addition, temperature dependence of remanent magnetization also provides a way to estimate T_C via KF plot. The relation of T_C vs. n in anatase $Ti_{1-x}Co_xO_{2-\delta}$ was revealed for the first time indicating non-monotonic function. This result implies the formation of bound magnetic polaron in addition to an importance of electron carriers reported previously. Therefore, it is possible that the formation of bound magnetic polaron incorporated with carrier-mediated exchange coupling might yield in strong exchange interaction and result

in high T_C in this system. I also investigated some possible substructures which might be responsible for nucleation of magnetic polaron in (Ti,Co)O_2 .

The mechanism of high T_C in ferromagnetic oxide semiconductor has been extensively debated whether carrier mediation or bound magnetic polarons shall be dominant. Different from an ordinary carrier mediation mechanism, it seems that bound magnetic polarons which might be formed around subatomic structures residing in the crystal framework, cooperates with mobile carriers. This might pose a way to design a high T_C ferromagnetic materials in which two mechanisms should be combined.

Chapter 7
General conclusions

In this dissertation, anatase $Ti_{1-x}Co_xO_{2-\delta}$ ((Ti,Co)O_2) epitaxial thin films were fabricated by pulsed laser deposition (PLD). The films were grown on anatase TiO_2 buffer layer and high quality anatase (Ti,Co)O_2 (001) epitaxial thin films were obtained. I mainly focused on three issues on this compound, i.e., microscopic ferromagnetism, magnetically dead layer and mechanism of the high T_C.

The observation of magnetic domain structure in anatase (Ti,Co)O_2 films were successfully performed by magnetic force microscopy at room temperature in vacuum condition. Systematic study of the domain as functions of carrier density and Co content was investigated and the average magnetic domain size showed increasing functions of both parameters. The systematic dependence of magnetic domain structure on carrier density agreed well with bulk magnetization suggesting a close relationship between microscopic and macroscopic ferromagnetism. The observation of magnetic domain structure in (Ti,Co)O_2 evidenced homogeneous ferromagnetism with high T_C in this compound. In addition, the understanding of magnetic domain structure could be one step towards magnetic domain manipulation in room temperature ferromagnetic semiconductor.

In this study, non-magnetic capping layer of TiO_2 was successfully developed to protect (Ti,Co)O_2 films from surface oxidation. Use of 2 nm-thick capping layer improved magnetization and enhanced perpendicular anisotropy with prolong magnetization stability at least for two years. The capping layer could prevent a formation of surface depletion region with deficient electron carriers. The capping technique was also effective for decreasing film thickness, which is useful for further device development using (Ti,Co)O_2 film.

Systematic investigation of T_C of anatase (Ti,Co)O_2 thin films was performed by using electrical transport and magnetization measurement at low temperature regime below T_C. The relation of T_C vs. n in anatase (Ti,Co)O_2 was revealed for the first time indicating non-monotonic function and implying the formation of bound magnetic polaron in addition to the carrier mediation reported previously. It is possible that bound magnetic polarons, probably related to subatomic structure residing in the crystal frameworks, cooperate with mobile carriers and result in high T_C in this system. The finding might pose a way to design high T_C ferromagnetic materials by considering the combination of two mechanisms.

In conclusion, magnetic domain structure in (Ti,Co)O_2 was revealed at room temperature and microscopic ferromagnetism was evidenced by homogeneous magnetic domains. In addition, non-magnetic capping layer developed in this study was effective to prevent a formation of magnetically dead layer. The relation of T_C vs. n in anatase (Ti,Co)O_2 suggested that magnetic bound polarons in concert with an ordinary carrier mediation are needed to consider. These results will contribute to further development of ferromagnetic domain manipulation devices utilizing (Ti,Co)O_2 and could also give a guide to explore new high T_C ferromagnetic semiconductors.

References

[1] T. Fukumura, M. Kawasaki, *Functional Metal Oxides: New Science and Novel Applications*, S. B. Ogale, T. V. Venkatesan, M. G. Blamire, eds. (John Wiley & Sons, Inc., Weinheim, 2013), chap. 3, pp. 91–131, first edn.

[2] T. Dietl, *Nature Materials* **9**, 965 (2010).

[3] T. Dietl, H. Ohno, F. Matsukura, J. Cibert, D. Ferrand, *Science* **287**, 1019 (2000).

[4] S. W. Jung, S.-J. An, G.-C. Yi, C. U. Jung, S.-I. Lee, S. Cho, *Applied Physics Letters* **80**, 4561 (2002).

[5] P. Sharma, A. Gupta, K. V. Rao, F. J. Owens, R. Sharma, R. Ahuja, J. M. O. Guillen, B. Johansson, G. A. Gehring, *Nature Materials* **2**, 673 (2003).

[6] Y. Q. Chang, D. B. Wang, X. H. Luo, X. Y. Xu, X. H. Chen, L. Li, C. P. Chen, R. M. Wang, J. Xu, D. P. Yu, *Applied Physics Letters* **83**, 4020 (2003).

[7] T. Fukumura, Y. Yamada, H. Toyosaki, T. Hasegawa, H. Koinuma, M. Kawasaki, *Applied Surface Science* **223**, 62 (2004).

[8] T. Fukumura, H. Toyosaki, Y. Yamada, *Semiconductor Science and Technology* **20**, S103 (2005).

[9] Y. Matsumoto, M. Murakami, T. Shono, T. Hasegawa, T. Fukumura, M. Kawasaki, P. Ahmet, T. Chikyow, S. Koshihara, H. Koinuma, *Science* **291**, 854 (2001).

[10] N. Hong, J. Sakai, W. Prellier, A. Hassini, A. Ruyter, F. Gervais, *Physical Review B* **70**, 195204 (2004).

[11] S. R. Shinde, S. B. Ogale, S. Das Sarma, J. R. Simpson, H. D. Drew, S. E. Lofland, C. Lanci, J. P. Buban, N. D. Browning, V. N. Kulkarni, J. Higgins, R. P. Sharma, R. L. Greene, T. Venkatesan, *Physical Review B* **67**, 115211 (2003).

[12] T. Fukumura, Y. Yamada, K. Tamura, K. Nakajima, T. Aoyama, A. Tsukazaki, M. Sumiya, S. Fuke, Y. Segawa, T. Chikyow, T. Hasegawa, H. Koinuma, M. Kawasaki, *Japanese Journal of Applied Physics* **42**, L105 (2003).

[13] Y. Yamada, T. Fukumura, K. Ueno, M. Kawasaki, *Applied Physics Letters* **99**, 242502 (2011).

[14] J. W. Quilty, A. Shibata, J.-Y. Son, K. Takubo, T. Mizokawa, H. Toyosaki, T. Fukumura, M. Kawasaki, *Physical Review Letters* **96**, 027202 (2006).

[15] D. H. Kim, J. S. Yang, K. W. Lee, S. D. Bu, T. W. Noh, S. J. Oh, Y. W. Kim, J. S. Chung, H. Tanaka, H. Y. Lee, T. Kawai, *Applied Physics Letters* **81**, 2421 (2002).

[16] Y. Yamada, K. Ueno, T. Fukumura, H. T. Yuan, H. Shimotani, Y. Iwasa, L. Gu, S. Tsukimoto, Y. Ikuhara, M. Kawasaki, *Science* **332**, 1065 (2011).

[17] J. M. D. Coey, *Magnetism and Magnetic Materials* (Cambridge, 2009).

[18] T. Shono, T. Hasegawa, T. Fukumura, F. Matsukura, H. Ohno, *Applied Physics Letters* **77**, 1363 (2000).

[19] T. Fukumura, T. Shono, K. Inaba, T. Hasegawa, H. Koinuma, F. Matsukura, H. Ohno, *Physica E: Low-dimensional Systems and Nanostructures* **10**, 135 (2001).

[20] S. S. P. Parkin, M. Hayashi, L. Thomas, *Science* **320**, 190 (2008).

[21] M. Yamanouchi, D. Chiba, F. Matsukura, H. Ohno, *Nature* **428**, 539 (2004).

[22] A. Yamaguchi, T. Ono, S. Nasu, K. Miyake, K. Mibu, T. Shinjo, *Physical Review Letters* **92**, 077205 (2004).

[23] I. M. Miron, G. Gaudin, S. Auffret, B. Rodmacq, A. Schuhl, S. Pizzini, J. Vogel, P. Gambardella, *Nature Materials* **9**, 230 (2010).

[24] U. Bauer, S. Emori, G. S. D. Beach, *Nature nanotechnology* **8**, 411 (2013).

[25] M. Tsoi, R. E. Fontana, S. S. P. Parkin, *Applied Physics Letters* **83**, 2617 (2003).

[26] M. Yamanouchi, D. Chiba, F. Matsukura, T. Dietl, H. Ohno, *Physical Review Letters* **96**, 096601 (2006).

[27] M. Yamanouchi, J. Ieda, F. Matsukura, S. E. Barnes, S. Maekawa, H. Ohno, *Science* **317**, 1726 (2007).

[28] Y. Matsumoto, R. Takahashi, M. Murakami, T. Koida, X.-J. Fan, T. Hasegawa, T. Fukumura, M. Kawasaki, S.-Y. Koshihara, H. Koinuma, *Japanese Journal of Applied Physics, Part 2: Letters* **40**, L1204 (2001).

[29] N. Bahadur, R. Pasricha, Govind, S. Chand, R. K. Kotnala, *Materials Chemistry and Physics* **133**, 471 (2012).

[30] H. J. Meng, D. L. Hou, L. Y. Jia, X. J. Ye, H. J. Zhou, X. L. Li, *Journal of Applied Physics* **102**, 073905 (2007).

[31] N. H. Hong, A. Ruyter, F. Gervais, W. Prellier, J. Sakai, *Journal of Applied Physics* **97**, 10D323 (2005).

[32] N. H. Hong, J. Sakai, W. Prellier, A. Ruyter, *Journal of Physics D: Applied Physics* **38**, 816 (2005).

[33] H. S. Yang, R. K. Singh, *Journal of Applied Physics* **95**, 7192 (2004).

[34] C.-R. Cho, J.-P. Kim, J.-Y. Hwang, S.-Y. Jeong, Y.-G. Joh, D.-H. Kim, *Japanese Journal of Applied Physics* **43**, L1323 (2004).

[35] N. H. Hong, W. Prellier, J. Sakai, A. Ruyter, *Journal of Physics: Condensed Matter* **16**, 5549 (2004).

[36] M. Kowalewski, W. H. Butler, N. Moghadam, G. M. Stocks, T. C. Schulthess, K. J. Song, J. R. Thompson, A. S. Arrott, T. Zhu, J. Drewes, R. R. Katti, M. T. McClure, O. Escorcia, *Journal of Applied Physics* **87**, 5732 (2000).

[37] K. Oguz, P. Jivrajka, M. Venkatesan, G. Feng, J. M. D. Coey, *Journal of Applied Physics* **103**, 07B526 (2008).

[38] R. P. Borges, W. Guichard, J. G. Lunney, J. M. D. Coey, F. Ott, *Journal of Applied Physics* **89**, 3868 (2001).

[39] H. Yamada, Y. Ogawa, Y. Ishii, H. Sato, M. Kawasaki, H. Akoh, Y. Tokura, *Science* **305**, 646 (2004).

[40] M. Schultz, S. Levy, J. W. Reiner, L. Klein, *Physical Review B* **79**, 125444 (2009).

[41] V. R. Singh, Y. Sakamoto, T. Kataoka, M. Kobayashi, Y. Yamazaki, A. Fujimori, F.-H. Chang, D.-J. Huang, H.-J. Lin, C. T. Chen, H. Toyosaki, T. Fukumura, M. Kawasaki, *Journal of Physics: Condensed Matter* **23**, 176001 (2011).

[42] V. R. Singh, K. Ishigami, V. K. Verma, G. Shibata, Y. Yamazaki, T. Kataoka, A. Fujimori, F.-H. Chang, D.-J. Huang, H.-J. Lin, C. T. Chen, Y. Yamada, T. Fukumura, M. Kawasaki, *Applied Physics Letters* **100**, 242404 (2012).

[43] N. Yamashita, T. Sudayama, T. Mizokawa, Y. Yamada, T. Fukumura, M. Kawasaki, *Applied Physics Letters* **96**, 021907 (2010).

[44] C.-Y. Hung, M. Mao, S. Funada, T. Schneider, L. Miloslavsky, M. Miller, C. Qian, H. C. Tong, *Journal of Applied Physics* **87**, 6618 (2000).

[45] L. Abad, B. Martínez, L. Balcells, *Applied Physics Letters* **87**, 212502 (2005).

[46] Y.-H. Wang, W.-C. Chen, S.-Y. Yang, K.-H. Shen, C. Park, M.-J. Kao, M.-J. Tsai, *Journal of Applied Physics* **99**, 08M307 (2006).

[47] J. Li, Z. Y. Wang, A. Tan, P.-A. Glans, E. Arenholz, C. Hwang, J. Shi, Z. Q. Qiu, *Physical Review B* **86**, 054430 (2012).

[48] A. Kaminski, S. Das Sarma, *Physical Review Letters* **88**, 247202 (2002).

[49] J. M. D. Coey, M. Venkatesan, C. B. Fitzgerald, *Nature Materials* **4**, 173 (2005).

[50] T. Fukumura, Y. Yamada, K. Ueno, H. Yuan, H. Shimotani, Y. Iwasa, L. Gu, S. Tsukimoto, Y. Ikuhara, M. Kawasaki, *SPIN* **02**, 1230005 (2012).

[51] T. Zhao, S. R. Shinde, S. B. Ogale, H. Zheng, T. Venkatesan, R. Ramesh, S. Das Sarma, *Physical Review Letters* **94**, 126601 (2005).

[52] M. J. Calderón, S. Das Sarma, *Annals of Physics* **322**, 2618 (2007).

[53] B. S. Sørensen, P. E. Lindelof, J. Sadowski, R. Mathieu, P. Svedlindh, *Applied Physics Letters* **82**, 2287 (2003).

[54] K. Sato, H. Katayama-Yoshida, P. H. Dederichs, *Japanese Journal of Applied Physics, Part 2: Letters* **44** (2005).

[55] T. Dietl, K. Sato, T. Fukushima, A. Bonanni, M. Jamet, A. Barski, S. Kuroda, M. Tanaka, Spinodal nanodecomposition in magnetically doped semiconductors. ArXiv:1412.8062v2.

[56] K. Griffin Roberts, M. Varela, S. Rashkeev, S. T. Pantelides, S. J. Pennycook, K. M. Krishnan, *Physical Review B* **78**, 014409 (2008).

[57] W. Hu, K. Hayashi, T. Fukumura, K. Akagi, M. Tsukada, N. Happo, S. Hosokawa, K. Ohwada, M. Takahasi, M. Suzuki, M. Kawasaki, *Applied Physics Letters* **106**, 222403 (2015).

[58] L. W. Martin, Y. H. Chu, R. Ramesh, *Materials Science and Engineering R* **68**, 89 (2010).

[59] S. Ohashi, M. Lippmaa, N. Nakagawa, H. Nagasawa, H. Koinuma, M. Kawasaki, *Review of Scientific Instruments* **70**, 178 (1999).

[60] M. N. R. Ashfold, F. Claeyssens, G. M. Fuge, S. J. Henley, *Chemical Society Reviews* **33**, 23 (2004).

[61] C. Kittel, *Introduction to Solid State Physics* (John Wiley & Sons, Inc., 2005).

[62] B. D. Cullity, C. D. Graham, *Introduction to Magnetic Materials* (John Wiley & Sons, Inc., 2009).

[63] A. Hubert, R. Schafer, *Magnetic Domains* (Springer, Heidelberg, 1998).

[64] U. Hartmann, *Annual Review of Materials Science* **29**, 53 (1999).

[65] T. Yamaoka, K. Watanabe, Y. Shirakawabe, K. Chinone, *Journal of the Magnetics Society of Japan* **27**, 429 (2003).

[66] F. Jensen, *Introduction to Computational Chemistry* (John Wiley & Sons, Inc., 2007).

[67] L. Däweritz, *Reports on Progress in Physics* **69**, 2581 (2006).

[68] S. W. Shin, G. L. Agawane, I. Y. Kim, Y. B. Kwon, I. O. Jung, M. G. Gang, A. Moholkar, J.-H. Moon, J. H. Kim, J. Y. Lee, *Applied Surface Science* **258**, 5073 (2012).

[69] T. S. Krasienapibal, T. Fukumura, Y. Hirose, T. Hasegawa, *Japanese Journal of Applied Physics* **53**, 090305 (2014).

[70] P. N. Hai, L. D. Anh, S. Mohan, T. Tamegai, M. Kodzuka, T. Ohkubo, K. Hono, M. Tanaka, *Applied Physics Letters* **101**, 182403 (2012).

[71] U. S. Ram, P. Gaunt, *Journal of Applied Physics* **54**, 2872 (1983).

[72] S. Okamoto, N. Kikuchi, O. Kitakami, T. Miyazaki, Y. Shimada, K. Fukamichi, *Physical Review B* **66**, 024413 (2002).

[73] J. U. Thiele, L. Folks, M. F. Toney, D. K. Weller, *Journal of Applied Physics* **84**, 5686 (1998).

[74] J. König, T. Jungwirth, A. H. MacDonald, *Physical Review B* **64**, 184423 (2001).

[75] C. Gourdon, A. Dourlat, V. Jeudy, K. Khazen, H. J. von Bardeleben, L. Thevenard, A. Lemaître, *Physical Review B* **76**, 241301 (2007).

[76] A. Dourlat, C. Gourdon, V. Jeudy, K. Khazen, H. J. von Bardeleben, L. Thevenard, A. Lemaître, *Physica E: Low-dimensional Systems and Nanostructures* **40**, 1848 (2008).

[77] T. Ohtsuki, A. Chainani, R. Eguchi, M. Matsunami, Y. Takata, M. Taguchi, Y. Nishino, K. Tamasaku, M. Yabashi, T. Ishikawa, M. Oura, Y. Senba, H. Ohashi, S. Shin, *Physical Review Letters* **106**, 047602 (2011).

[78] K. S. Takahashi, H. Y. Hwang, *Applied Physics Letters* **93**, 082112 (2008).

[79] C. W. Cheng, W. Feng, G. Chern, C. M. Lee, T. H. Wu, *Journal of Applied Physics* **110**, 033916 (2011).

[80] M. Yamanouchi, R. Koizumi, S. Ikeda, H. Sato, K. Mizunuma, K. Miura, H. D. Gan, F. Matsukura, H. Ohno, *Journal of Applied Physics* **109**, 07C712 (2011).

[81] T. P. Sarkar, K. Gopinadhan, M. Motapothula, S. Saha, Z. Huang, S. Dhar, A. Patra, W. M. Lu, F. Telesio, I. Pallecchi, Ariando, D. Marré, T. Venkatesan, *Scientific Reports* **5**, 13011 (2015).

[82] R. Ramaneti, J. C. Lodder, R. Jansen, *Physical Review B* **76**, 195207 (2007).

[83] A. Urushibara, Y. Moritomo, T. Arima, A. Asamitsu, G. Kido, Y. Tokura, *Physical Review B* **51**, 103 (1995).

[84] M. Jaime, H. T. Hardner, M. B. Salamon, M. Rubinstein, P. Dorsey, D. Emin, *Physical Review Letters* **78**, 951 (1997).

[85] G. C. Xiong, Q. Li, H. L. Ju, S. N. Mao, L. Senapati, X. X. Xi, R. L. Greene, T. Venkatesan, *Applied Physics Letters* **66**, 1427 (1995).

[86] M. Wang, R. A. Marshall, K. W. Edmonds, A. W. Rushforth, R. P. Campion, B. L. Gallagher, *Applied Physics Letters* **104**, 132406 (2014).

[87] S. Mukherjee, P. Raychaudhuri, A. K. Nigam, *Physical Review B* **61**, 8651 (2000).

[88] A. K. Pramanik, A. Banerjee, *Physical Review B* **79**, 214426 (2009).

[89] S. Das Sarma, E. H. Hwang, A. Kaminski, *Physical Review B* **67**, 155201 (2003).

[90] J. P. Perdew, K. Burke, M. Ernzerhof, *Phys. Rev. Lett.* **77**, 3865 (1996).

[91] J. P. Perdew, K. Burke, M. Ernzerhof, *Phys. Rev. Lett.* **78**, 1396 (1997).